THÈSE

En vue de l'obtention du

DOCTORAT DE L'UNIVERSITÉ DE TOULOUSE

Délivré par :

Institut National Polytechnique de Toulouse (Toulouse INP)

Discipline ou spécialité :

Dynamique des fluides

Présentée et soutenue par :

M. HONG DUC LE

le lundi 4 juin 2018

Titre :

Modélisation d'un jet chargé en nanoparticules à partir d'une fuite de canalisation de transport

---

Ecole doctorale :

Mécanique, Energétique, Génie civil, Procédés (MEGeP)

Unité de recherche :

Institut de Mécanique des Fluides de Toulouse (I.M.F.T.)

Directeur(s) de Thèse :

M. ERIC CLIMENT

M. PASCAL FEDE

Rapporteurs :

Mme ANNE TANIERE, UNIVERSITÉ LORRAINE

M. SIMON GANT, HEALTH AND SAFETY LABORATORY

Membre(s) du jury :

M. OLIVIER DUFAUD, UNIVERSITÉ LORRAINE, Président

M. BENJAMIN TRUCHOT, INERIS, Membre

M. CRISTIAN MARCHIOLI, UNIVERSITE D'UDINE, Membre

M. ERIC CLIMENT, INP TOULOUSE, Membre

M. MARTIN SOMMERFELD, UNIVERSITE OTTO VON GUERICKE MAGDEBURG, Membre

M. PASCAL FEDE, UNIVERSITE TOULOUSE 3, Membre

"As far as the laws of mathematics refer to reality, they are not certain, and as far as they are certain, they do not refer to reality."

Albert Einstein

Acknowledgement

I would like first to acknowledge INERIS and IMFT for financing and according me to realize my thesis.

I would like to thank Olivier DUFAUD, President of the jury, Anne TANIERE and Simon GANT, reviewers, Christian MARCHIOLI, examiner, and all jury members for their presences at my thesis defence and their interesting discussions to improve my work. *May the Brownian Force be with you!*

My thesis couldn't be archived without Eric CLIMENT, my director, and Pascal FEDE, my co-director. I thank them for their engagements, their understanding and their encouragements during my thesis. They enhanced my capability, my knowledge and my motivation in my research field. Many thanks to Benjamin TRUCHOT, my INERIS supervisor, and also Bruno DEBRAY, Jean-Marc LACOME and Alexis VIGNES for interesting discussions on the thesis context, physics and other subjects. Thanks to them, I could participate to different international and national conferences and had interesting discussions with researchers in my research field.

I would like to thank prof. Martin SOMMERFELD for his presence at my thesis defence and for interesting discussions during my exchange in his laboratory. A great thanks to Martin ERNST for helping me in the use of the complex Lattice Boltmann code. I also thank members of Institut für Verfahrenstechnik for very funny youtube videos at lunch time.

Many thanks to COSINUS Service, especially Hervé NEAU, for helping me with the use of Neptune_CFD and also some simulation cases of Code_Saturne. I would like to thank Florence COLOMBIES, secretariat of PSC group, for facilitating my stay at IMFT and for her engagements in my administration documents at the beginning of my thesis.

I sincerely thank all PhD students, post-doctoral and members of PSC group for creating a very welcome environment, funny and also serious discussions on research topics. Special thanks to Lokman BENNANI, my 'officemate', for helping me in the use of SALOME, for the stories from his thesis and interesting discussions about physics, especially at the party after 10 pm.

With more than 2 years at INERIS, I had many great memories thanks to members of PHDS division. I would like to thank them for their encouragements, interesting discussions and helpful advices from their thesis. Also, I thank them for stressing me out in the morning of my thesis defence because for them, I was very calm (only on the outside). Special thanks to Lauris JOUBERT for reviewing my publications and taking time to answers my mathematical questions. Many thanks to Guilaumme LEROY, Frédéric TOGNET for helping me in the use of ADMS. I would like also to thank Stephane and Christian for their engagements to help me in the experiment at INERIS. Many thanks to Veronique LEJEUNE, secretariat of PHDS division, for facilitating my stay at INERIS. Also special thanks to Guillaume LECOCQ for so many free rides to Compiègne.

Ma thèse s'est bien passé grâce aux encouragements de mes amis. Je tiens à re-

mercier la famille BIENVENU d'avoir eu confiance en mes succès. Je voudrais remercier également la famille CHEVALLIER (+ Arlequine, E.T., la Mouffette) pour leurs encouragements, les vendredis crêpes, les repas délicieux du dimanche et les randonnées très naturelles dans la vallée de Chevreuse.

Con cảm ơn Bá, Má đã cho con điều kiện để đi du học và ủng hộ con khi con lựa chọn học tiến sĩ. Chúc mừng đám cưới của Giang và Mai. Chuẩn bị lên kế hoạch đi du lịch Châu Âu thôi!

Pour finir, je remercie Joël pour les voyages inoubliables, les beaux concerts et pour être toujours là pour moi.

Résumé

Depuis quelques années, les nanomatériaux sont de plus en plus utilisés dans les processus industriels. Afin de protéger la population et l'environnement des possibles conséquences lors de rejets accidentels de ces produits dans l'atmosphère, des analyses de risques ont permis d'identifier des scénarios accidentels dans le cas du transport, de la manipulation et du stockage. Parmi les cas de fuite non intentionnelle dans l'atmosphère libre, la fuite accidentelle sur un convoyeur peut générer un relargage massif de nanoparticules. Afin d'évaluer les conséquences de ce type de scénario accidentel, notre étude s'intéresse à la prédiction des propriétés du nuage de particules dispersées dans l'air, par exemple la concentration en nombre et la distribution des diamètres. La première étape de l'étude consiste à synthétiser les phénomènes physiques des nanoparticules dans l'air afin de choisir les phénomènes physiques les plus pertinants à modéliser. Les phénomènes physiques à modéliser sont la forme complexe des agglomérats, la force de traînée des agglomérats, la fragmentation des agglomérats par le fluide, la collision et l'agglomération des agglomérats. Ensuite, la modélisation des phénomènes physiques est développée dans l'outil CFD Code_Saturne. Pour chaque phénomène physique, un cas de simulation numérique est réalisé pour vérifier le développement de la modélisation dans l'outil CFD. Une bonne comparaison des résultats CFD avec les résultats de modèle 0D de Scilab et les modèles dans la litérature est obtenue. Egalement dans notre étude, un nouveau modèle de la probabilité de collision des agglomérats est proposé. Ces nouveaux modèles sont validés par les expérimentations numériques. Ensuite, l'outil CFD développé est appliqué dans une simulation d'une fuite de canalisation de transport. La zone proche de la fuite est simulée par Code_Saturne. Les résultats du Code_Saturne sont utilisés comme les données entrées pour ADMS, un outil numérique de la dispersion des particules à grande échelle. Les résultats montrent que les particules sont dispersées plus de 1 km par rapport au terme source, ce qui est en accord avec la distance observée. En perspective, l'influence de plusieurs paramètres comme la vitesse du vent, les propriétés des particules comme la distribution de taille ou la concentration en agglomérats pourrait être testé. Une expérimentation de rejet des microparticules est réalisée à l'INERIS pour ensuite pouvoir étudier les rejets des nanoparticules à l'échelle laboratoire.

Mots clés: nanoparticules, agglomération, fragmentation, dispersion.

Abstract

Since a few years, nanomaterials are more and more used in industrial process. In order to protect the population and the environment from the consequences of an accidental release into the atmosphere, the risk assessment allowed to identify the accidental scenario in transport, manipulation and storage of those products. The accidental leakage of the conveying pipe may lead to a massive release of nanoparticles. In order to evaluate the consequences of this type of accident, our study focuses on the prediction of particles properties dispersed into the air, for example the particle number concentration and the particle diameter distribution. The first step of the study consists in the analyse of physical phenomena related to nanoparticles in order to choose the most predominant physical phenomena to model. The relevant physical phenomena in the present configuration are the agglomerate complex shape, the drag force on agglomerates, the agglomerate breakage by gas, the agglomerate collision and the agglomeration. After that, the modelling of physical phenomena chosen is developed in CFD tool Code_Saturne. For each physical phenomenon, a simulation test case is realized in order to verify the development in CFD tool. A good agreement between CFD tool Code_Saturne and 0D tool from Scilab and model in the literature is obtained. Also in the present study, new model for the collision probability of agglomerates is proposed. This new model is validated with the numerical experiment. After that, the numerical tool developed is applied in a simulation of an accidental pipe leakage. The field near the leakage is simulated by Code_Saturne. The results from Code_Saturne is used as the input data for ADMS tool, a simulation tool for the particle dispersion in large scale. The results show that the particles are dispersed more than 1 km from the release source, which is in agreement with the distance observed. In perspective, the influences of different parameters as the wind field and the particle properties, on the agglomerate size and number distribution can be tested. An experiment of the microparticle jet is realized at INERIS in order to be able to assess the nanoparticle jet experiment in the laboratory scale

Keywords: nanoparticles, agglomeration, breakage, dispersion.

Contents

List of Figures

List of Tables

List of symbol

Latin symbols

A	Hamaker constant	[J]
A_A	agglomerate collision cross section	[m^2]
A_{c-s}	agglomerate cross section	[m^2]
A_s	spherical particle collision cross section	[m^2]
C_c	Cunningham correction coefficient	[-]
C_d	drag coefficient for spherical particles	[-]
$C_{d,A}$	agglomerate drag coefficient	[-]
C_μ	constant in $k-\varepsilon$ model	[-]
$C_{\varepsilon 1}$	constant in $k-\varepsilon$ model	[-]
$C_{\varepsilon 2}$	constant in $k-\varepsilon$ model	[-]
D_{Br}	Brownian diffusion coefficient	[$m^2.s^{-1}$]
D_f	fractal dimension	[-]
D_{nozzle}	nozzle diameter	[-]
D_{SE}	Stokes - Einstein diffusion coefficient	[$m^2.s^{-1}$]
D_T	turbulent diffusion coefficient	[$m^2.s^{-1}$]
d_{12}	effective diameter of two agglomerates	[m]
d_{50}	agglomerate median count diameter	[m]
d_A	agglomerate characteristic diameter	[m]
$\overline{d_A}$	mean agglomerate characteristic diameter	[m]
d_{A1}	characteristic diameter of the first agglomerate	[m]
d_{A2}	characteristic diameter of the second agglomerate	[m]
d_p	particle diameter	[m]
d'_{p1}	diameter of the equivalent spherical particle	[m]
d_{p1}	diameter of the first spherical particle	[m]
d_{p2}	diameter of the second spherical particle	[m]
d_{fict}	diameter of the fictitious particle	[m]
d_{pp}	primary particle diameter	[m]
E_{12}	effective Young modulus of two agglomerates	[$N.m^{-2}$]
E_A	agglomerate Young modulus	[$N.m^{-2}$]
e_c	rebound coefficient	[-]
F_{capil}	capillary force	[N]
F_{vdw}	van der Waals force	[N]
f_{coll}	collision frequency	[s^{-1}]
g_i	gravity component in direction i	[$m.s^{-2}$]
I	turbulent intensity	[%]
K_f	structure coefficient	[-]
K_n	Knudsen number	[-]
k_B	Boltzmann constant	[$J.K^{-1}$]

k_c	mean coordination number in agglomerate	[-]
k_f	fluid kinetic energy	[J]
l_{cube}	length of a cube	[-]
l_T	turbulent mix length	[m]
m_{12}	effective mass of two agglomerates	[kg]
m_A	agglomerate mass	[kg]
m_{pp}	primary particle mass	[kg]
N_A	total agglomerates number	[-]
$N_{A,fr}$	number of agglomerates having a breakge	[-]
N_{pp}	primary particle number	[-]
N_{pp}^{+}	new agglomerate primary particle number after agglomeration	[-]
N_{pp}^{-}	agglomerate primary particle number before agglomeration	[-]
$N_{pp,fict}$	primary particle number of fictitious agglomerate	[-]
N_t	total time steps	[-]
$\overline{N_{pp}}$	mean primary particle number	[-]
n_p	particle number density	[m^{-3}]
n_A	agglomerate number density	[m^{-3}]
P_A	agglomerates collision probability	[-]
P_{coll}	collision probability	[-]
$P_{coll,s}$	collision probability for spherical particles	[-]
P	pressure	[$N.m^{-2}$]
P_k	turbulence production by fluid velocity	[-]
q_{fp}	fluid - particle velocity covariance	[$m^2.s^{-2}$]
$q_{f@p}^2$	fluid kinetic energy 'seen' by particles	[$m^2.s^{-2}$]
q_p^2	particle kinetic energy	[$m^2.s^{-2}$]
$\bar{p}$	maximum deformation pressure	[$N.m^{-2}$]
$R.H.$	relative humidity	[%]
R_A	collision probability coefficient for agglomerates	[-]
R_0	agglomerate interception radius	[m]
$R_{Frag,A}$	ratio between the fluid stress and the agglomerate strength	[-]
R_g	agglomerate gyration radius	[m]
Re	Reynolds number based on the nozzle diameter	[-]
Re_p	particulate Reynolds number based on particle diameter	[-]
RN	random number following uniform distribution between $[0, 1]$	[-]
r_A	agglomerate intern radius	[m]
Sc_T	turbulent Schmidt number	[-]
t	time	[s]

T_f	fluid temperature	$[K]$
U_f	fluid mean velocity	$[\ m.s^{-1}\ ]$
U_p	particle mean velocity	$[\ m.s^{-1}\ ]$
U_w	wind velocity	$[\ m.s^{-1}\ ]$
u_A	agglomerate instantaneous velocity	$[\ m.s^{-1}\ ]$
$u_{A,ts}$	agglomerate terminal settling velocity	$[\ m.s^{-1}\ ]$
u_A^-	agglomerate instantaneous velocity before the collision	$[\ m.s^{-1}\ ]$
u_A^+	new agglomerate velocity after the agglomeration	$[\ m.s^{-1}\ ]$
$u_{f@p}$	fluid velocity 'seen' by particles	$[\ m.s^{-1}\ ]$
u_{fict}	instantaneous velocity of the fictive particle	$[\ m.s^{-1}\ ]$
u_p	particle instantaneous velocity	$[\ m.s^{-1}\ ]$
u_{pp}	primary particle velocity	$[\ m.s^{-1}\ ]$
$u_{p,ts}$	particle terminal settling velocity	$[\ m.s^{-1}\ ]$
u_f'	fluid velocity fluctuation	$[\ m.s^{-1}\ ]$
u_p'	particle velocity fluctuation	$[\ m.s^{-1}\ ]$
u_{fict}'	fictitious particle velocity fluctuation	$[\ m.s^{-1}\ ]$
V_A	agglomerate characteristic volume	$[\ m^3\ ]$
$V_{b,c}$	breakage critical relative velocity	$[\ m.s^{-1}\ ]$
V_{cr}	agglomeration critical relative velocity	$[\ m.s^{-1}\ ]$
V_{pp}	primary particle volume	$[\ m^3\ ]$
V_r	mean relative velocity between particles and fluid	$[\ m.s^{-1}\ ]$
w_p	parcel statistical weight	[-]
w_p^+	parcel statistical weight after agglomeration	[-]
w_p^-	parcel statistical weight before agglomeration	[-]
X_{12}	minimal distance between two particle surfaces	$[\ m\ ]$
x_A	agglomerate mass center	[m]
x_j	position at a point in direction j	[m]
x_p	particle mass center	[m]
x_{pp}	primary particle mass center	[m]
z_s	height of the source	[m]

Greek symbols

α	parameter in agglomerate collision probability coefficient model	[-]
β	parameter in agglomerate drag model	[-]
γ_f	liquid surface tension	$[\ N.m^{-1}\ ]$
δt	time interval	$[\ s\ ]$
δW_i	Weiner process	[-]
Δt	simulation time step	$[\ s\ ]$

Δt_c	collision time	[s]
Δu_f	difference fluid velocity on two positions in agglomerate	[$m.s^{-1}$]
ε_f	fluid turbulence dissipation	[$m^2.s^{-3}$]
η	Kolmogorov scale	[m]
η_r	inverse of the Stokes number	[-]
κ	agglomerate permeability	[m^2]
λ	gas mean free path	[m]
μ_f	fluid dynamic viscosity	[$N.m^{-2}.s$]
ν_f	fluid kinetic viscosity	[$m^2.s^{-1}$]
ν_A	agglomerate Poisson ratio	[-]
ν_p	particle Poisson ratio	[-]
ν_T	turbulent kinetic viscosity	[$m^2.s^{-1}$]
ξ	parameter in agglomerate collision probability coefficient model	[-]
ξ_{gauss}	Random number following Gaussian distribution	[-]
ρ_A	agglomerate density	[$kg.m^{-3}$]
ρ_f	fluid density	[$kg.m^{-3}$]
ρ_p	particle density	[$kg.m^{-3}$]
ρ_{pp}	primary particle density	[$kg.m^{-3}$]
$\sigma_{f\to A}$	fluid stress on agglomerate	[$N.m^{-2}$]
σ_k	constant in $k-\varepsilon$ model	[-]
$\sigma'_{p,i}$	RMS velocity component in i-direction of the particle	[-]
σ_ε	constant in $k-\varepsilon$ model	[-]
σ_{res}	agglomerate tensile strength	[$N.m^{-2}$]
σ_y	standard deviation in ADMS model	[-]
σ_z	standard deviation in ADMS model	[-]
τ_{coll}	collision characteristic time scale	[s]
τ_f	fluid turbulent time scale	[s]
$\tau^t_{f@p}$	turbulent Lagrangian integral time scale "seen" by particles	[s]
τ^{pp}_k	collision time scale between spherical particles	[s]
τ^{AP}_{coll}	collision time scale between agglomerates and spherical particles	[s]
τ^{AA}_{coll}	collision time scale between agglomerates	[s]
τ_p	particle relaxation time	[s]
φ_A	agglomerate solid fraction	[-]
ϕ	angle	[rad]
Ω	drag coefficient correction	[-]
ω_{fr}	breakage frequency	[s^{-1}]

Abreviation

ADMS	Atmospheric Dispersion Modelling System
CFD	Computational Fluid Dynamics
DNS	Direct Numerical Simulation
EAM	Energy - based Agglomeration Model
IMFT	Institut de Mécanique des Fluides de Toulouse
INERIS	Institut National de L'Environnement et des Risques
LES	Large Eddy Simulation
MAM	Momentum - based Agglomeration Model
RANS	Reynold Averaged Navier Stokes

Chapter 1

Introduction

Contents

Nowadays, nanomaterials are more and more used in industrial processes leading to a significant increase in terms of interest and budget [78]. A key issue to protect the population and the environment consists in identifying risk scenario cases related to the use of nanoparticles. An important part of the risk assessment is based on the understanding of dangerous physical phenomena which can occur in case of an accident during the production, the manipulation, the transport and the storage of the product. In the past, a leakage of a conveying pipe in Blanzy (France, 2012) [1] released 5 tons of carbon black into the atmosphere. In order to be able, in the future, to evaluate the consequences of such an accident, a study of this specific case of conveying pipe leakage need to be realized. However, the physical phenomena in nanoparticles jet are still misunderstood. In the literature, some experimentations investigated the nanoparticles behaviors in different configurations such as the free fall [52] or the flow under pressure in a small device [109, 27] but these studies did not propose a model to predict the dispersion and the evolution of the particle size distribution. In parallel, some authors investigated numerically the formation of aggregates composed by nanoparticles in air [53, 118, 25]. These numerical simulations are very computationally expensive and cannot be applied to industrial applications or for risk predictions. In order to predict the behavior of nanoparticle jet, a specific CFD numerical tool needs to be developed to model the physical phenomena related to nanoparticles.

1. https://www.aria.developpement-durable.gouv.fr/accident/43049/

1.1 Industrial context

In the last few years, the nanotechnology sector has rapidly grown worldwide with an important budget investment. According to Lux research [2], $18.5 billion have been invested worldwide in the nanotechnology in 2012. Among this budget, only $40 million were invested in the research regarding negative effects and risks of nanotechnology. According to the BBC research [3], the global nanotechnology market should reach $909.5 billion by 2021 from $39.2 billion in 2016. The *project on emerging nanotechnogies* has identified more than 1800 products [116] based on nanotechnology. In France, since 2012, all producers, distributors or importers have to declare all used, produced and imported quantity of nanomaterials in the market.

The innovation in nanotechnology is often based on materials composed by nanoparticles, called 'nanomaterials'. These nanomaterials have new properties with respect to the same materials composed of microparticles. The new properties are created by the very high specific surface area of nanoparticles. Nanomaterials are applied in different industrial sectors:

- Automobile industry and aeronautics: lighter and faster vehicles with composites, more adhesive paint, longer life tires, etc...
- Electronics and communication industry: batteries with greater autonomy, new solar cells, faster process, ultra fast computers , etc...
- Pharmaceutic, bio-medicine and biotechnology: new drugs and new cosmetic products, sun cream, tissue regeneration, etc...
- Energy: new generation of photo-voltaic panels, better insulating materials, better capacity of solar and wind power, etc...
- Environment and ecology: reduce CO_2 emission, better materials recycle, etc...

However, the use of nanomaterials in the industry also generates risks, as illustrated by the accidents listed in Table 1. Therefore, it is necessary to assess these risks, to evaluate their consequences, implement preventive and protective procedures [129].

1.2 Terms and definitions

In the present study, definitions from the standard ISO/TS 80004-1 2^{nd} edition [1] are used.

- **Nanoscale**: size ranging from approximately 1 nm to 100 nm.
- **Nanomaterial**: material with any external dimension at the nanoscale or having internal structure or surface structure at the nanoscale.
- **Nano-object**: material with one, two or three external dimensions at the nanoscale.
- **Nanostructure**: composition of inter-related constituent parts, in which one or more of those parts is a nanoscale region.

2. https://members.luxresearchinc.com/research/report/13748, consulted day: 21/07/2017
3. https://www.bccresearch.com/market-research/nanotechnology/nanotechnology-market-assessment-report-nan031f.html, consulted day: 21/07/2017

Accident	Causes	Materials / released quantity	Consequences
Norway (1973)	Inadaptation of inerting system of nitrogen - powder explosion	200 kg aluminium and sulfur	5 dead, 4 injured people
Taiwan (2007-2010)	Powder explosion (Crushing aluminium micrometric powder to aluminium nanometric powder)	Aluminium powder, titaninum powder	/
Blanzy, France (2012)	Leakage of conveying pipe in dense phase	5 tons of carbon black	Pollution
Alsace, France (2011)	Accidental spillage of truck	750 kg of titanium dioxide	Pollution
Allemagne (2012)	Accidental spillage of truck	Undefined quantity of nano zinc oxyde	Pollution

Table 1 – A few accidental cases related to nanomaterials in the past.

— **Nanostructured material**: material having internal nanostructure or surface nanostructure.

In the present study, the term *Nanoparticles* is equivalent to the term *Nano-object* defined above. The definition of *Agglomerate* and *Aggregate* are as follows:

— **Agglomerate**: a collection of weakly bound particles or aggregates where the resulting external surface area is similar to the sum of the surface areas of the individual particles

— **Aggregate**: a particle composed of strongly bound or fused particles.

A more comprehensive view of nanoscales is proposed in Figure 1.

1.3 Context of the study

Many reviews were published to comment on the exposure to nanoparticles and its potential impact on human and environment [78]. However, these studies focus on the long term effect with a long exposure and a weak dose. Very few studies investigated on the short term effect with a short exposure and a large dose created by an accidental dispersion of nanoparticles. The main scenarios of accidental risk related to nanoparticles dispersion in the air are identified as follows:

— leakage from a conveying pipe of powder containing nanoparticles yielding the turbulent;

— spill of powder containing nanoparticles where nanoparticles are in free fall;

— resuspension of powder containing nanoparticles by an air flow.

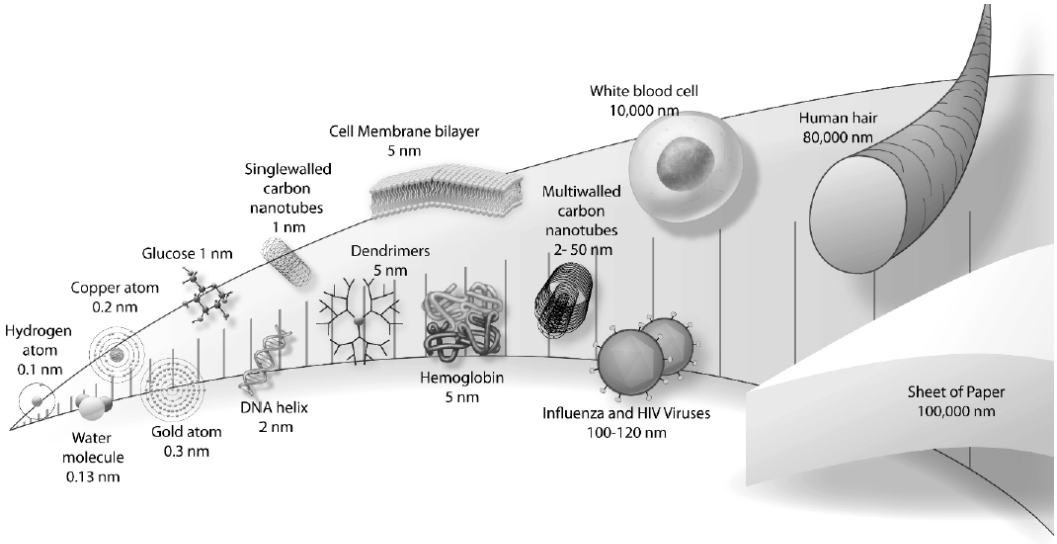

Figure 1 – Nanoscale and some examples [129].

Within the framework of those scenarios, accidental emissions of nanoparticles may cause consequences as follows:

— Exposure of workers and surrounding population to nanoparticles whose potential negative effects are still misunderstood. For example, the nanoparticles may penetrate deeper than microparticles into the lung in case of an inhalation [131].

— Formation of a particle cloud and potentially of an explosive atmosphere (ATEX) when particles are flammable. In the presence of an ignition source, such a leakage would then be followed by an explosion.

In order to estimate quantitatively the consequence of the accidental scenario cases, various tools are used to simulate the hazardous physical or chemical phenomena. Depending on the hazardous phenomena (dispersion, fire or explosion) and on the physical phenomena considered, a specific tool and model needs to be used. The objective of the physical phenomena modelling is to estimate the safety distances to limit the effects on human health and environment. Unfortunately, the physical phenomena of the nanoparticles released in the air are not well understood. In addition, there are no available tools to predict reliably the spatial and temporal evolution of nanoparticles concentration and size distribution in the air. In this context, the specific study of the behavior of nanoparticles jet in the air is necessary. Therefore, the aim of the thesis is as follows:

— To develop a better understanding of physical phenomena related to the nanoparticles jet

— Development of a predictive model for the concentration and size evolution of nanoparticles in the near field.

The present study focuses on the field in the vicinity of the conveying pipe leakage. In

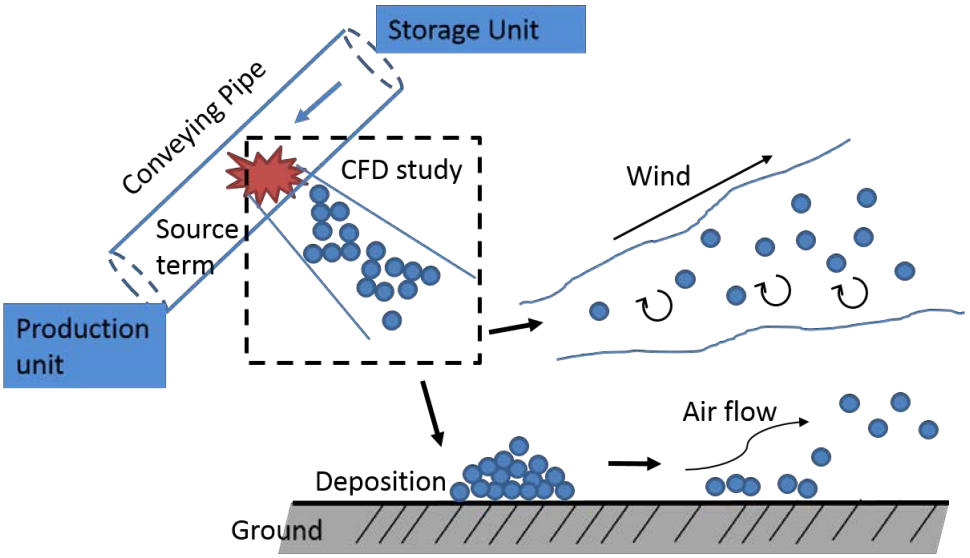

Figure 2 – Schematic representation of the nanoparticle leakage from a conveying pipe. The zone under study is represented by the dashed line.

this near field, there are several physical phenomena needed to be specifically modelled in order to predict the nanoparticle fate in the air (cf. Chapter 2). Those physical phenomena occur in a distance less than a few meters from the leakage and on a time scale of seconds or minutes. Figure 2 shows the configuration of a conveying pipe leakage. The nanoparticles are released into the ambiant air with a jet under pressure after the leakage. The nanoparticle-gas and the inter-nanoparticle interactions have to be taken into account. The turbulence created by the gas flow also needs to be modelled. After that, the nanoparticles jet enters the "far field" where the nanoparticle dispersion is mainly controlled by the wind. Nanoparticles or agglomerates may deposit on the ground and be resuspended by the air flow. Therefore, the results from our study are essential for other studies as nanoparticle atmospheric dispersion and deposition.

The present study focuses on the nanoparticle dispersion related to the use of nanoparticle powder by the industry. Additionally, the behavior of a dense flow of nanoparticles in a conveying pipe is still not well understood. Its modelling is out of the scope of the present study.

Type of powder under study

Different types of nanoparticles have different physical and chemical properties when they are released into the air. The nanoparticles TiO_2 are used extensively, mostly for their photocatalytic and anti-UV properties in paints, plastics, foods, pharmaceuticals and cosmetics and other products [124]. The properties of TiO_2 can be found in the literature and in several experimental works which investigated the behavior of TiO_2 in the air [52, 109]. Therefore, solid nanoparticles of TiO_2 are chosen in the present study as the reference material. This choice of powder allows the investigation of physical phe-

nomena with realistic values of the solid material properties (as the density, the Hamaker constant, etc...). The study is applied for all other studies with another solid nanoparticles having the same physical phenomena (cf. Chapter 2) as the solid nanoparticles TiO_2, for example, the carbon black particles type in case of the accidental leakage in Blanzy, France.

1.4 Thesis outline

Due to the increase of computer power, CFD numerical simulations (*Computational Fluids Dynamics*) has become recently a powerful tool for research and engineering applications. CFD can provide important information that can be very complicated to be achieved through experimental measurements. In the present study, the CFD tool used is *Code_Saturne* developed by EDF (Électricité de France). This choice is based on a good evaluation of the results from *Code_Saturne* with experimental data in microparticles jet case (cf. Appendix B). Code_Saturne is an open source code with a good potential to model the nanoparticles physical phenomena presented hereafter.

The first step of the study summarizes the physical phenomena related to nanoparticles in the air. These physical phenomena are analyzed in order to select physical phenomena that appear predominant in the present configuration. The second step consists in the modelling of the physical phenomena chosen for the numerical simulation tool. Finally, the third step consists in the numerical simulation of an accidental case of a conveying pipe leakage. The following chapters are :

— *Chapter 2*: state of the art of physical phenomena related to nanoparticles.
— *Chapter 3*: modelling physical phenomena related to nanoparticles.
— *Chapter 4*: numerical simulation of an accidental pipe leakage.
— *Chapter 5*: conclusions and perspectives

Chapter 2

State of the art of physical phenomena related to nanoparticles

Contents

This chapter is dedicated to the description of physical phenomena taking place when nanoparticles are transported by a turbulent air flow. Because of the complexity of those physical phenomena, the aim of this chapter is to estimate their relative importance in the present study. This evaluation was done with simple models in order to select the main physical phenomena to take into account. First, the physical parameters which describe the agglomerate shape are presented. After that, the fluid and particulate phase modelling is explained. Then, the interaction between the fluid and the agglomerate as the drag force, the Brownian motion, the agglomerate breakage by the fluid are described. Then, the interaction between agglomerates as the collision, the agglomeration and the agglomerate breakage by the collision are detailed. Finally, other physical phenomena as the aggregation, the nucleation, the condensation, the vaporization and the chemical reaction are briefly presented.

2.1 Characterization of agglomerates

Under atmospheric conditions, nanoparticles form agglomerates because of interaction forces between nanoparticles. As already defined in the previous chapter, an agglomerate is formed by an assembly of primary particles linked to each other by weak forces. Particles which constitute agglomerates are called primary particles. This section is dedicated to the characterization of the nanoparticle agglomerates.

2.1.1 Interactions between primary particles

Depending on different conditions of the carrier phase, agglomerates could be formed by different forces as the Van der Waals force, the capillary force, the electrostatic force, the solid bridge force. Figure 3 [101] shows the comparison between different interparticle forces in function of the particle diameter. Seville [101] showed that, in air, the electrostatic force is very weak compared to the Van der Waals force and the capillary force. Therefore, electrostatic interactions can be safely neglected in the present study. Although, it is interesting to note that in some powder handling processes where the collision between the particles and a wall becomes very frequent, the particles may be charged by the frictional contact. This phenomenon is called the triboelectric charging (see Matsusaka et al. [77] for more information). The solid bridge force is formed by the fusion of primary particles at very high temperature. Therefore, the solid bridge cannot be formed at the atmospheric temperature and is neglected in the present study. In the following, we introduce only the Van der Waals force and the capillary force which are the main interactions between primary particles in an agglomerate.

The Van der Waals force is an attractive force which forms a weak bond between particles. In case of two spherical particles of different diameters d_{p1} and d_{p2}, the Van der Waals force reads:

$$\mathbf{F}_{vdw} = \frac{A}{12X_{12}^2}\frac{d_{p1}d_{p2}}{d_{p1}+d_{p2}} \tag{2.1.1}$$

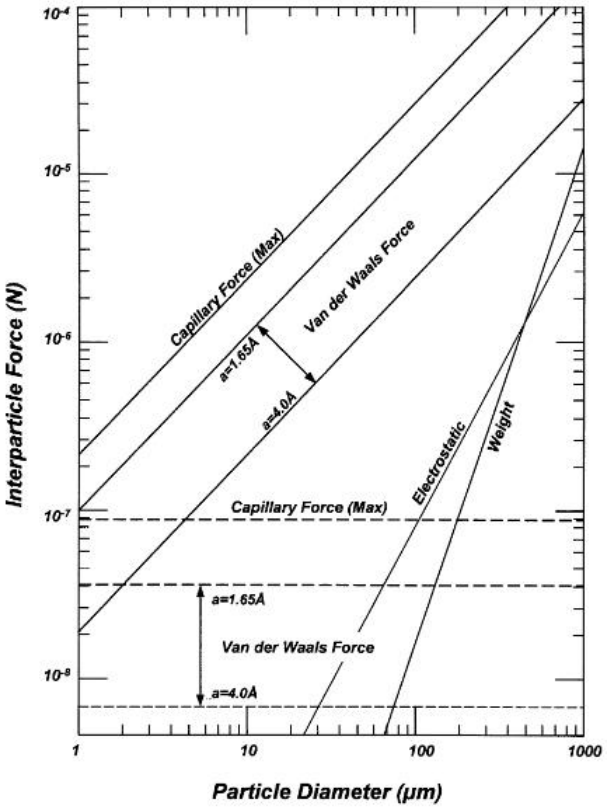

Figure 3 – Comparison of magnitude of interparticle forces. Theoretical interparticle forces for single-point contact between equal spheres (in air), with particle weight plotted for comparison [101].

where A is the Hamaker's constant. X_{12} is the distance between the two particle surfaces. It can be easilly seen from Eq. (2.1.1) that when the two particles are in contact, $X_{12} \to 0$, and the force tends to infinity. Therefore, a minimum distance of Van der Waals force $X_{12}^{min} \approx 0.4\ nm$ is generally considered . Details about the influence of the choice of X_{12}^{min} are discussed in Abbasfard et al.[2]. Some experimental values of the Hamaker's constant are given in Table 2 [34].

Considering two approaching particles in a humid environment, a thin layer of liquid could be formed between the two particle surfaces. As for the Van der Walls force, the capillary force, created by the liquid bridge, is an attractive force. The liquid bridge formation depends on the carrier phase humidity and the particle surface properties. This physical phenomenon is sketched in Figure 4.

The capillary force is approximated as follows [87]:

$$\mathbf{F}_{capil} \approx -\pi d_p \gamma_f cos\phi \tag{2.1.2}$$

Compound	A x 10^{-20} J	Compound	A x 10^{-20} J
Water	4.4	Al_2O_3	14.8
NaCl	6.6	Metal (Au,Ag,Cu)	25-40
KCl	5.6	Polystyrene	7.2
Carbon	30.7	Hydrocarbon	4-10
Ethanol	4.2	TiO_2	14.6
$CaCO_3$	3.0	Acetone	2.9

Table 2 – Example of Hamaker's constant value for several compounds. The data is extracted from [34].

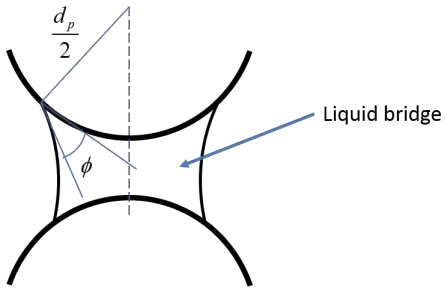

Figure 4 – Schematic representation of the liquid bridge between two spherical particles.

where γ_f is the liquid surface tension. Considering both water and air at 20°C, the surface tension is $\gamma_f = 73.10^{-3} N.m^{-1}$. In Eq. (2.1.2), ϕ is the contact angle between the liquid bridge and the surface as shown in Figure 4.

The capillary force between spherical particles can also be estimated by an experimental method [49]:

$$\mathbf{F}_{capil} = 0.063 d_p (1 + 0.009 R.H.) \tag{2.1.3}$$

where $R.H.$ is the relative humidity.

Recently, Balakin et al. [9] used an Euler - Lagrangian approach to simulate the agglomeration of solid particles taking into account the liquid bridge force. Ding et al., 2015 [27] studied the influence of the humidity on the agglomerate breakage. Despite of numerous researches in the literature focusing on this topic, the role of the capillary force in the agglomeration and the agglomerate strength is still misunderstood. None of the models in the literature could predict such a physical phenomenon with a good accuracy.

2.1.2 Description parameters of agglomerates

In this section, several parameters which describe the agglomerate properties are presented.

The agglomerate mass center, $\mathbf{x}_A$, is defined as the mean of all primary particle mass

center in agglomerate:

$$\mathbf{x}_A = \frac{\sum_i^{N_{pp}} m_{pp,i}\, \mathbf{x}_{pp,i}}{\sum_i^{N_{pp}} m_{pp,i}} \tag{2.1.4}$$

where $\mathbf{x}_{pp,i}$ is the mass center of primary particle i and $m_{pp,i}$ is its mass. In Eq(2.1.4), N_{pp} is the number of primary particles in the considered agglomerate.

The agglomerate velocity, $\mathbf{u}_A$, is defined as follows:

$$\mathbf{u}_A = \frac{\sum_i^{N_{pp}} m_{pp,i}\mathbf{u}_{pp,i}}{\sum_i^{N_{pp}} m_{pp,i}} \ . \tag{2.1.5}$$

In the present study, the rotation and the deformation of the agglomerates are not considered. Hence, the agglomerate velocity u_A is equal to the primary particles velocity u_{pp}.

Because of the non spherical shape of agglomerates, several agglomerate radius can be defined:

— *Interception radius*, R_0, (in some study, called *the outer radius*) corresponds to the maximum distance between the primary particle (including the surface) and the agglomerate mass center.

— *Gyration radius*, R_g, is the average distance between the primary particles mass center and the agglomerate mass center. It is given by:

$$R_g = \frac{\sqrt{\sum_i^{N_{pp}} \left[m_{pp,i}\left(\mathbf{x}_{pp,i} - \mathbf{x}_A\right)\right]^2}}{\sum_i^{N_{pp}} m_{pp,i}} \tag{2.1.6}$$

— *Internal radius*, r_A, is the radius that ranging between primary particle radius and the agglomerate interception radius. It must be noted that the internal radius is not a given value but a variable generally used for the internal quantity representation within an agglomerate.

All defined radius are presented in Figure 5. In the present study, most of the models are represented as a function of the agglomerate interception diameter instead of the agglomerate interception radius. The characteristic agglomerate diameter d_A considered here is based on the agglomerate interception radius: $d_A = 2R_0$.

Due to the complex shape of the agglomerates, the agglomerate volume is quite difficult to be defined. One simple way is to define the agglomerate volume as the sum of the volumes of each primary particles composing the agglomerate:

$$V_A = \frac{1}{N_{pp}} \sum_i^{N_{pp}} V_{pp,i} \tag{2.1.7}$$

A second simple definition is to consider the agglomerate as a sphere with one of the radius defined in the previous section. The agglomerate volume can be defined by the interception diameter:

$$V_A = \frac{\pi d_A^3}{6}. \tag{2.1.8}$$

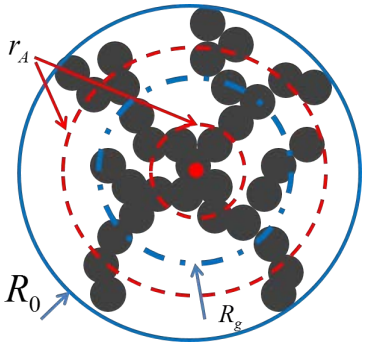

Figure 5 – Schematic representation of the interception radius R_0, the gyration radius R_g and the internal radius r_A.

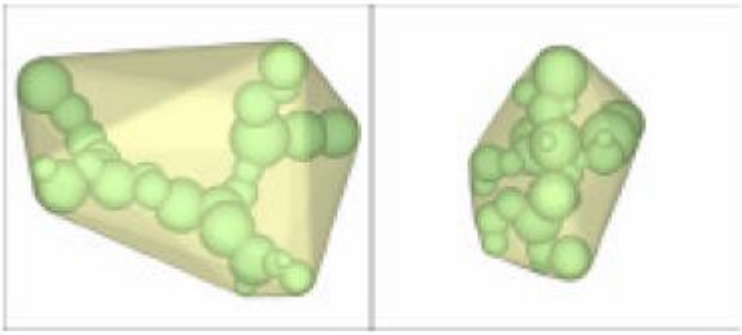

Figure 6 – Agglomerate volume defined by the convex hull enwrapping the agglomerate. Picture from Dietzel et al. [26].

In the present study, Eq. (2.1.8) is chosen to define the agglomerate volume because the agglomerate interception diameter was chosen previously. However, Dietzel et al. [26] proposed to define the agglomerate volume as the convex hull enwrapping the agglomerate but this determination of this volume needs a specific numerical method. Such a convex hull is shown by Figure 6.

From experimental data, Forrest & Witten [33] proposed a relation between the agglomerate mass and its characteristic radius. This relation is expressed as a power law as follows:

$$m_A \approx R_0^{D_f} \ . \tag{2.1.9}$$

where D_f is the Haussdorff dimension or the fractal dimension of the agglomerate. The fractal dimension allows to characterize the structure of the agglomerate as:

— If $D_f \to 1$, the agglomerate has a chain structure.
— If $D_f \to 2$, the agglomerate has a plane disk structure.
— If $D_f \to 3$, the agglomerate has a sphere structure.

Following [117], the number of primary particles, N_{pp}, can be written in terms of the

fractal dimension:

$$N_{pp} = K_f \left(\frac{d_A}{d_{pp}} \right)^{D_f} \tag{2.1.10}$$

where K_f is the structure coefficient that can be expressed as [117]:

$$K_f = 0.414 D_f - 0.211 \ . \tag{2.1.11}$$

The Eq. (2.1.11) is valid for $1.5 < D_f < 2.75$. As discussed by Sorensen [108, 107], when the primary particle number tends to unity, the agglomerate is a sphere and does not have a fractal form. The author proposed that the limit for using the fractal model is $N_{pp,min} = 3$. Up to now, there is no model in the literature which describes the modification of the fractal dimension after the agglomeration or the breakage. Hence, the fractal dimension is considered constant in the present study.

The solid volume fraction in an agglomerate is defined as:

$$\varphi_A = \frac{N_{pp} V_{pp}}{V_A} \tag{2.1.12}$$

where V_{pp} is the primary particle volume. Eq. (2.1.10) & Eq. (2.1.12) lead to:

$$\varphi_A = K_f \left(\frac{d_A}{d_{pp}} \right)^{D_f - 3} \tag{2.1.13}$$

From the agglomerate volume fraction, the agglomerate density is computed as follows:

$$\rho_A = \varphi_A \rho_{pp} + (1 - \varphi_A) \rho_f \tag{2.1.14}$$

where ρ_{pp} is the primary particle density and ρ_f is the fluid density.

2.2 Interaction between fluid and agglomerates

Two families of approaches exist for the numerical simulation of turbulent flows transporting a dispersed phase: the Euler-Lagrange approach and the Euler-Euler approach. Following the Euler-Euler approach, all phases are treated as continuous phases and coupled through interphase momentum transfer terms. Generally, the fluid phase turbulence is modelled according to the Reynolds Average Navier-Stokes (RANS) approach namely $k_f - \varepsilon$ model or $R_{f,ij} - \varepsilon$ model. For the discrete phase, the continuous equations are derived in the framework of the kinetic theory of granular flows [102]. Such an approach has been widely used for the numerical simulation of particulate flows. However, when the particle diameter evolves, as in nanoparticle flows, such a method requires very specific developments [80, 67, 130]. In contrast, the Euler-Lagrange approach is more easily adapted because each particle is tracked individually and may have a given evolving diameter. However, in industrial applications, the number of particles is so large that it is not possible to track all real particles. An approach consists in tracking a limited

number of "numerical particles", also called *parcels*, representing a given number of real particles [32]. In Euler-Lagrange approach, the fluid phase can be either simulated by RANS [68], LES (Large Eddy Simulation) [120] or DNS (Direct Numerical Simulation) [91]. Each approach requires a specific numerical treatment of the inter-phase coupling terms especially for the transfer of momentum.

In the present study, the Euler-Lagrange approach has been selected and adapted for modelling nanoparticle flows. In case of the particle-laden flows, the dispersed phase may modify the fluid phase dynamics. Elghobashi [30] and later Gore & Crowe [37] discussed the influence of the particles on the fluid. They identified three different regimes:

— *One-way coupling*: the influence of the particulate phase on the fluid phase is negligible. This consideration can be applied for the case of a very dilute particulate phase when the particulate volume fraction, α_p, is in order of $\alpha_p < 10^{-6}$.

— *Two-way coupling*: the influence of the particulate phase on the velocity and the fluid turbulence should be considered. This case is considered in the limit of the dilute/dense phase with $10^{-6} < \alpha_p < 10^{-3}$.

— *Four-way coupling*: in this case, the interaction between particles and the influence of the particulate phase on the fluid phase should be considered. This regime corresponds to dense phase with $\alpha_p > 10^{-3}$.

2.2.1 Fluid phase and turbulence modelling

The mass conservation equation for the fluid phase is written as:

$$\frac{\partial \rho_f}{\partial t} + \frac{\partial \rho_f \mathbf{U}_{f,j}}{\partial x_j} = 0 \tag{2.2.1}$$

where ρ_f is the fluid density, and $\mathbf{U}_f$ the mean fluid velocity. The momentum conservation equation for the fluid phase is written as:

$$\frac{\partial \mathbf{U}_{f,i}}{\partial t} + \mathbf{U}_{f,j}\frac{\partial \mathbf{U}_{f,i}}{\partial x_j} = -\frac{1}{\rho_f}\frac{\partial P}{\partial x_i} + \mathbf{g}_i + (\nu_f + \nu_T)\frac{\partial^2 \mathbf{U}_f}{\partial x_j \partial x_j} \tag{2.2.2}$$

where $\mathbf{g}_i$ is the gravity acceleration, ν_f is the molecular diffusion, ν_t the turbulent viscosity which is evaluated as follows:

$$\nu_T = C_\mu \frac{k_f^2}{\varepsilon_f} \tag{2.2.3}$$

with $C_\mu = 0.09$ is the model constant. In a turbulent jet, molecular diffusion is very weak compared to the turbulent diffusion $\nu_f \ll \nu_T$, the molecular diffusion is negligible in the present study.

To model the fluid turbulence, several models are available in the literature as two equations models $k_f - \varepsilon_f, k_f - \omega$ and many others. In the present study, the $k_f - \varepsilon_f$ model proposed by Launder & Spalding [69] is used. The transport equation for the kinetic energy k_f is as follows:

$$\rho_f \left[\frac{\partial k_f}{\partial t} + \mathbf{U}_{f,j}\frac{\partial k_f}{\partial x_j}\right] = \frac{\partial}{\partial x_j}\left(\rho_f \frac{\nu_T}{\sigma_k}\right)\frac{\partial k_f}{\partial x_j} + P_k - \rho_f \varepsilon_T \tag{2.2.4}$$

In Eq. (2.2.4),

— The first term in the right hand side represents the turbulent diffusion.

— The second term in the right-hand-side is the turbulence production by the fluid velocity gradient $P_k = \langle u'_{f,i} u'_{f,j} \rangle_f \frac{\partial \mathbf{U}_{f,i}}{\partial x_j}$.

— The third term in the right-hand-side represents the fluid dissipation.

The transport equation for the fluid turbulent dissipation reads:

$$\rho_f \left[\frac{\partial \varepsilon_f}{\partial t} + \mathbf{U}_{f,j} \frac{\partial \varepsilon_f}{\partial x_j} \right] = \frac{\partial}{\partial x_j} \left[\rho_f \frac{\nu_T}{\sigma_\varepsilon} \frac{\partial \varepsilon_f}{\partial x_j} \right] \tag{2.2.5}$$

$$- \rho_f \frac{\varepsilon_f}{k_f} \left[C_{\varepsilon,1} \langle u'_{f,i} u'_{f,j} \rangle_f \frac{\partial \mathbf{U}_{f,i}}{\partial x_j} + C_{\varepsilon,2} \varepsilon_f \right] \tag{2.2.6}$$

In this equation,

— The first term in the right hand side represents the turbulent diffusion of the dissipation.

— The second term in the right hand side represents the destruction by the fluid gradient velocity and the turbulence production.

The constants of the $k_f - \varepsilon_f$ model are gathered in Table 3.

C_μ	$C_{\varepsilon 1}$	$C_{\varepsilon 2}$	σ_k	σ_ε
0.09	1.44	1.92	1.0	1.3

Table 3 – Constants used in the $k_f - \varepsilon_f$ model [69].

2.2.2 Lagrangian approach for the particulate phase

Here, the equations governing the motion of a dispersed phase are described. As previously explained, the dispersed phase is represented by parcels and a parcel can be either a primary particle, $p \equiv pp$, or an agglomerate $p \equiv A$. The Lagrangian approach consists in tracking each parcel in a Lagrangian frame of reference. Assuming that only the drag and the gravity forces are acting on the particle, the governing equations for the center of mass and the velocity of a particle read:

$$\frac{d\mathbf{x}_p}{dt} = \mathbf{u}_p \tag{2.2.7}$$

$$\frac{d\mathbf{u}_p}{dt} = -\frac{\mathbf{u}_p - \mathbf{u}_{f@p}}{\tau_p} + \mathbf{g} \tag{2.2.8}$$

where $\mathbf{u}_{f@p}$ is the locally undisturbed fluid velocity at the particle position, and τ_p is the particle relaxation time. Such a timescale represents the time required for a particle to adjust its velocity to the carrier phase velocity. The particle relaxation time writes:

$$\tau_p = \frac{4}{3} \frac{\rho_p}{\rho_f} \frac{d_p}{C_d ||\mathbf{u}_p - \mathbf{u}_{f@p}||} \tag{2.2.9}$$

with C_d is the drag coefficient (see hereafter).

When a RANS approach is coupled with a Lagrangian approach, a model is needed for the turbulent dispersion. Indeed, in one hand, the RANS approach gives only the predictions of the mean fluid flow through the mean fluid velocity and the mean fluid agitation. On the other hand, the particle momentum equation, Eq. (2.2.8), needs the instantaneous fluid velocity at the particle position. In the literature, several models can be founded (Gosman & Ioannides [38], Minier et al. [83], Simonin [102], Oesterle & Petitjean [88]).

In case of an homogeneous isotropic turbulent flow, Simonin et al. [102] proposed to model the fluid velocity at the particle position by a Langevin equation as:

$$u_{f,i}(\mathbf{x}_p + \mathbf{u}_d\delta t, t+\delta t) - u_{f,i}(\mathbf{x}_p, t) = -\frac{1}{\tau^t_{f@p}} u_{f,i}(\mathbf{x}_p, t)\delta t + \sqrt{\frac{4}{3}\frac{q^2_{f@p}}{\tau^t_{f@p}}}\delta W_i \tag{2.2.10}$$

where $\tau^t_{f@p}$ is the Lagrangian integral time scale seen by the particles, $q^2_{f@p}$ the fluid agitation at the particle position and δW_i a Weiner process. For the numerical implementation of such a stochastic differential equation, we use a first order scheme. The numerical method of the velocity "seen" by particles can be shown as follows:

$$u^{n+1}_{f,i} = u^n_{f,i}\left[1 - \frac{\Delta t}{\tau^t_{f@p}}\right] + \sqrt{\frac{4}{3}\frac{q^2_{f@p}}{\tau^t_{f@p}}}\Delta t \xi_{gauss} \tag{2.2.11}$$

where ξ_{gauss} is a random number following a Gaussian distribution of zero mean and a standard deviation of 1.

2.2.3 Drag force on agglomerates

The drag force on a spherical particle has been extensively investigated [19, 97]. Basically, the drag force depends on the particle Reynolds number:

$$Re_p = \frac{||\mathbf{u}_p - \mathbf{u}_{f@p}||d_p}{\nu_f} \ . \tag{2.2.12}$$

When the particulate Reynolds number is low ($Re_p \ll 1$), the drag coefficient reads:

$$C_d = \frac{24}{Re_p} \tag{2.2.13}$$

and the particle relaxation timescale in a gas ($\rho_p \gg \rho_g$), Eq. (2.2.9), becomes:

$$\tau_p = \frac{\rho_p d_p^2}{18\mu_f} \tag{2.2.14}$$

For the intermediate particle Reynolds number ($1 < Re_p < 1000$), the drag coefficient can be modelled by using the expression proposed by Schiller & Naumann [97]. However, the nanoparticles and the agglomerates considered in the present study are always

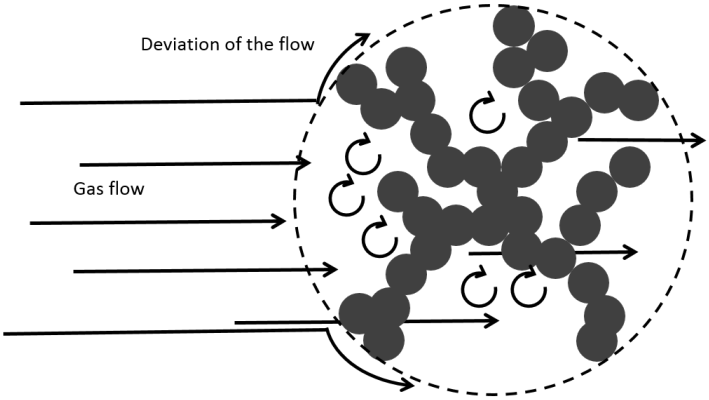

Figure 7 – Schematic description of the fluid passing through the agglomerate because of the agglomerate porosity.

considered in Stokes regime meaning that the particle response timescale is given by Eq. (2.2.14).

In case of an agglomerate, the fluid can pass through the agglomerate (see Figure 7). Obviously, in such a case the drag force is strongly modified. Vanni [117], Chernyakov et al. [18], Kim et al. [57] and Vainshtein [114] proposed the following expression for the drag coefficient of an agglomerate:

$$C_{d,A} = C_d \Omega \tag{2.2.15}$$

where $C_{d,A}$ is the agglomerate drag coefficient assuming a spherical shape of the agglomerate and Ω is a correction coefficient. The correction coefficient takes into account the agglomerate fractal dimension and therefore, the agglomerate porosity. However, Vanni [117] shows that taking into account the heterogeneity of the porosity is relevant only for a fractal dimension $D_f \leq 2$. In the present study, the agglomerate porosity is assumed uniform. For more information about the influence of the uniform porosity hypothesis on the drag force for agglomerates, the reader can refer to the study of Vainshteain et al. [115]. Following Vanni [117], the correction coefficient is modeled as follows:

$$\Omega = \frac{2\beta^2(\beta - tanh\beta)}{2\beta^3 + 3(\beta - tanh\beta)} \tag{2.2.16}$$

where $\beta = d_A/(2\sqrt{\kappa})$ and κ is the agglomerate permeability. It can be noted that Eq. (2.2.16) has been validated by comparison with experimental data [75]. The agglomerate permeability represents the capability of the agglomerate to let the flow passing through it. The simplest model, also named the dilution limit model, estimates the agglomerate permeability by considering that primary particles are not in contact with each other:

$$\kappa = \frac{1}{18}\frac{d_{pp}^2}{\varphi_A} \tag{2.2.17}$$

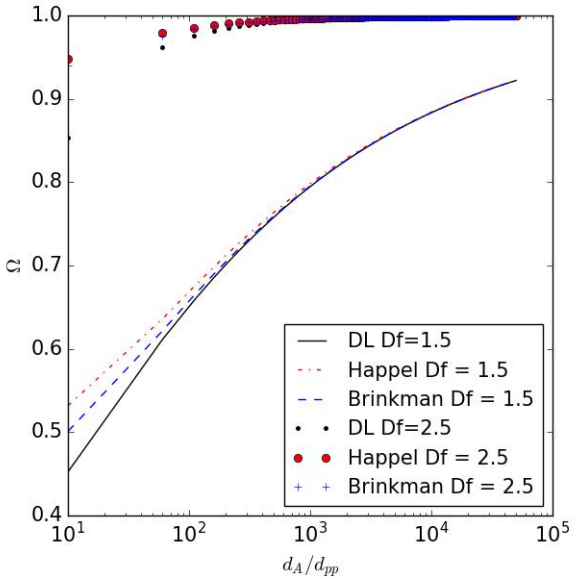

Figure 8 – Drag coefficient correction with respect to the agglomerate diameter. DL: Dilution limit Eq. (2.2.17), Happel: Eq. (2.2.19), and Brinkman: Eq. (2.2.18).

Brinkman [13] proposed the relation following by taking into account the interaction between primary particles:

$$\kappa = \frac{d_{pp}^2}{18\varphi_A}\left[1 + \frac{3}{4}\varphi_A\left(1 - \sqrt{\frac{8}{\varphi_A} - 3}\right)\right] \tag{2.2.18}$$

When the agglomerate solid volume is very high, Happel [45] proposes to calculate the permeability as follows :

$$\kappa = \frac{d_{pp}^2}{18\varphi_A}\frac{\left(6 - 9{\varphi_A}^{1/3} + 9{\varphi_A}^{5/3} - 6{\varphi_A}^2\right)}{\left(6 + 4{\varphi_A}^{5/3}\right)} \tag{2.2.19}$$

In Eq. (2.2.19), the agglomerate solid fraction is calculated with Eq. (2.1.13) which takes into account the fractal dimension D_f. Figure 8 shows the drag correction coefficient computed with three permeability models: Eq. (2.2.17), Eq. (2.2.18) and Eq. (2.2.19) with $D_f = 1.5$ and $D_f = 2.5$.

The trend and the order of Ω are in good agreement with the results of Vanni [117]:

— Ω is always smaller than 1, $C_{d,A} < C_d$ which indicates that the drag force on agglomerates is always smaller than the drag force on spherical particles of the agglomerate interception diameter.

— Ω increases when d_A/d_{pp} increases with a constant fractal dimension D_f. Ω increases when D_f increases with a constant d_A/d_{pp}.

— For $D_f = 2.5$, the results from Happel model and Brinkman model are similar. The dilution limit model underestimates Ω in comparison with the other two models. This difference is observed because the dilution limit model does not takes into account the influence between primary particles which becomes important when the agglomerate is compact.

For the Happel model, the author used a "sphere-in-cell" approximation, i.e., a particle very dense in the center having a porous cell. This approximation is similar to the agglomerate structure considered in the present study. Additionally, Masliyah et al [75] validated the coefficient correction model, Eq. (2.2.16), by using Happel's model to calculate the agglomerate permeability. Therefore, Happel model is used in the present study.

2.2.4 Brownian motion

For very small particles, typically at nanoscale, the Brownian motion needs to be considered. The Knudsen number permits to evaluate the importance of the Brownian motion. Such a dimensionless number compares the fluid mean free path, λ, to the agglomerate diameter:

$$Kn = \frac{2\lambda}{d_A} \tag{2.2.20}$$

The fluid mean free path is the averaged distance of the fluid molecules between two collisions. For air under a normal conditions of $T = 293\ K$ at $1\ atm$, $\lambda \approx 65$ nm [99].

From a macroscopic point of view, the Brownian motion can be modeled by a diffusion phenomenon [34]:

$$D_{Br} = C_c D_{SE} \tag{2.2.21}$$

where D_{Br} is the Brownian diffusion coefficient, D_{SE} is the Stokes-Einstein diffusion coefficient:

$$D_{SE} = \frac{k_B T_f}{3\pi\mu_f d_p} \tag{2.2.22}$$

with k_B is the Boltzmann constant, T_f is the fluid temperature, μ_f is the fluid dynamic viscosity. In Eq. (2.2.21), C_c is the slip correction factor called the Cunningham coefficient. Following [34], the Cunningham coefficient is computed as follows:

$$C_c = 1 + \frac{2\lambda}{d_p}\left[A_1 + A_2 \exp\left(\frac{-A_3 d_p}{2\lambda}\right)\right] . \tag{2.2.23}$$

From experimental data, Kim et al., [58] proposed the following set of parameters $A_1 = 1.165; A_2 = 0.483; A_3 = 0.997$ for a nanoparticle in air under standard atmospheric condition of $T = 293\ K$ and $1\ atm$.

For nanoparticles released as a jet in the atmosphere, the particle or agglomerate motion may be strongly influenced by the jet turbulence. It is interesting to compare the turbulent diffusion to the Brownian diffusion. Using the definition of the turbulent

Schmidt number $Sc_T = \nu_T/D_T$ and considering that Sc_T is known, the turbulence diffusion D_T is evaluated as follows:

$$D_T = \frac{\nu_T}{Sc_T} \tag{2.2.24}$$

where Sc_T is considered to be equal to 1, ν_T is the turbulent viscosity. The fluid turbulent dissipation is calculated as:

$$\varepsilon_f = 0.09\frac{k_f^{3/2}}{l_T} \tag{2.2.25}$$

where l_T is the turbulence length scale describing the size of the large turbulent eddies. Here, the turbulent length scale is chosen as $l_T \approx 0.15 D_{nozzle}$ with D_{nozzle} is the nozzle diameter. The fluid agitation is related to the turbulence intensity by experimentation of the turbulent jet. The experimental data have shown that the turbulence intensity ranges from 2% [41] to 12% [11]. The numerical parameter considered for the comparison between the turbulent diffusion and the Brownian diffusion is presented in Table 4. Figure 9 shows the turbulent diffusion, Eq. (2.2.24), normalized by the Brownian diffusion coefficient, Eq. (2.2.21) with respect to the particle diameter. The result shows that turbulent diffusion is always larger than Brownian diffusion. Based on that result, the Brownian motion is neglected in the present study. However, it is important to note that in other configurations as the free fall or the deposition of nanoparticle agglomerates, turbulence diffusion can be very weak and the Brownian diffusion should be considered.

Temperature	293.5 K
Viscosity μ_{air}	$1.85 \times 10^{-5} kg.m^{-1}.s^{-1}$
Mean free path in air λ	$6.5 \times 10^{-8} m$
Turbulence intensity I	5%
Jet velocity	10 m/s
Nozzle diameter	1.5×10^{-2} m
Turbulent Schmidt number Sc_t	1

Table 4 – Gas and particle properties for evaluating the Brownian diffusion and the turbulent diffusion.

2.2.5 Agglomerate breakage by interaction with the fluid

In this section, the agglomerate breakage by the hydrodynamic stress induced by the fluid on the agglomerate structure is presented. The agglomerate breakage resulting from a collision between two agglomerates (or with a primary particles) will be presented in Chapter 2.3.3. Figure 10 shows the configuration of the agglomerate breakage by the fluid. The breakage has a strong influence on the agglomerate size distribution which

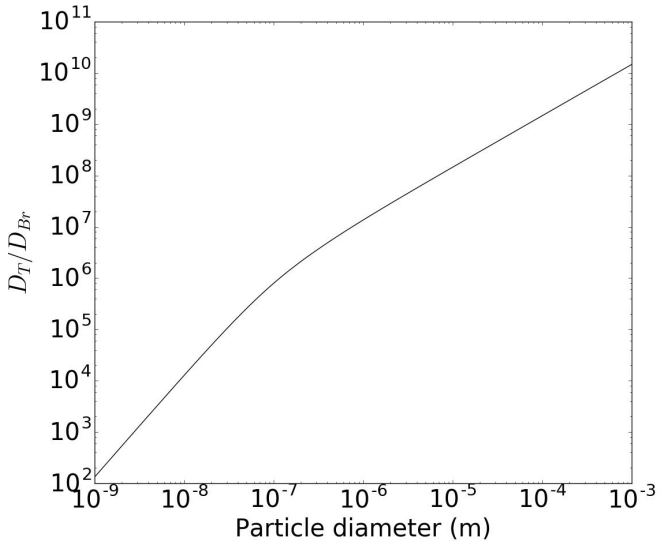

Figure 9 – Turbulent diffusion normalized by Brownian diffusion with respect to the particle diameter.

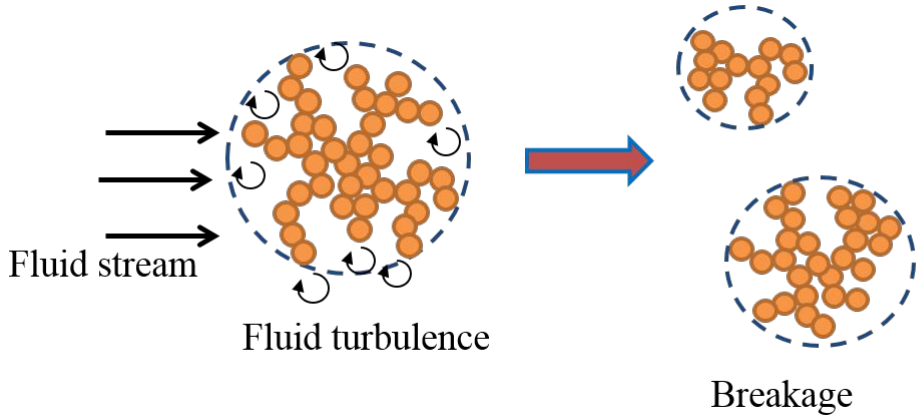

Figure 10 – Schematic representation of hydrodynamic agglomerate breakage by a fluid flow.

is very important in the dispersion. Then, such a physical phenomenon appears as a key issue that required to be modeled as precisely as possible. In the literature, the breakage of droplets in a turbulent flow has been extensively studied and quite well understood [22, 71]. In contrast, the agglomerate breakage is not well known because of the complexity in the prediction of the adhesive forces within an agglomerate. To model the agglomerate breakage phenomenon, two pieces of information are required:

— the breakage occurrence condition or rate.

— the breakage resulting number, size and velocity.

Two approaches for breakage occurrence are founded in the literature: a deterministic approach and a probabilistic approach.

2.2.5.1 Deterministic approach for the agglomerate breakage

The main idea of the deterministic approach is based on the comparison between the stress exerted by the fluid on the agglomerate and the agglomerate strength:

$$R_{Frag,A} = \frac{\sigma_{f\to A}}{\sigma_{res}} \tag{2.2.26}$$

where $\sigma_{f\to A}$ is the stress exerted by the fluid on the agglomerate and σ_{res} is the agglomerate tensile strength. If the dimensionless number $R_{Frag,A} > 1$, the breakage occurs. To estimate the agglomerate strength, Rumpf [15] [121] proposed the following model:

$$\sigma_{res} = \frac{9}{8}\frac{k_c \varphi_A F_{vdw}}{\pi d_{pp}^2} \tag{2.2.27}$$

In Eq. (2.2.27), only the Van der Walls forces have been retained as an adhesive force. This force is computed by Eq. (2.1.1). k_c is the mean coordination number in the agglomerate that represents the mean number of contact between the primary particles. The coordination number can be computed by the empirical model as follows [126, 65]:

$$k_c = 14.64{\varphi_A}^{1/2} \tag{2.2.28}$$

It is important to note that this model is based on a uniform solid fraction hypothesis inside agglomerates. Some approaches can go further than this hypothesis such as in [105].

When the agglomerate size is smaller than the Kolmogorov length scale, $\eta = (\nu_f^3/\varepsilon_f)^{1/4}$, the turbulent stress of the fluid on the agglomerate is calculated as follows [20, 93, 106]:

$$\sigma_{f\to A} = \frac{5}{2}\mu_f\sqrt{\frac{\varepsilon_f}{\nu_f}} \tag{2.2.29}$$

When the agglomerate is larger than the Kolmogorov length scale. The turbulent stress is then estimated by [20]:

$$\sigma_{f\to A} = \rho_f C_{IS}(\varepsilon_f d_A)^{2/3} \tag{2.2.30}$$

where $C_{IS} = 0.7$ is the model constant.

2.2.5.2 Probabilistic approach for the agglomerate breakage

Similarly to the study of the droplet breakage [21], the probabilistic approach for the agglomerate breakage is based on the breakage frequency which is defined as follows:

$$\omega_{fr} = \frac{1}{\tau_{fr}}\frac{N_{A,fr}}{N_A} \tag{2.2.31}$$

where, $N_{A,fr}/N_A$ is the fraction of agglomerates having a breakage during a duration τ_{fr}. Following the study of Delichatsios et al.[22] on the droplet breakage, Kuster [66] proposed a model of the breakage frequency for the agglomerate breakage as follows:

$$\omega_{fr} = \left(\frac{2}{\pi}\right)^{1/2} \frac{\Delta u_f}{d_A} exp\left(\frac{-V_{b,c}^2}{2\Delta u_f^2}\right) \tag{2.2.32}$$

where $V_{b,c}$ is a breakage critical velocity and $\Delta u_f/d_A$ represents the stress of the fluid acting on agglomerate. This term is expressed with Δu_f, the difference of fluid velocity at different positions on the agglomerate. When the agglomerate size is larger than Kolmogorov scale, $\Delta u_f/d_A$ can be computed as follows [22, 65]:

$$\frac{\Delta u_f}{d_A} = 1.37\varepsilon_f^{1/3} d_A^{-2/3} \ . \tag{2.2.33}$$

In contrast, if the agglomerate size is smaller than the Kolmogorov length scale, Kuster [65] proposed:

$$\frac{\Delta u_f}{d_A} = \left(\frac{2\varepsilon_f}{15\nu_f}\right)^{1/2} \ . \tag{2.2.34}$$

In the original model proposed by Kuster, the author did not propose a model for the critical breakage velocity $V_{b,c}$. It is chosen here to use a similar approach than Delichatsios & Probstein [22]:

$$V_{b,c} = \left(\frac{\sigma_{res}}{\rho_A}\right)^{1/2} \tag{2.2.35}$$

where σ_{res} is the agglomerate strength model proposed by Rumpf given by Eq. (2.2.27). ρ_A is the agglomerate density calculated by Eq (2.1.14).

As pointed out by Ammar [6], the agglomerate breakage by the turbulent stress is identified to be a predominant mechanism in a jet configuration where the expected turbulence is strong near the leakage of the conveying pipe. The turbulent stress is determined by the fluid viscosity and the local energy dissipation rate that are highly intermittent. From this physical point of view, the probabilistic approach for the agglomerate breakage seems to be more appropriate to be used with RANS modelling than the deterministic approach. Therefore, the evaluation of the breakage rate by Eq. (2.2.32) and Eq. (2.2.35) is used in the present study.

2.2.5.3 Fragment distribution function

If breakage occurs, several fragments of different sizes may be generated. Several studies have investigated this aspect by a numerical approach such as Sator et al. [96] and experimental method as Ihalainen et al. [54], but none of them has proposed a model to predict the results of the agglomerate breakage. With an experimental approach, Yeung and Pelton [128] showed that, on one hand, the breakage of large pieces is predominant for agglomerate having a low fractal dimension of 1.8. On the other hand, the attrition and detachment of primary particles from the agglomerate surface dominate in case of

fractal dimension larger than 2.4. Beside these studies, the reader can refer to some studies about the propagation of the breakage within an object as a compact sphere or an agglomerate: Mishra et al. [84], Salman et al. [94] , Herrmann et al. [47], Huang et al. [50]. However, these studies do not propose a model for the fragment distribution function. Because of the lack of information about the fragment distribution function in the literature, we consider the hypothesis hereafter.

Only binary breakage is considered. An agglomerate with $N_{pp,A}$ primary particles breaks in two fragments m and n of respectively $N_{pp,m}$ and $N_{pp,n}$ primary particles. Additionally, the number of primary particle in the resulting agglomerate follows a uniform distribution. Hence, the number of primary particles of the first fragment m is calculated as follows:

$$N_{pp,m} = \left[\left(\frac{N_{pp,min}}{N_{pp,A}} \right) + \left(1 - \frac{2N_{pp,min}}{N_{pp,A}} \right) RN \right] N_{pp,A} \tag{2.2.36}$$

To conserve the primary particle number, the number of primary particle of the second fragment n is directly deduced:

$$N_{pp,n} = N_{pp,A} - N_{pp,m} \tag{2.2.37}$$

In Eq. (2.2.36), $N_{pp,min}$ is the minimum primary particle number per agglomerate and RN is a random number between $[0, 1]$ following a uniform distribution.

2.3 Interaction between agglomerates

As shown by Figure 11, the collision of two agglomerates may lead to several scenarios:

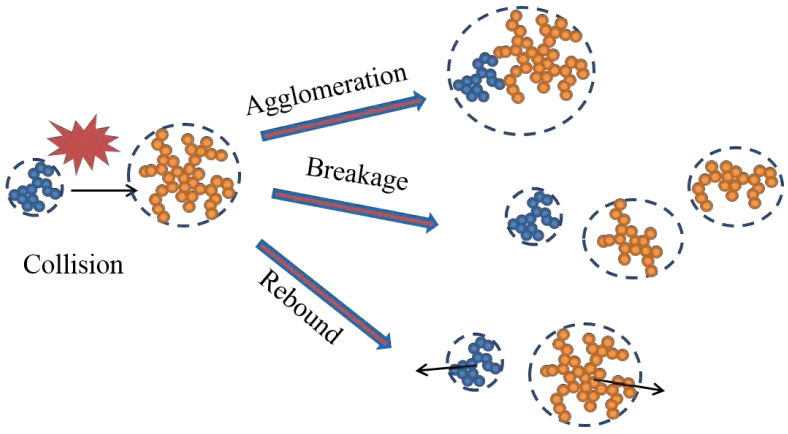

Figure 11 – Schematic representation of the collision, the agglomeration, the breakage and the rebound of agglomerates.

— Agglomeration,

— Breakage (in one or several agglomerates),
— Rebound.

Because of the complexity of those physical phenomena, it is assumed first that one collision gives only one result. Three pieces of information are required:

— Collision occurrence condition or rate.
— Collision result.
— New properties of agglomerates depending on the collision result.

The collision between two spherical particles, even with different diameters, is well understood and modeled [36]. However, this is not the case for the collision rate of agglomerates. The main difficulty is to compute the solid angle of objects characterized by fractal dimensions. That point is detailed in Chapter 3.3. Consequently, in the present section, the focus is made on the modelling of collision of spherical particles and the collision result.

2.3.1 Collision between spherical particles

In the literature, only binary collisions are usually considered [103]. The collision between more than two particles is considered as series of binary collision. In Euler-Lagrange numerical simulations, two approaches exist for the inter-particle collisions treatment: the deterministic approach and the stochastic approach. The deterministic approach computes all inter-particle distances and applies the collision rules. Such an approach is time-consuming and has not been retained in our work. Consequently, a stochastic collision algorithm has been used. In the literature, two approaches can be found: the single-particle approach [104, 88] and the multiple-particle simultaneous approach [119, 32].

In the framework of single-particle algorithm, Sommerfeld [104] proposed a collision model that has been retained in the present study. This model showed good results with less computation time than other statistical collision model. First, the particles are not treated as real particles but as numerical particles, also called parcels (each parcel representing a given number of real particles). Such an approach is equivalent to approximate the probability distribution number of particles by a Dirac sum weighted by the ratio between the real and the numerical particles [32]. For each parcel, a fictitious partner is randomly chosen in terms of velocities, size and any other properties. Following Sommerfeld [104], the fluctuating velocity components of the fictitious particle may be correlated to the fluctuating velocity components of the parcel:

$$u'_{fict,i} = R(St)u'_{p,i} + \sigma_{p,i}\sqrt{1 - R(St)^2}\xi_{gauss} \tag{2.3.1}$$

where $u'_{fict,i}$ is the fluctuating velocity component of the fictitious particle, $\sigma_{p,i}$ is the local rms velocity component i of the parcels, ξ_{gauss} is a random number following a Gaussian distribution and $R(St)$ is a correlation given in terms of the Stokes number:

$$R(St) = \exp\left(0.55St^{0,4}\right) \tag{2.3.2}$$

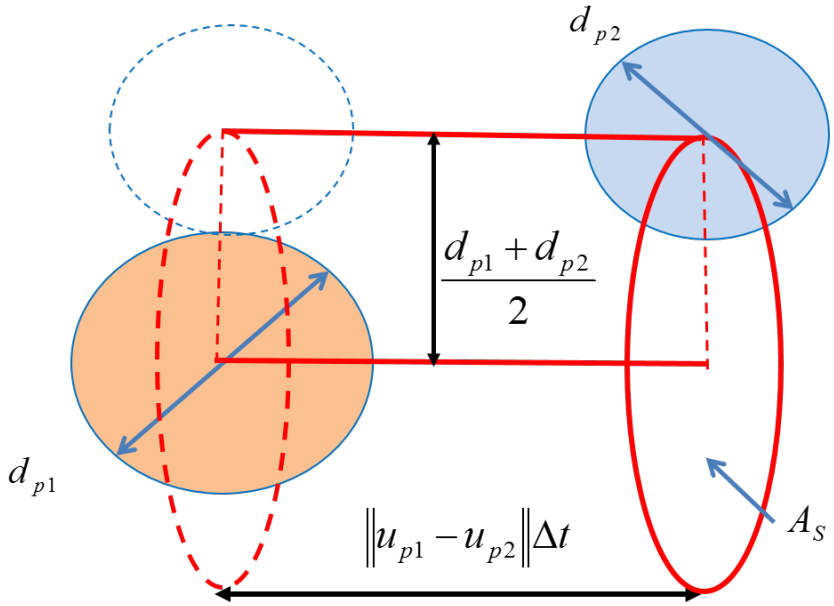

Figure 12 – Schematic representation of collision cylinder of two spherical particles

If the collision partner has uncorrelated velocities, $R(St) = 0$, and the fluctuating velocity component of the fictitious particle becomes

$$u'_{fict,i} = \sigma_{p,i}\xi_{gauss} \tag{2.3.3}$$

For determining the occurrence of the collision, the collision probability is computed as (see Figure 12):

$$P_{coll} = \frac{\pi}{4}(d_p + d_{fict})^2||\mathbf{u}_p - \mathbf{u}_{fict}||n_p\Delta t \tag{2.3.4}$$

where d_p and d_{fict} are respectively the parcel diameter and the fictitious particle diameter and n_p is the particles number density. For each collision partner, a random number RN following a uniform distribution is generated. If $RN < P_{coll}$, the collision occurs otherwise the collision does not occur [46, 56].

2.3.2 Agglomeration between spherical particles

In the literature, we may found two approaches for describing the agglomeration of particles: the Energy-based Agglomeration Model (EAM) [48] and the Momentum-based Agglomeration Model (MAM) [60]. Basically the two approaches compare the energy, or the momentum, to the one resulting from the adhesion forces. In the literature, the agglomeration between two agglomerates is still not fully described so that no model is available for non-spherical particles. For both approaches, the relative velocity of the two approaching agglomerates is compared to a critical velocity, $\mathbf{V}_{cr}$, representing the adhesive forces. If the impact velocity is smaller than such a critical velocity, agglomeration occurs otherwise two agglomerates bounce back.

Following the EAM (see Hiller [48], Alletto et al. [3], Almohammed et al. [5] for details) the critical velocity reads

$$||\mathbf{V}_{cr}|| = \frac{A}{6X_{12}^2}\frac{\sqrt{(1-e_c^2)}}{e_c^2}\sqrt{\frac{\pi d_{12}}{\bar{p}m_{12}}} \tag{2.3.5}$$

where $d_{12} = (d_{A1}d_{A2})/(d_{A1}+d_{A2})$ is the reduced diameter of both agglomerates, $m_{12} = (m_{A1}m_{A2})/(m_{A1}+m_{A2})$ the reduced mass of both agglomerates, $\bar{p}$ the maximum deformation pressure depending on material and finally e_c the normal restitution coefficient.

The MAM approach has been essentially developed by Kokinski et al. [60, 59]. Following such an approach, the critical velocity reads :

$$|\mathbf{V}_{cr}.\mathbf{k}| = \left(\frac{0.238A}{m_{12}X_{12}^2e_c}\right)^{\frac{5}{6}}\left(\frac{2m_{12}^2}{E_{12}^2}\right)^{\frac{1}{6}}d_{12}^{2/3} \tag{2.3.6}$$

where $\mathbf{k}$ is the unit vector along the center line of the two agglomerates and E_{12} the effective Young's modulus:

$$E_{12} = \left[\frac{1-\nu_{A1}^2}{E_{A1}} + \frac{1-\nu_{A2}^2}{E_{A2}}\right]^{-1} \tag{2.3.7}$$

with ν_{A1} and ν_{A2} the Poisson coefficients of the two agglomerates and E_{A1}, respectively E_{A2}, the Young's modulus of the agglomerate 1, respectively 2.

Figure 13 shows the results of the critical relative velocity by Eq. (2.3.5) for the EAM, and by Eq. (2.3.6) for the MAM. The parameters are given in Table 5.

	Property	**Value**
Parameters for both EAM and MAM	Primary particle density ρ_{pp}	2500 kg/m^3
	Primary particle diameter d_{pp}	20 nm
	Fractal dimension D_f	2.2
	Restitution coefficient e_c	0.9
	Hamaker constant A	5×10^{-19} J
	Minimal distance between particles X_{12}	4×10^{-10} m
Parameter for EAM	Maximum deformation pressure $\bar{p}$	5.0×10^9 N/m^2
Parameters for MAM	Young's modulus E_A	2.3×10^7 N/m^2
	Poisson ratio ν_A	0.28

Table 5 – Titanium dioxyde TiO_2 properties for the numerical calculation.

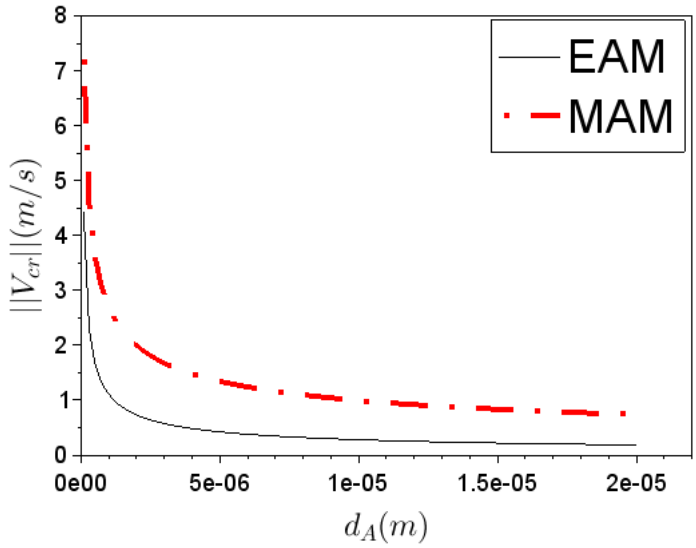

Figure 13 – Critical relative velocity in function of the agglomerate diameter for two models EAM and MAM. The agglomerates in collision have the same size.

The results show that the critical relative velocity given by both models is of same order and follows the same trend. When the size of the two agglomerates decreases, the critical relative velocity increases, i.e the agglomeration occurs more easily with smaller agglomerates. The difference between the two models is explained by the uncertain hypothesis value of the maximum deformation pressure $\bar{p}$, the Young's modulus E_A and the Poisson ratio ν_A. For more details about the comparison between two models, the reader can refer to the work of Almohammed et al., [5]. In the present study, a stochastic collision with a fictive particle is used assuming the collision angle is considered following a uniform distribution. However, the MAM model requires the computation of the angle of collision of agglomerates which is not the case for EAM model. The EAM model is therefore more suitable to be coupled with the stochastic collision method and is chosen in the present study.

As explained previously, a parcel with a statistical weight is used in the present study. In order to ensure mass and momentum conservation, the new properties of the parcel is computed by the following equations:

$$N_{pp}^{+} = N_{pp} + N_{pp,fict} \tag{2.3.8}$$

$$w_p^{+} = w_p \left(1 - \frac{N_{pp,fict}}{N_{pp,fict} + N_{pp}}\right) \tag{2.3.9}$$

$$\mathbf{u}_p^{+} = \frac{m_p \mathbf{u}_p + m_{fict} \mathbf{u}_{fict}}{m_p + m_{fict}} \tag{2.3.10}$$

where N_{pp}^{+} is the new primary particle number of the parcel. and w_p is the parcel statistical weight and w_p^+ is the new parcel statistical weight. u_p^+ is the new velocity of the parcel. The position of the parcel is assumed unchanged.

2.3.3 Agglomerate breakage by impact

In the literature, the experiments focusing on the agglomerate breakage due to collision between agglomerates is not realized yet. Although, there are many experiments that investigated the agglomerate breakage by impact with a surface [35, 54, 123]. Seipenbusch [100], later Wernet [123], used a probabilistic approach to model the breakage probability by impact. This breakage probability depends on the critical velocity of agglomerates to cause breakage and the impact velocity of agglomerate. Due to the complexity in the agglomerate strength modelling, the modelling of the critical velocity of the agglomerate breakage is still based on experimental data. By numerical method, some authors investigated on this physical phenomenon without proposing a prediction model [111, 85, 15].

Regarding the results of the agglomerate breakage by collision, several experiments and numerical calculations focused on this subject but no predictive model is proposed [84, 8, 95, 50].

Table 6 summarises few examples of the experiments in the literature investigating nanoparticle agglomerate breakage. The critical velocity of breakage $V_{c,br}$ in the experiment is defined as the minimal agglomerate velocity at impact when breakage is observed. In case of collision between two agglomerates, the $V_{c,br}$ can be assumed equal to the critical relative velocity between two agglomerates to cause the breakage. The agglomerate type and also their properties, as the agglomerate diameter, the primary particle size are very different between those experiments in the literature. For the type of agglomerates of TiO_2, a very high relative velocity between agglomerates is required to cause the agglomerate breakage.

In the present study, the agglomerate breakage by impact is not considered because of several reasons:

— An agglomerate breakage from collision occurs only in very dense regime and with a very high relative velocity between agglomerates. This physical phenomenon is competing with the agglomeration and the breakage by fluid physical phenomena which are more relevant in a jet configuration.
— This physical phenomenon is extremely complex and none of the models in the literature can predict the criterion and the results of the agglomerate breakage by collision with a quite good accuracy.

However, in case of presence of an obstacle in a jet configuration, the agglomerate breakage by impact should be considered depending on the agglomerate velocity and the agglomerate strength.

Author	Type	d_A	d_{pp}	$V_{c,br}$	Measurement
Froeschke et al.[35]	Ag, Ni, TiO_2	$\approx 20-80$ nm (Ag,Ni), $\approx$ 95nm (TiO_2)	3 - 8,3 nm (Ag), 4 nm (Ni), 12 nm (TiO_2)	$\approx$ 40 m/s - 70 m/s	TEM, CPC
Seipenbusch et al. [100]	Ni, Pt, Ag	-	6.5 - 28 nm	$\approx$ 30 m/s - 80 m/s	TEM, CPC
Ihalainen et al.[54]	TiO_2	300 nm, 400 nm	27 nm	60 m/s - 70 m/s (400 nm)	DMA, TEM
Wernet et al. [123]	Pt	24 nm	-	$\approx$ 23 m/s	MBA

Table 6 – Experiments in the literature that focus on the agglomerates or particles breakage by an impact with a surface. P_{rel} is the pressure difference to inject agglomerates, $V_{c,br}$ is the critical velocity for agglomerate breakage. CPC: Condensation Particle Counter, DMA: Differential Mobility Analyzer, TEM: Transmission Electron Microscope, MBA: Molecular Beam Apparatus.

2.3.4 Rebound of agglomerates after collision

In case of rebound, the number of primary particles in an agglomerate does not change. Because of the complex form of an agglomerate, the agglomerate velocity after the collision depends on the contact point and the agglomerate shape. In the present study, the agglomerate velocity after the collision is calculated as follows:

$$\mathbf{u}_{A1}^{+} = \mathbf{u}_{A1}^{-} + \frac{1}{2}(1+e_c)[(\mathbf{u}_{A2}^{-} - \mathbf{u}_{A1}^{-}).\mathbf{k}]\mathbf{k} \tag{2.3.11}$$

$$\mathbf{u}_{A2}^{+} = \mathbf{u}_{A2}^{-} - \frac{1}{2}(1+e_c)[(\mathbf{u}_{A2}^{-} - \mathbf{u}_{A1}^{-}).\mathbf{k}]\mathbf{k} \tag{2.3.12}$$

where $\mathbf{k}$ is the unity vector which links the center of the agglomerate 1 to the center of the agglomerate 2 at the moment of the collision.

By using the stochastic collision model of Sommerfeld [104], the collision angle is considered having a uniform distribution and the fictitious particle is stationary. By neglecting the rotation, the agglomerate velocity after a rebound is calculated as follows:

$$\mathbf{u}_{A}^{+} = \mathbf{u}_{A}^{-}\left(\frac{m_A - m_{fict}e_c}{m_A + m_{fict}}\right) \tag{2.3.13}$$

where m_{fict} is the mass of the fictitious particle, e_c is the restitution coefficient.

2.4 Other physical phenomena

2.4.1 Aggregation

The fusion of nanoparticles is one of the principal cause of the aggregation in which the total aggregate volume is smaller than the sum of the primary particles volume. The temperature condition for the nanoparticle fusion decreases abruptly compared to that of the microparticles for the same material. For example, gold fusion temperature is in order of 1340 K for gold microparticles and 1200 K for gold nanoparticles of 6 nm. The same observation is obtained for other materials as Pb, Bi, Sn [87]. In the present study, the air temperature is much lower than material fusion temperature. Therefore, the aggregation is not considered.

2.4.2 Nucleation

Nucleation is the formation of the new solid or liquid particles from the gas molecules. This phenomenon is occuring during cloud formation in nature. The classical nucleation theory supposes that the molecules and the atom form a very small particle at certain critical size. After that, those particles grown to form a new particle called *nuclei*. The nuclei size is in order of 1 - 30 nm [64]. Experimental data found that the nucleation in the atmosphere depends strongly on the presence of the molecule H_2SO_4. For an average concentration H_2SO_4 measured in the atmosphere $[H_2SO_4] \approx 10^{13}\#/m^{-3}$ [61, 31], the number concentration formation rate of the nucleus is evaluated by classical nucleation theory to be equal $C_{nucleation,max} = 10^{-5}m^3.s^{-1}$. Indeed, the nucleation is a long process over time scale of hours and days. In the present study, this physical phenomenon is not considered because we focus on the vicinity of the conveying pipe leakage with time scale of seconds or minutes.

For more information about this physical phenomenon, the reader can refer to some experimental [92, 61, 31] and numerical studies [23].

2.4.3 Condensation - Vaporization

In the atmosphere, many volatile components can condense on the nanoparticle surface. The condensation and vaporization rate depends on the particle surface property, the particle size, the condenser type and the atmospheric condition. The Kelvin effect indicates that the vaporization on a curve surface is stronger than the vaporization on a plane surface. For nanoparticles, the Kelvin effect should be considered in the condensation-vaporization process. Kulmala et al. [63] measured the growth of nanoparticles in the atmosphere by an experimental method and showed that the size evolution rate by condensation is in scale of hours or days. Again, in the present study, the time scale is seconds or minutes. Therefore, this physical phenomenon is not considered. For more information about the condensation and the vaporization process of nanoparticles in the atmosphere, the reader can refer to [34, 87].

2.4.4 Chemical reaction

For some nanoparticle types, chemical reaction between the nanoparticles and the atmospheric components can lead to strong modification of nanoparticle chemical and physical properties and often create a new nanoparticle type. For example, Kapias et al. [55] studied the transformation of $TiCl_4$ in the liquid phase to TiO_2 in the solid phase by the following reaction:

$$TiCl_4(l) + 3H_2O(l,g) \rightarrow TiO_2.H_2O.3HCl(s) + HCl(g) + \Delta H \tag{2.4.1}$$

where l, g, s indicate the liquid, gas and solid phase respectively .

The chemical reaction depends on the choice of product studied. In the present study, we choose the TiO_2 solid which, under atmospheric conditions, does not have any chemical reactions with the atmospheric component.

2.4.5 Turbophoresis

Turbophoresis is the tendency of particles to move from the higher agitation fluid region to the lower one. This physical phenomenon needs to be considered in case of the deposition of nanoparticle agglomerates, especially inside the conveying pipe. A synthesis of the theoretical works and the numerical studies (DNS) can be founded in the work of Nérisson [86]. According to Minier [82], turbophoresis is naturally modelled in the equation of the particle agitation. Therefore, the turbophoresis is modeled in the present study.

2.4.6 Thermophoresis

Thermophoresis corresponds to the movement of particle under the effect of fluid temperature gradient in the direction of the lower temperature. This physical phenomenon is involved in some industrial applications such as flow purification by collecting suspended particles in a hot flow by cold plates. More details on the thermophoresis can be found in the works of Guichard [40] and Martineau [73]. In the present study, the atmosphere near the leakage is considered having a uniform temperature, therefore thermophoresis is neglected.

2.5 Conclusion

In this chapter, we synthesized the physical phenomena related to nanoparticles in the configuration of a nanoparticle jet into the air. This synthesis allows us to evaluate the behavior of nanoparticles when they are released in the air. The understanding of the physical phenomena is essential for the development of their modelling. Each physical phenomenon is explained and their models found in the literature are presented. Because of their complexity, an estimation of their relevance in our configuration let us focus on modelling the most important physical phenomena. By simple approaches or literature data, the relevant physical phenomena considered in the present study are

the drag force on agglomerates, the agglomerates breakages by fluid turbulence and the agglomeration of agglomerates. For the physical phenomena that are less relevant and will not be modelled in the present study, we showed the configuration where those physical phenomena need further study. A physical phenomenon can be modelled by different approaches in the literature. In that case, we analyzed those approaches in order to select the most appropriate approaches.

A schematic presentation of all physical phenomena related to the nanoparticles released in the atmosphere is presented by Figure 14. In the next chapter, the validation of the modelling of selected physical phenomena will be detailed.

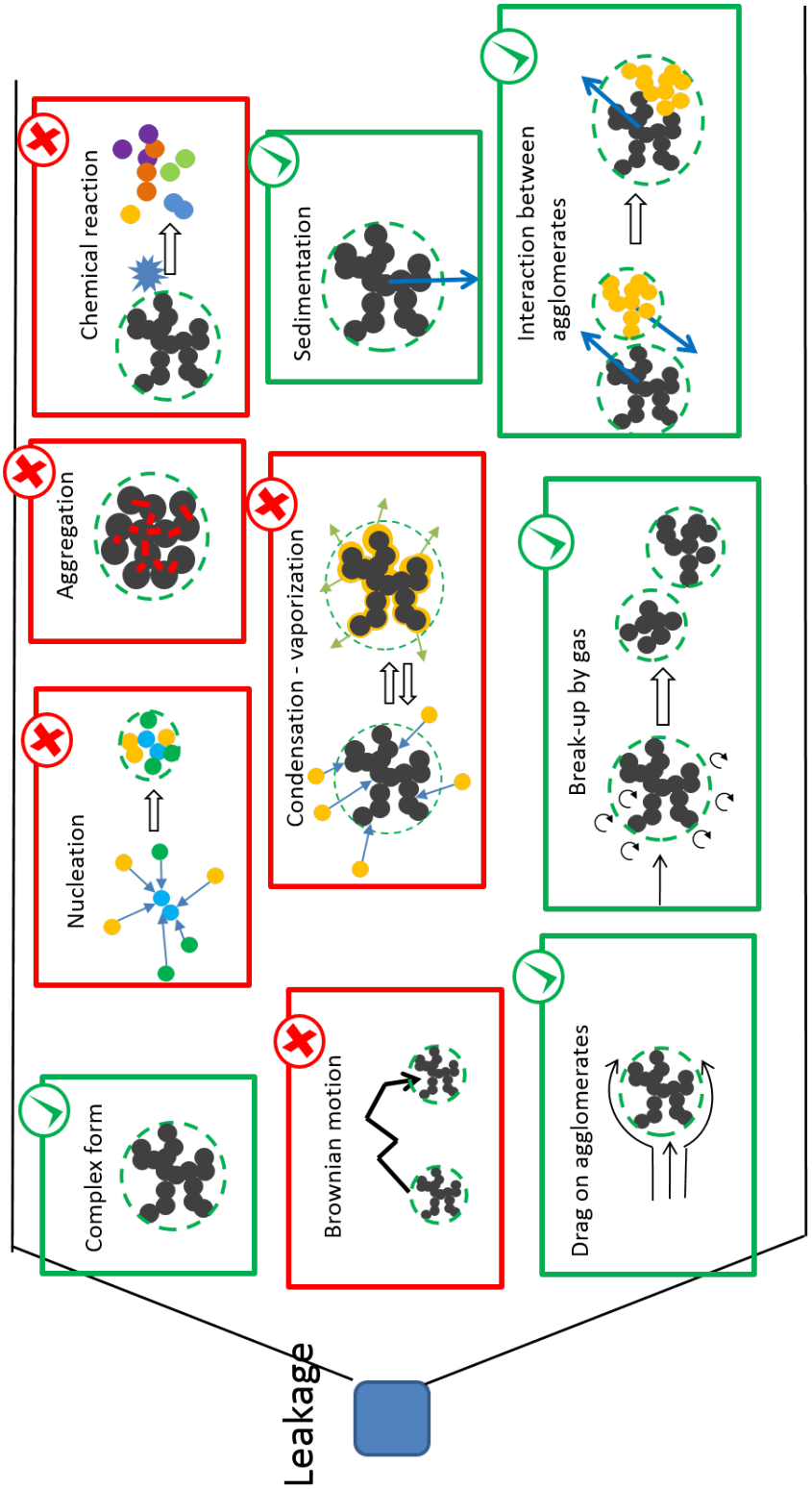

Figure 14 – Schematic representation of physical phenomena related to nanoparticles released in the air. The green box and the check symbol indicate the physical phenomena modeled in the present study. The red box and cross symbol indicate the physical phenomena not modeled in the present study.

Chapter 3

Modelling of physical phenomena related to nanoparticles

Contents

In the previous chapter, the principal physical phenomena related to nanoparticle jets are presented. In this chapter, the modelling of physical phenomena considered by CFD tool Code_Saturne v4.0.3 and by the numerical tools developed in Scilab v5.4.1 is presented. In Code_Saturne, the fluid flow is modelled by an Euler single phase approach, the fluid turbulence is modelled by RANS approach with the $k_f - \varepsilon_f$ model [69] and the agglomerate phase is modelled by a Lagrangian approach. In Scilab, the gas phase is not modelled, an homogeneous isotropic turbulence is considered and the agglomerate phase is also modelled by Lagrangian approach. The physical phenomena modelled in both numerical tools are listed below:

1. Drag force on agglomerates characterised by a fractal dimension

2. Agglomerates breakage by the fluid turbulence
3. Collision probability for agglomerates
4. Collision and agglomeration between agglomerates

3.1 Drag force on agglomerates

Considering a particle falling through a fluid, the particle velocity reaches a maximum value called "terminal settling velocity". For heavy particles, the terminal settling velocity is obtained when the gravity force is balanced by the drag force. As introduced in Chapter 2.2.3, the agglomerate size and shape modify the drag force exerted on the agglomerate and therefore change the agglomerate terminal settling velocity.

Matsumoto & Suganuma [76] investigated the terminal velocity of agglomerate in fluid for several agglomerate permeabilities. They proposed the following correlation:

$$\frac{u_{A,ts}}{u_{p,ts}} = \frac{\beta}{\beta - tanh(\beta)} + \frac{3}{2\beta^2} \tag{3.1.1}$$

where $u_{A,ts}$ is the agglomerate terminal velocity, $u_{p,ts}$ is the terminal velocity of a spherical particle of the diameter of the agglomerate and $\beta = d_A/(2\kappa)$ with d_A is the agglomerate interception diameter and κ the agglomerate permeability evaluated by Happel's model, Eq. (2.2.19). The agglomerate permeability is computed in function of the agglomerate solid fraction depending on the agglomerate fractal dimension.

A 3D domain is proposed. The height of the domain is chosen equal to 0.04 m to ensure that the agglomerate reaches a steady terminal velocity before leaving the domain. The gas and agglomerate properties are given in Table 7. Numerical simulations have been performed for several fractal dimensions (D_f =1.5, 1.8, 2.5.) and agglomerate interception diameters (d_A =200 nm, 2 μm, 10 μm, 15 μm, 20 μm).

Gas properties	Density ρ_f	1.18 kg/m^3
	Dynamic viscosity μ_f	$1.85 \times 10^{-5} Pa.s$
Agglomerate properties	Primary particle density ρ_{pp}	2500 kg/m^3
	Primary particle diameter d_{pp}	20 nm

Table 7 – Gas and agglomerate properties for the agglomerate settling velocity simulation.

The terminal setting velocities for each case are gathered in Table 8. Figure 15 shows the comparison between the results from Code_Saturne and from the analytic model given by Eq. (3.1.1).

Figure 15 shows that the numerical results from Code_Saturne are in good agreement with the analytic results. The dense agglomerate terminal settling velocity of the fractal dimension $D_f = 2.5$ tends to the spherical terminal settling velocity. When D_f is low, the fluid approaching the agglomerate is likely to move through it, the resistance experienced by the flow in passing through the agglomerate decreases. Therefore, the

d_A	Spherical case	$D_f = 2.5$	$D_f = 1.8$	$D_f = 1.5$
200 nm	2.978×10^{-6} m/s	3.036×10^{-6} m/s	4.783×10^{-6} m/s	7.742×10^{-6} m/s
2 μm	2.978×10^{-4} m/s	2.992×10^{-4} m/s	3.675×10^{-4} m/s	5.388×10^{-4} m/s
10 μm	7.417×10^{-3} m/s	7.429×10^{-3}m/s	8.285×10^{-3} m/s	1.1×10^{-2} m/s
15 μm	1.661×10^{-2} m/s	1.663×10^{-2}m/s	1.824×10^{-2} m/s	2.363×10^{-2} m/s
20 μm	2.932×10^{-2} m/s	2.995×10^{-2} m/s	3.123×10^{-2} m/s	4.060×10^{-2} m/s

Table 8 – Terminal settling velocities of spherical particles and agglomerates for several sizes and fractal dimensions.

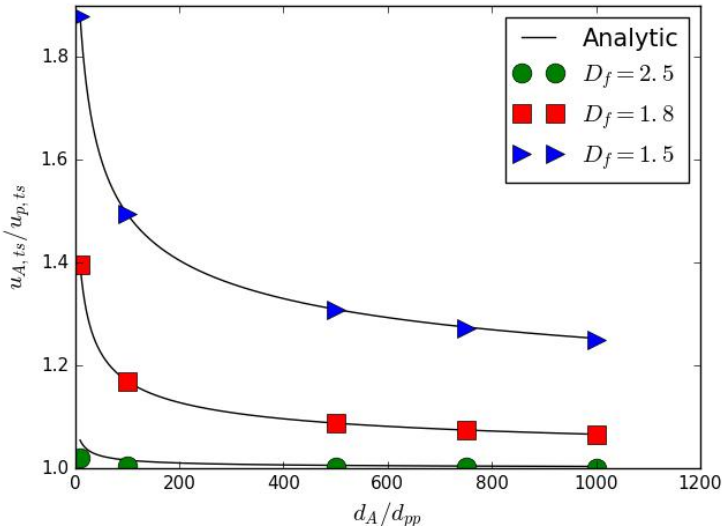

Figure 15 – Agglomerate terminal settling velocity normalized by the spherical particle terminal settling velocity with respect to the agglomerate interception diameter normalized by the primary particle diameter for different agglomerate fractal dimensions. $u_{A,ts}$ and $u_{p,ts}$ are the terminal settling velocities of agglomerates and spherical particles respectively. The solid lines correspond to Eq. (3.1.1). The symbols correspond to the results from Code_Saturne.

drag on agglomerate decreases and the terminal settling velocity increases. This trend is also observed in the experiments of Li & Logan [70]. The agglomerate drag model is therefore correctly implemented in Code_Saturne.

3.2 Agglomerate breakage by the fluid turbulence

This section presents in detail the model implemented in Code_Saturne for the agglomerate breakage. The model has been first developed in case of homogeneous isotropic configuration (later called 0D configuration) and then implemented in Code_Saturne. To

ensure a correct implementation in the CFD code, a systematic comparison between the results obtained by the two numerical tools is performed.

3.2.1 Agglomerates of nanoparticles in homogeneous isotropic turbulence

The domain is a cube of length $l_{cube} = 0.01\ m$. In this specific test the positions and velocities of the agglomerate are not computed. A constant fluid shear rate $\gamma_f = \sqrt{(\varepsilon_f/\nu_f)}$ is considered. For each time step, the probability of the agglomerate breakage is calculated as a function of the breakage frequency of Eq. (2.2.32). If the breakage occurs, the agglomerate fragment properties are calculated by Eqs. (2.2.36) and (2.2.37). The agglomerate median count diameter d_{50} is determined as the diameter yielding half of agglomerates in the system larger than d_{50} and another half of agglomerates smaller.

Figures 16 and 17 show the time-evolution of the agglomerate total number and the agglomerate median count diameter respectively for the case of the agglomerate initial size of $d_A = 100\ \mu m$, the fractal dimension of $D_f = 1.6$ and a shear rate of $\gamma_f = 10^5\ s^{-1}$ as an example. Because of the breakage, the agglomerate median count diameter decreases and the agglomeration number increases. A stable agglomerate median count diameter is obtained because when the agglomerate size decreases, the agglomerate strength increases and the turbulence is not strong enough to break the agglomerates. This trend is well reproduced.

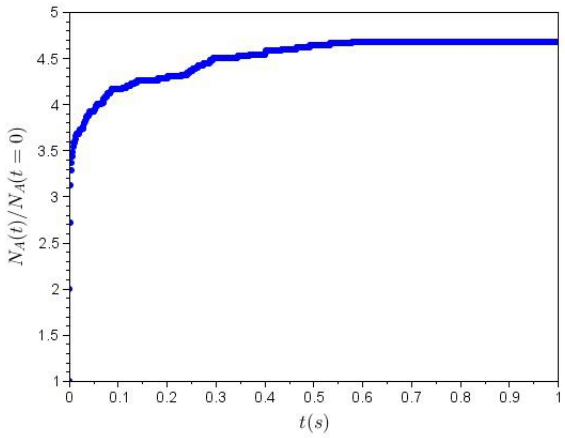

Figure 16 – Time-evolution of the agglomerates number. The initial agglomerate diameter is $d_A = 100\ \mu m$, the agglomerate fractal dimension $D_f = 1.6$ and shear rate $\gamma_f = 10^5\ s^{-1}$.

As explained in Chapter 2.2.5, the relevant parameters in agglomerate breakage are the agglomerate strength and the fluid dissipation. Therefore, those two parameters have been tested. The initial agglomerate diameter is $d_A = 100\ \mu m$ and the primary

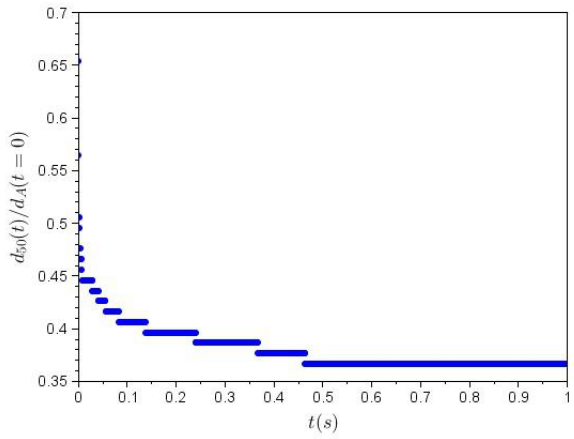

Figure 17 – Time-evolution of agglomerate median count diameter. The initial agglomerate diameter $d_A = 100\ \mu m$, the agglomerate fractal dimension $D_f = 1.6$ and the shear rate $\gamma_f = 10^5\ s^{-1}$.

particle diameter $d_{pp} = 20\ nm$. Two values of the fractal dimension $D_f = 1.6, 2.3$ are tested. Figure 18 shows the results from Code_Saturne, from 0D configuration and a

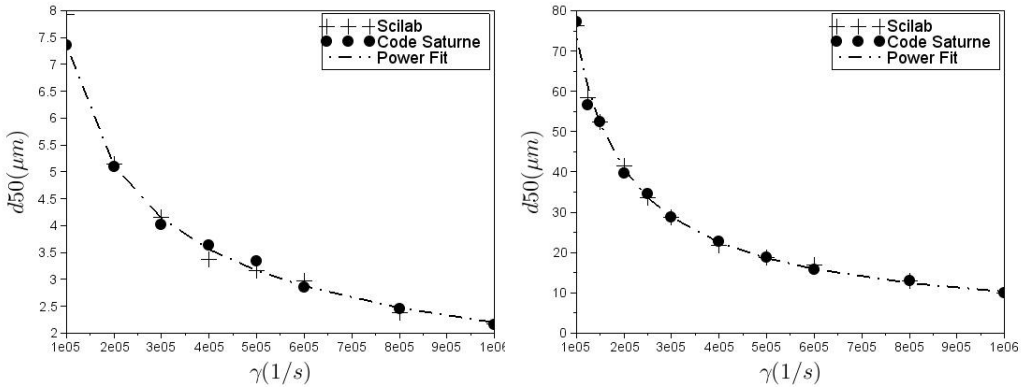

Figure 18 – The agglomerate median count diameter with respect to the turbulent shear rate for the agglomerate fractal dimension $D_f = 1.6$ (left) and for the agglomerate fractal dimension $D_f = 2.3$ (right). The power fit stands for Eqs. (3.2.1) & (3.2.2).

power fit,

$$d_{50} = 3.116 \times 10^4 \gamma_f^{-0.525} \quad \text{for} \quad D_f = 1.6 \tag{3.2.1}$$

$$d_{50} = 1.367 \times 10^6 \gamma_f^{-0.854} \quad \text{for} \quad D_f = 2.3 \tag{3.2.2}$$

Figure 18 shows that the results from Code_Saturne are in good agreement with the

results from 0D configuration. The agglomerate count median diameter decreases when the flow stress increases. The agglomerate count median diameter increases when the fractal dimension increases because the agglomerate strength increases. Those trends are well reproduced. The results from the model used in the present study show a correlation between the particle count median diameter and the turbulent shear rate, as demonstrated by the experiment of Ammar et al., [6].

3.2.2 Nanoparticle jet simulation

The objective of this section is to study the agglomerates breakage in a turbulent jet. In Chapter 4, a numerical simulation of an accidental pipe leakage, inspired by the accidental pipe leakage in Blanzy, will be realized but the numerical domain will be much larger and the detailed physical phenomena near the jet needs to be tested. In this section, a numerical simulation near the jet is realized taking into account the agglomerate breakage.

A domain is generated with the dimensions of 0.47 m × 0.47 m × 1.0 m. Figure 19 shows the boundary conditions of the simulation. The injection nozzle is located on the top of the domain. The nozzle diameter is $D_{nozzle} = 14\ mm$. The lateral faces are set as "wall" boundary conditions and the bottom face is set as "Outlet".

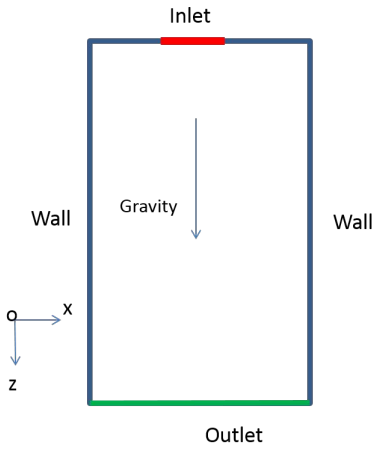

Figure 19 – Boundary conditions in the numerical simulation of the agglomerate breakage

Figure 20 shows the 3D mesh composed of 36180 cells and a zoom on the Inlet.

The physical properties of the fluid and the agglomerates are given in Table 9. The Reynolds number based on nozzle diameter is $Re = D_{nozzle}U_f/\nu_f \approx 10,000$. The maximum value of the fluid velocity and the agglomerates velocity at the nozzle are both equal to $U_f = U_A = 11\ m/s$ and the velocity profile follows a parabolic shape. We tested to inject the agglomerate diameter of $d_A = 100\ nm$ with the fractal dimension of $D_f = 2.5$ which are the data for the simulation of conveying pipe leakage in Blanzy but the agglomerate breakage was not observed. Therefore, the agglomerate diameter of

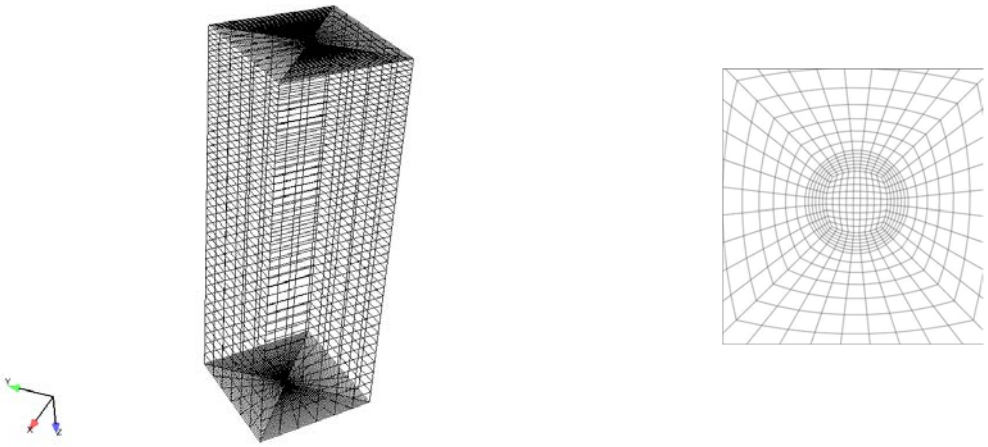

Figure 20 – Mesh used in numerical simulation (left) and zoom on the inlet face (right).

$d_A = 100\ \mu m$ with the fractal dimension of $D_f = 1.8$ is chosen in the present simulation.

The turbulence model for the fluid phase is the standard $k_f - \varepsilon_f$ (without turbulence modulation by the agglomerates). For the agglomerate phase, 100 parcels of statistical weight of 1 are injected every 0.001 s. The statistical weight of the parcels is not an important parameter in this simulation case because the breakage by fluid turbulence is independent of the total number concentration of agglomerates.

Gas properties	Density ρ_f	1.18 kg/m^3
	Dynamic viscosity μ_f	1.85×10^{-5} $Pa.s$
Agglomerate properties	Primary particle density ρ_{pp}	2500 kg/m^3
	Primary particle diameter d_{pp}	20 nm
	Agglomerate fractal dimension D_f	1.8
	Agglomerate interception diameter d_A	100 μm

Table 9 – Fluid and agglomerates physical properties

The influence of agglomerates on the fluid phase and the agglomerates collision are not taken into account. The simulation is performed in two steps:

— First, the gas phase is computed without the agglomerates:

— After that, the trajectories of agglomerates are computed from the steady fluid flow.

Figure 21 shows the fluid velocity and dissipation fields at the beginning of the Lagrangian simulation. The fluid velocity is steady after 2 seconds of simulation

Figure 22 shows time-evolution of the total agglomerate number in the domain. After 1.5 s of physical simulation time, the total number of agglomerates in the domain is constant. The agglomerate phase simulation is therefore steady after 1.5 s. The time-average calculation of the agglomerate parameters results is performed between 2 s and

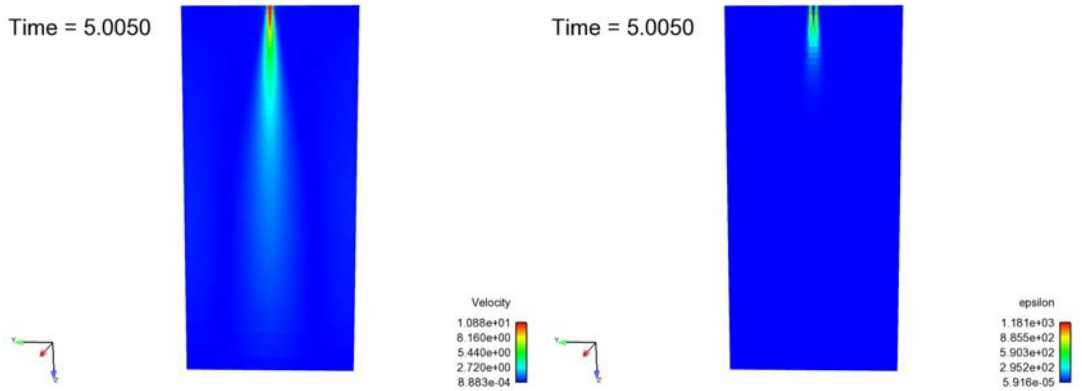

Figure 21 – Fluid velocity field (left) and fluid dissipation (right) at the beginning of the Lagrangian simulation.

3 s of the simulation.

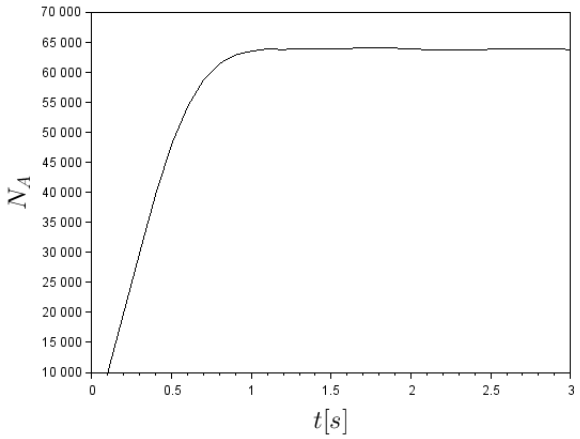

Figure 22 – Time-evolution of the total agglomerate number in the domain.

Figure 23 shows the steady dispersion of agglomerates. Most of large agglomerates of $d_A = 100\ \mu m$ did not break. A few small agglomerates of $d_A = 100\ nm$ are generated after the breakage. The fluid turbulence may not be strong enough to break agglomerates and because of the particle dispersion, agglomerates may not pass through the strongest turbulence field near the jet.

Figure 24 shows the frequency of the PDF of all agglomerates in the domain. The limit of the agglomerate size distribution are $d_{A,min} = 100\ nm$ and $d_{A,max} = 100\ \mu m$. The breakage is observed but the number of large agglomerates $d_A = 100\ \mu m$ is still high, approximately 84.2 %. The smallest agglomerates of $d_A = 100\ nm$ are generated by the breakage, around 1 % of the total agglomerate number.

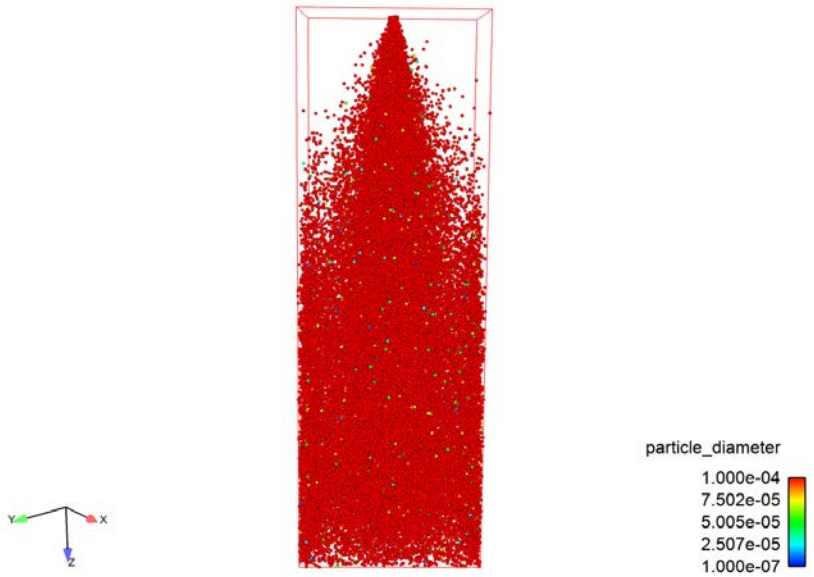

Figure 23 – Dispersion of agglomerates phase. The parcels are colorized by their diameter

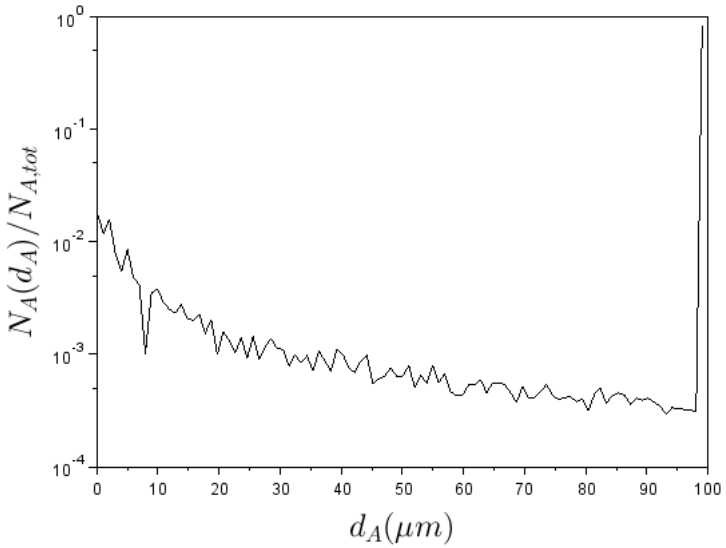

Figure 24 – Frequency of the agglomerate diameter distribution within the domain

Figure 25 compares the frequency of the PDF of the agglomerates phase at different distances from the nozzle. The results show that the breakage occurred already very near the nozzle. The breakage occurred between between the nozzle and $5 \times D_{nozzle}$. Further than $5 \times D_{nozzle}$, the agglomerate size distribution does not change which indicates that

the breakage is not predominant anymore. This trend is expected because near the orifice, the jet turbulence is strong enough to break the agglomerate. Downstream, the jet turbulence decreases and the breakage decreases.

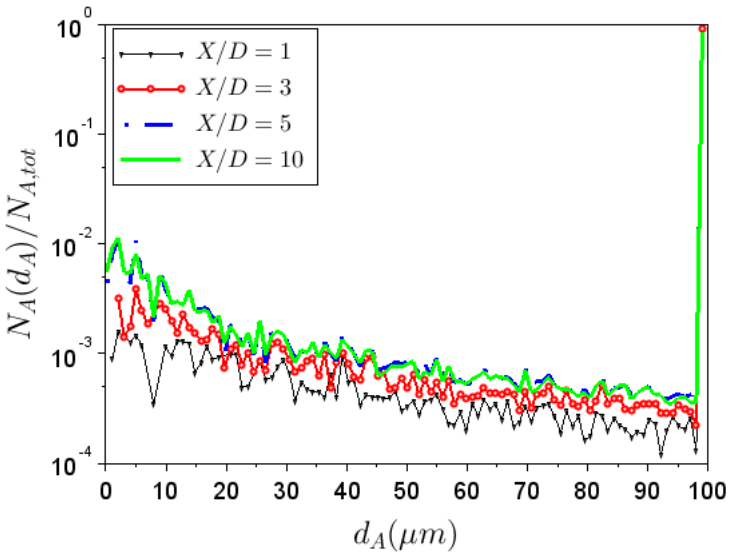

Figure 25 – Frequency of the agglomerate size distribution function for different distance from the nozzle. X stands for the distances from the nozzle and D stands for the nozzle diameter $D_{nozzle} = 14\ mm$.

3.3 Collision probability for agglomerates

Modeling the collision between agglomerates is challenging because of the complex shape of agglomerates and the local modification of the flow by agglomerates. In the literature, inter-agglomerate collision are usually performed by considering the agglomerate as a sphere with an equivalent diameter [12]. In order to avoid such an approximation, some studies perform Discret Element Method (DEM) to simulate the collision between agglomerates and spherical particles [39] and to simulate the collision between agglomerates [112]. Even if those numerical simulations are very useful to understand the local mechanisms of the collision, they are still computationally expensive and cannot be used for practical applications. The Euler n-fluid multiphase approach [102] and the Euler - Lagrangian multiphase approach are more suitable for industrial applications. These approaches are less time consuming but cannot take into account the complex structure of the agglomerates. In this context, a new simple collision model taking into account the structure of the agglomerate has been developed.

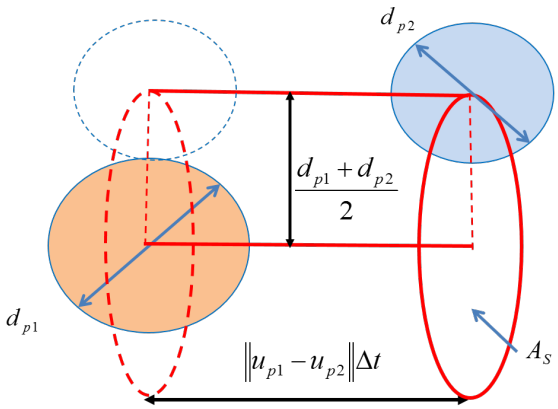

Figure 26 – Collision cylinder for two spherical particles.

3.3.1 Model description

Basically, the probability of the collision between two spherical particles reads

$$P_{coll,s} = A_S(d_{p1}, d_{p2})||\mathbf{u}_{p1} - \mathbf{u}_{p2}||n_p\Delta t \tag{3.3.1}$$

where $\mathbf{u}_{p1}$ and $\mathbf{u}_{p2}$ are the translational velocity of the two particles, n_p is the number density of particles and A_S is the cross section of the collision cylinder the collision cross section. For two spherical particles of diameter d_{p1} and d_{p2}, the collision cross section is directly given by

$$A_S(d_{p1}, d_{p2}) = \frac{\pi}{4}(d_{p1} + d_{p2})^2. \tag{3.3.2}$$

The collision cylinder for two spherical particles is shown by Figure 26.

As shown by Figure 27, if one particle or both particles are agglomerates, they can pass through each other without experiencing a collision because of the agglomerate porosity even if they are inside the collision cylinder. Therefore, the probability of the collision given by Eq. (3.3.1) is no longer valid. Similarly to the collision probability for spherical particles, the collision probability for agglomerates is proposed as

$$P_A = A_A||\mathbf{u}_{A1} - \mathbf{u}_{A2}||n_A\Delta t \tag{3.3.3}$$

where $\mathbf{u}_{A1}$ and $\mathbf{u}_{A2}$ are the translational velocity of the two agglomerates.

In Eq. (3.3.3), the collision cross section, A_A, for an agglomerate is different from the collision cross section $A_s(d_{p1}, d_{p2})$ (Eq. (3.3.2)) for the spherical particles. This collision cross section A_A is unknown and is a function of the geometrical properties of the agglomerate (number of primary particles forming the agglomerate, geometry and microstructure of the agglomerate). Due to the anisotropic geometry of the agglomerate, the agglomerate collision cross section varies with respect to the collision angle between the agglomerate and the incident spherical particle or agglomerate. In our study, we define the collision cross section of the agglomerate, A_A, as the mean of the collision

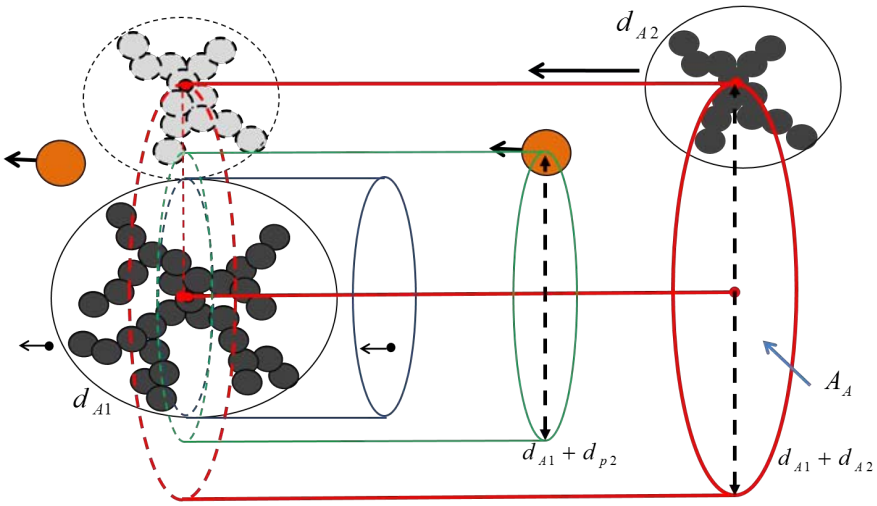

Figure 27 – Schematic description of the collision between an agglomerate and a spherical particle or the collision between two agglomerates.

cross section over all the collision angles. In order to model A_A, a collision probability coefficient, R_A, is defined as follows

$$R_A = \frac{A_A}{A_S(d_{A1}, d_{A2})} \tag{3.3.4}$$

where $A_S(d_{A1}, d_{A2})$ is calculated as:

$$A_S(d_{A1}, d_{A2}) = \frac{\pi}{4}(d_{A1} + d_{A2})^2 \tag{3.3.5}$$

with d_{A1} is the interception diameter of agglomerate 1 which corresponds to the maximum extension distance of the agglomerate from its mass center. d_{A2} is the interception diameter of agglomerate 2.

3 configurations were considered in our study:

1. Collision between an agglomerate and a tracer particle: $d_{A2} \to 0$.
2. Collision between an agglomerate and a spherical particle: $d_{A2} \equiv d_{p2}$.
3. Collision between two agglomerates.

The following section presents different models to calculate the collision probability coefficient R_A for those configurations.

3.3.1.1 Collision between an agglomerate and a tracer particle

In case of collision between an agglomerate and a tracer particle, the collision probability coefficient R_A represents the ratio between the agglomerate cross section compared

to the surface of a disk of diameter d_{A1}. Following [89], the agglomerate cross section A_{c-s} can be estimated as follows

$$A_{c-s} = \frac{\pi}{4}\xi N_{pp}^{\alpha} d_{pp}^2 \tag{3.3.6}$$

where N_{pp} is the number of primary particles in the agglomerate, d_{pp} is the primary particle diameter. ξ and α are the parameters which represent the agglomerate projected cross section geometry and are calculated from the numerical simulations. By definition, the collision probability coefficient R_A is calculated in this case as follows

$$R_A = \xi N_{pp}^{\alpha} \frac{d_{pp}^2}{d_{A1}^2} \tag{3.3.7}$$

where d_{A1} is the agglomerate interception diameter.

3.3.1.2 Collision between an agglomerate and a spherical particle

In case of the collision between an agglomerate and a spherical particle, the collision probability coefficient R_A is the ratio between the collision cross section and the surface of the disk of diameter $(d_{A1} + d_{p2})$. From a statistical point of view, we represent the agglomerate mean cross section by the cross section of a spherical particle of the diameter d'_{p1}. This consideration gives $A'_{p1} = A_{c-s,A1}$. Therefore, the collision cross section of the agglomerate (d_{A1}) and spherical particle (d_{p2}) is expected to be equal to the collision cross section of the spherical particle (d'_{p1}) and the spherical particle (d_{p2}). This idea is presented by Figure 28.

By considering $A'_{p1} = A_{c-s,A1}$, from Eq. (3.3.6), the diameter of the equivalent spherical particle considered is calculated as

$$\left(d'_{p1}\right)^2 = d_{pp}^2 \xi N_{pp}^{\alpha} \tag{3.3.8}$$

Finally, the collision probability coefficient for agglomerate and spherical particle is proposed as

$$R_A = \frac{\left(d_{pp,A1}\sqrt{\xi_{A1} N_{pp,A1}^{\alpha_{A1}}} + d_{p2}\right)^2}{(d_{A1} + d_{p2})^2} \tag{3.3.9}$$

where the coefficients ξ_{A1} and α_{A1} are the same as ξ and α in the calculation of the agglomerate cross section (Eq. (3.3.6)).

3.3.1.3 Collision between two agglomerates

In case of the collision between two agglomerates, the collision probability coefficient R_A is the ratio between the collision cross section of the two agglomerates compared to the surface of the disk of the diameter $(d_{A1} + d_{A2})$. Similarly to the case of the collision between an agglomerate and a spherical particle, we consider two spherical particles which have the same mean cross section of two agglomerates respectively. Therefore,

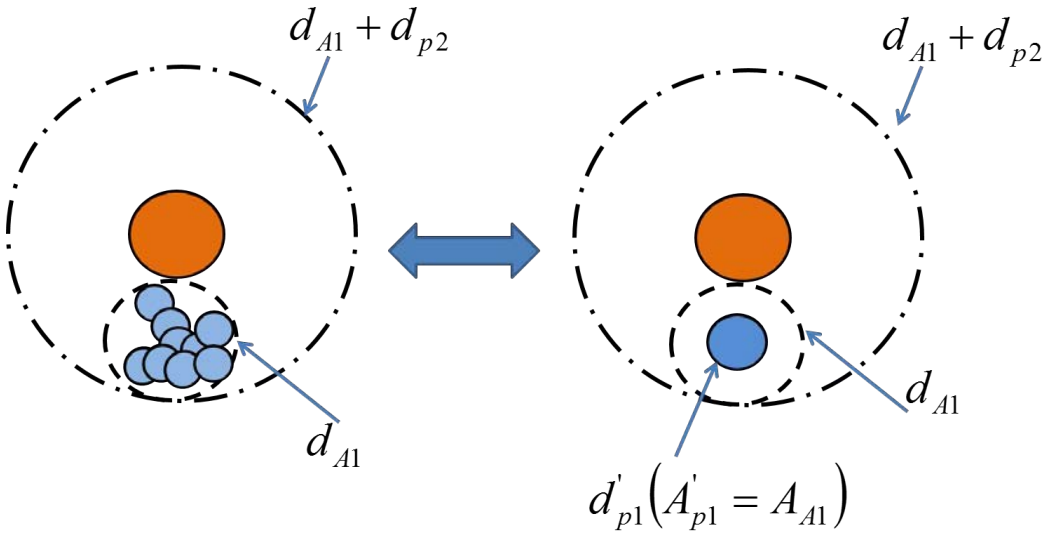

Figure 28 – Schematic description of the collision between an agglomerate and a spherical particle. The collision probability between an agglomerate with diameter d_{A1} and a spherical particle with diameter d_{p2} is considered equal to the collision probability between a spherical particle which has the same mean cross section of the agglomerate of diameter d'_{p1} and a spherical particle of diameter d_{p2}.

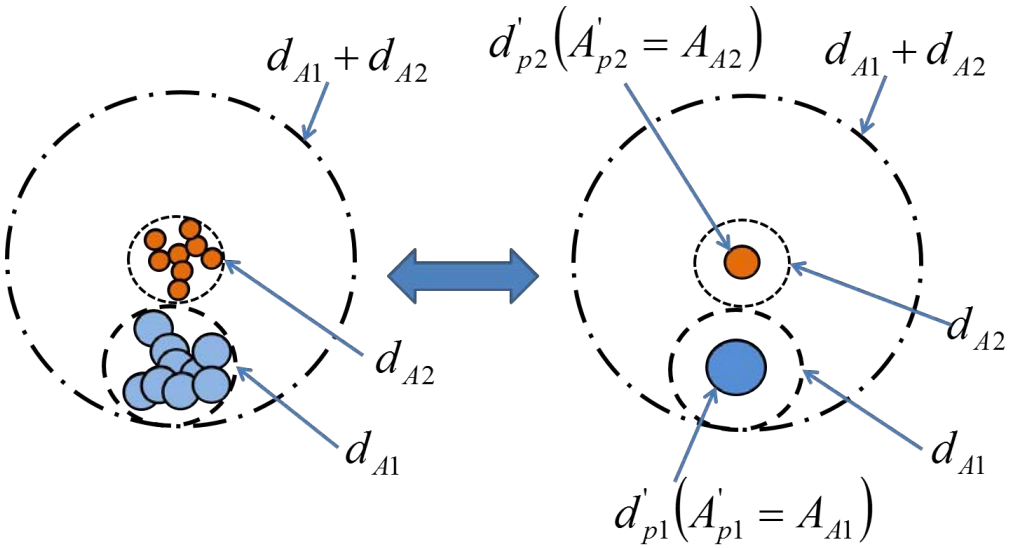

Figure 29 – Schematic description of the collision between two agglomerates. Two spherical particles which have the same mean cross section of two agglomerates is considered respectively.

the collision cross section of the agglomerate of diameter d_{A1} and the agglomerate of diameter d_{A2} is equal to the collision cross section of the spherical particle (d'_{p1}) and the spherical particle (d'_{p2}). This idea is presented by Figure 29.

Based on the assumption presented above, the collision probability coefficient for two agglomerates is written as:

$$R_A = \frac{\left(d_{pp,A1}\sqrt{\xi_{A1}N_{pp,A1}^{\alpha_{A1}}} + d_{pp,A2}\sqrt{\xi_{A2}N_{pp,A2}^{\alpha_{A2}}}\right)^2}{(d_{A1}+d_{A2})^2} \tag{3.3.10}$$

where $d_{pp,A1}$ and $d_{pp,A2}$ are the primary particle diameters of agglomerate 1 and 2 respectively. d_{A1} and d_{A2} are the diameters of agglomerate 1 and 2 respectively. $N_{pp,A1}$ and $N_{pp,A2}$ are the numbers of primary particles of agglomerate 1 and 2 respectively. ξ_{A1}, α_{A1} and ξ_{A2}, α_{A2} are parameters of the collision cross section of the agglomerate 1 and 2 respectively. The following section is dedicated to the determination of the collision probability coefficient R_A by means of numerical simulations.

3.3.2 Numerical simulations

To measure accurately the collision probability coefficient, R_A, deterministic simulations of the collision between an agglomerate and a spherical particle, and between two agglomerates, have been performed. For such numerical simulations, the first step consists in the generation of the agglomerate structure [127, 26, 29]. In the present study, the agglomerates are made of a collection of monosized primary particles.

3.3.2.1 Random structure of agglomerates

A random structure of agglomerates is generated according to a given interception diameter d_A and a given maximum coordination number that represents the maximum number of contacts allowed between primary particles composing the agglomerate. A maximum coordination number of 2 means that the primary particles of the agglomerate cannot have more than 2 contacts with other primary particles. If the coordination number gives information on the local structure of the agglomerate (i.e. at the scale of primary particles), the global characterization, in terms of geometry, of the agglomerate (i.e. at the scale of the agglomerate) is commonly related to the fractal dimension D_f. In our method of generating a random agglomerate structure, the input parameters are the agglomerate diameter d_A, the primary particle diameter d_{pp} and the maximum coordination number. The fractal dimension of the agglomerate is obtained consequently. The method is composed of the following steps :

1. Start from given primary particle which is the reference.
2. For each primary particle already forming the agglomerate, insert new primary particles in contact. This is done only for the primary particles having coordination number smaller or equal to the maximum coordination number. The position

of the new primary particles are calculated as follows

$$\begin{aligned} x_{pp,new} &= x_{pp} + d_{pp}\sin(\phi)\cos(\theta) \\ y_{pp,new} &= y_{pp} + d_{pp}\sin(\phi)\sin(\theta) \\ z_{pp,new} &= z_{pp} + d_{pp}\cos(\phi) \end{aligned}$$

where d_{pp} is the primary particle diameter, ϕ and θ are two random angles ranging $\theta \in [0; 2\pi]$ and $\phi \in [0; \pi]$.

3. Check for overlapping with every primary particles of the agglomerate. If the new primary particle overlaps another primary particles of the structure, the new primary particle is rejected.
4. Check the interception diameter of the agglomerate. While the chosen interception diameter is not reached, the algorithm goes back to step 2 and a new primary particle is added to the structure.
5. When the generation of primary particles stops, the exact agglomerate interception diameter and the agglomerate fractal dimension are calculated.

The draw of primary particles stops when the interception diameter of the agglomerate is larger than the predefined interception diameter . Therefore, the interception diameter of the agglomerate is not strictly equal to the interception diameter initially defined. When the generation of the agglomerate is stopped, the interception diameter of the agglomerate is finally measured by

$$d_A = 2\max\left(\sqrt{(x_{pp,i} - x_A)^2 + (y_{pp,i} - y_A)^2 + (z_{pp,i} - z_A)^2} + \frac{d_{pp}}{2}\right) \tag{3.3.11}$$

where $(x_{pp,i}, y_{pp,i}, z_{pp,i})$ indicates the mass center of the primary particle i in the agglomerate, (x_A, y_A, z_A) indicates the agglomerate mass center.

In the simulation, when several agglomerates are generated, the mean agglomerate interception diameter is calculated

$$\overline{d_A} = \frac{\sum_i^{N_A} d_A}{N_A} \tag{3.3.12}$$

where N_A is the number of agglomerates generated.

The fractal dimension of the agglomerate is calculated by the *Box Counting Method* [74]. Two examples of generated agglomerates are shown by Figure 30.

As expected when increasing the coordination number the agglomerate is more dense because the number of local contacts is higher. The distribution function of the fractal dimension for 100 agglomerates generated for four agglomerate sizes $\overline{d_A} = 110, 211, 411, 611$ nm with $d_{pp} = 20$ nm is presented by Figure 31. Within those 100 agglomerates of each agglomerate size, 50 agglomerates have the maximum coordination number of 2 and the other 50 agglomerates have the maximum coordination number of 3.

Figure 31 shows that the fractal dimension is ranging between $1.8 < D_f < 2.4$ for agglomerate mean size of $\overline{d_A} = 411nm$ and $\overline{d_A} = 611nm$. This range of the fractal

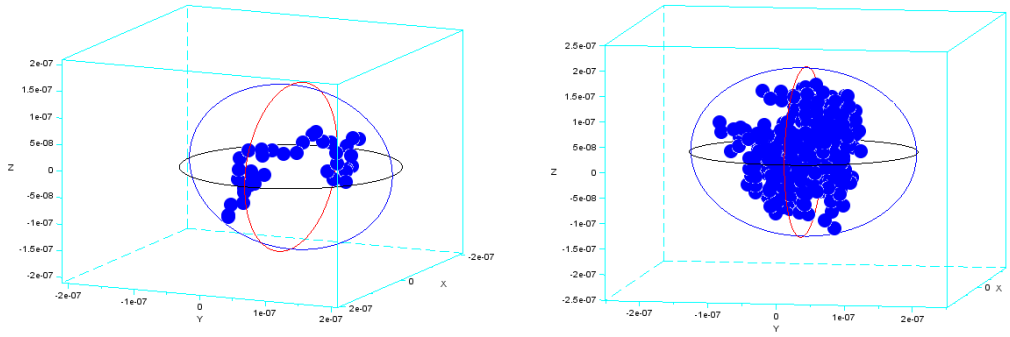

Figure 30 – Examples of two agglomerates generated for the study. In both cases, the interception diameter is 300 nm and the diameter of primary particles is 20 nm. The circles indicate the interception diameter of the agglomerate. Left: the fractal dimension is $D_f = 1.95$ for a coordination number of 2 and right: the fractal dimension is $D_f = 2.23$ for a coordination number of 3.

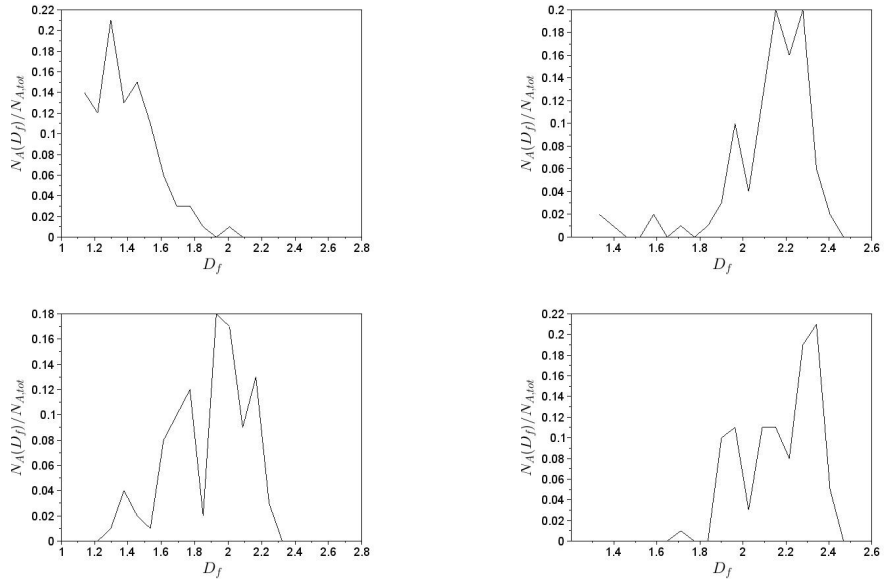

Figure 31 – Probability distribution function of the fractal dimension for 100 agglomerates generated. $N_{A,tot} = 100$. (a)$\overline{d_A} = 110$ nm, (b)$\overline{d_A} = 211$ nm, (c) $\overline{d_A} = 411$ nm, (d)$\overline{d_A} = 611$ nm

dimension can be observed in fumed silica agglomerates ([51]). The fractal dimension distribution is lower, between $1.2 < D_f < 2.2$, for agglomerate mean size of $\overline{d_A} = 110nm$ and $\overline{d_A} = 211nm$. This range of the fractal dimension can be observed in ethylene flame

soot ([16]).

3.3.2.2 Numerical method to characterize the collision cross section

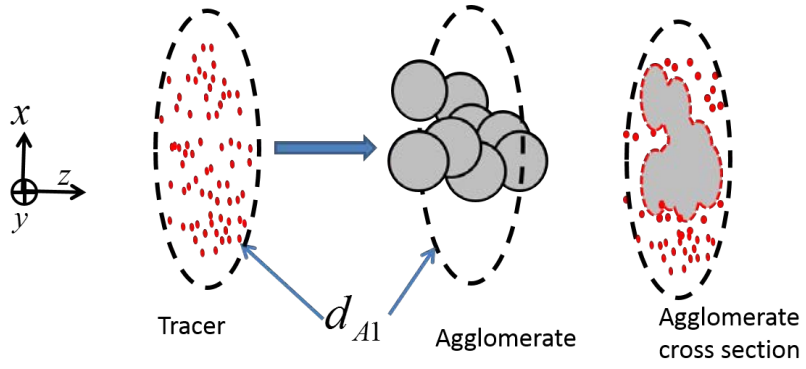

Figure 32 – Schematic description of the numerical simulation for determining collisional cross section of an agglomerate.

The collision cross section is equal to the agglomerate cross section when tracer particles are projected onto the agglomerate as shown by Figure 32. The collision of the tracers with the agglomerate is deterministically detected. The ratio of the number of tracers hitting the agglomerate over the total number of projected tracers is equal to the ratio of the cross section of agglomerate over the surface of the disk having the interception diameter. It leads to

$$R_A = \frac{A_{c-s}}{A_{inj}} \approx \frac{N_{coll}}{N_{inj}} \tag{3.3.13}$$

where A_{c-s} is the agglomerate cross section, A_{inj} the injection surface of tracers, N_{coll} is the number of tracers collided with the agglomerate, N_{inj} the number of tracers injected. It must be emphasized that such a surface has to be at least larger than the object. In the present case, 1000 tracers are injected with position randomly distributed in a disk. Numerical simulations with 10,000 tracers have shown no improvements of the results.

Due to the anisotropic geometry of the agglomerate, the agglomerate collision cross section varies with respect to the relative rotation between the agglomerate and the incident spherical particle or agglomerate. Therefore, for each agglomerate, the collision probability coefficient R_A is the average value of all the rotations of the agglomerate. Each agglomerate is rotated every $\pi/4$ radians between $[0, \pi]$ around three axes Ox, Oy and Oz passing through the agglomerate center. Numerical simulations of the rotation every $\pi/8$ radians have shown no improvements of the results.

To compute the collision probability coefficient between an agglomerate and a spherical particle, the tracers are replaced by a spherical particle of the predefined diameter

d_{p2}. In this case, the numerical value of R_A is calculated as follows:

$$R_A = \frac{A_A}{A_{inj}} \approx \frac{N_{p2,coll}}{N_{inj}} \tag{3.3.14}$$

where A_A is the agglomerate collision cross section, $A_{inj} = (\pi/4)(d_A + d_{p2})^2$ is the injection surface. $N_{p2,coll}$ is the number of spherical particles collided with the agglomerate and N_{inj} is the number of spherical particles injected.

The numerical method for collision between an agglomerate and a spherical particle is composed of the following steps:

1. Generate randomly the structure of the agglomerate 1 with a predefined diameter.
2. Generate randomly the position of the spherical particle 2 in the disk of diameter $d_{A1} + d_{p2}$. The center of this disk is equal to the mass center of the agglomerate 1.
3. For each position of the spherical particle 2, detect the collision by comparing the distance between the spherical particle and each primary particle of the agglomerate 1.
4. Calculate R_A, rotate the agglomerate 1, go to step 2. When R_A is calculated for all the rotations, go to the next step.
5. Calculate the average value R_A over all the rotation angles.

The numerical method for collision between two agglomerates is similar to the method for the collision between an agglomerate and a spherical particle:

1. Generate randomly the structure of the agglomerate 1 with a predefined diameter.
2. Generate randomly the structure of the agglomerate 2 with a predefined diameter.
3. Generate randomly the position of the mass center of the agglomerate 2 in the disk of the diameter of $d_{A1} + d_{A2}$. The center of this disk is equal to the mass center of the agglomerate 1.
4. For each position of the agglomerate 2, detect the collision by comparing the distance between each primary particle of the agglomerate 2 and each primary particle of the agglomerate 1.
5. Calculate R_A, rotate the agglomerate 1, go to step 3. When R_A is calculated for all the rotations of the agglomerate 1, go to next step.
6. Calculate the average value R_A over all the rotation angles.

3.3.3 Results and discussion

3.3.3.1 Collision between an agglomerate and a tracer particle

In order to determine the coefficients ξ and α of Eq. (3.3.7), a fit of the results for 100 agglomerates with similar size and different fractal dimensions is calculated as follows

$$log\left(R_A \frac{d_A^2}{d_{pp}^2}\right) = log(\xi) + \alpha log(N_{pp}) \tag{3.3.15}$$

Six cases have been considered with different interception diameters of the agglomerate. For each case, 100 agglomerates have been generated with different fractal dimensions in order to have a representative sample. Within 100 agglomerates, 50 agglomerates have the maximum coordination number of 2 and the other 50 agglomerates have the maximum coordination number of 3. This choice is based on the representative distribution of the fractal dimension of all the agglomerates. For 100 agglomerates generated, the mean agglomerate diameter and the mean number of primary particles are determined. For agglomerates with small size ($\overline{d_A} \leqslant 109.7$ nm), our algorithm of structure generation cannot achieve high fractal dimension. Table 10 shows the results of ξ and α for all cases. The results of the linear regression to estimate ξ and α are presented by Figure 33 for two cases of $d_A = 100nm$ and $d_A = 400nm$, as an example.

			$D_f < 2.0$		$D_f > 2.0$		
d_{pp} (nm)	$\overline{d_A}$ (nm)	$\overline{N_{pp}}$	ξ	α	ξ	α	σ
20	71.3	4.64	1.265	0.734	/	/	0.024
20	89.67	6.86	1.255	0.773	/	/	0.0202
20	109.7	10.54	1.297	0.778	/	/	0.0198
20	211.3	45.68	1.425	0.787	1.811	0.729	0.0174
20	311.3	122.05	1.568	0.755	1.652	0.726	0.0135
20	411.6	261.82	1.014	0.879	3.016	0.626	0.0158
20	511.0	581.0	0.702	0.951	4.053	0.590	0.0125
20	611.9	1005.43	1.178	0.847	5.149	0.563	0.020

Table 10 – Average values of model coefficients ξ and α estimated from the numerical simulations. $\overline{d_A}$ and $\overline{N_{pp}}$ are respectively mean agglomerate diameter and mean number of primary particles. σ is standard deviation between numerical results and model.

The results obtained in Table 10 are different from the value obtained in [89] who found $\xi = 0.864$ and $\alpha = 0.935$. Indeed, [89] calculated the value of ξ and α for all the agglomerate diameters in the simulation and based on the criterion of the overlap indicator ([89]). Moreover, the authors calculated the fractal dimension by the plot $log(d_A/d_{pp})$ vs $log(N_{pp})$ and not by the numerical method.

The numerical values of ξ and α are presented for different agglomerate sizes. From those values, a relation between ξ and α in function of the agglomerate interception diameter d_A and the primary particles diameter d_{pp} is founded. From the results of Table 10, a linear regression for $\xi(D_f \geqslant 2.0)$ and $\alpha(D_f \geqslant 2.0)$ is performed and the results are presented by Figure 34.

Using a linear regression, ξ can be computed by

$$\xi = \begin{cases} 1.196 \pm 0.281 & \text{for } D_f < 2.0 \\ 0.182(d_A/d_{pp}) - 0.59 & \text{for } D_f \geqslant 2.0 \end{cases} \tag{3.3.16}$$

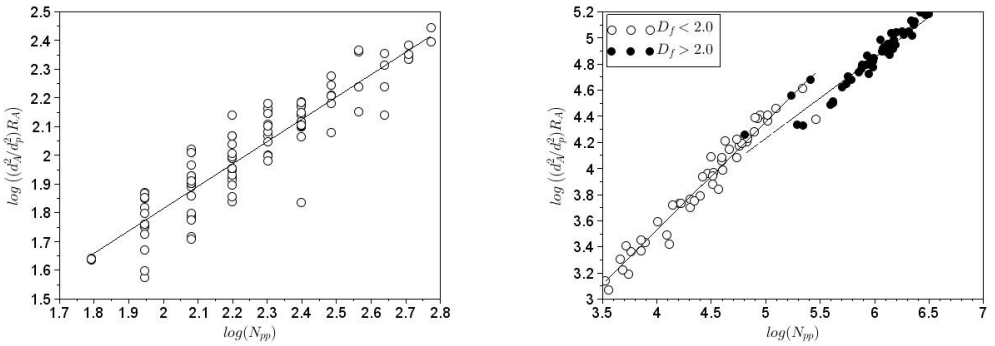

Figure 33 – The log of the collision probability coefficient with respect to the log of the number of primary particles in an agglomerate. Case of $\overline{d_A} = 109.7$ nm (left) and $\overline{d_A} = 411.6$ nm (right). For both cases, the primary particle diameter is $d_{pp} = 20$ nm. The line is the linear regression.

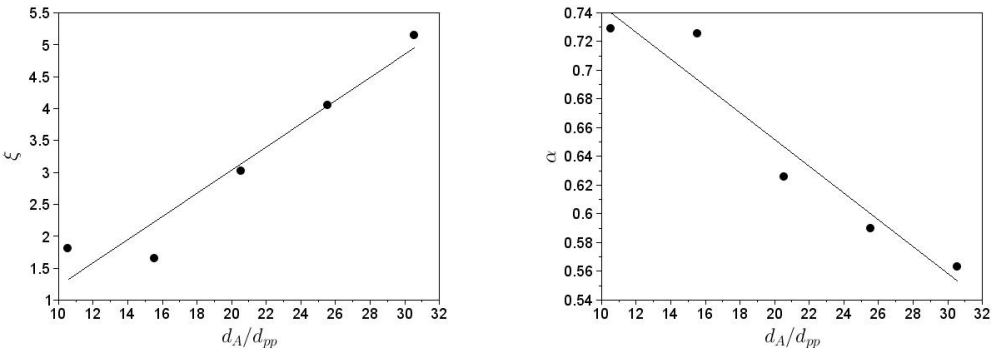

Figure 34 – Linear regression between $\xi(D_f \geqslant 2.0)$ and $\alpha(D_f \geqslant 2.0)$ with respect to the agglomerate size normalized by the primary particle size.(Left) Linear regression between $\xi(D_f \geqslant 2.0)$ and d_A/d_{pp}. $R^2 = 0.964$. (Right) Linear regression between $\alpha(D_f \geqslant 2.0)$ and d_A/d_{pp}. $R^2 = 0.961$.

and α by:

$$\alpha = \begin{cases} 0.833 \pm 0.068 & \text{for } D_f < 2.0 \\ -0.009(d_A/d_{pp}) + 0.838 & \text{for } D_f \geqslant 2.0 \end{cases} \tag{3.3.17}$$

The comparison between numerical results and model predictions is presented by Figure 35. The model corresponds to Eq. (3.3.7) with the number of primary particles from the numerical results. The values of ξ and α are calculated from Eq. (3.3.16) and Eq. (3.3.17) . Because of the limitation of calculation time, the highest ratio of agglomerate diameter to primary particle diameter considered is $d_A/d_{pp} = 600/20 = 30$. Therefore, the value of the linear regression for ξ and α is validated for this range of the agglomerate size. Eqs. (3.3.16) & (3.3.17) are expected to give good results for the agglomerate size

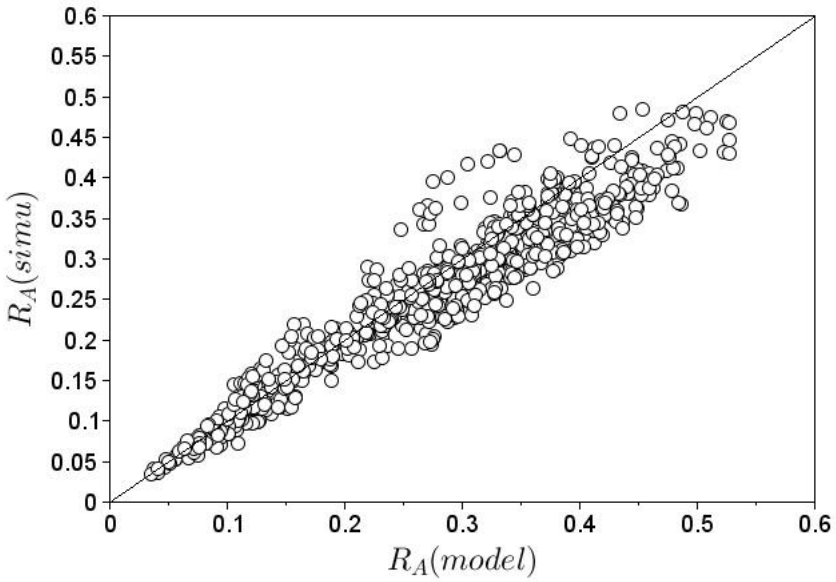

Figure 35 – Numerical results of the collision probability coefficient R_A compared to the model results for the case of collision between an agglomerate and a tracer. For the model, the values of ξ and α are calculated from Eqs. (3.3.16) & (3.3.17). The model is Eq. (3.3.7) with the number of primary particles from the numerical results. The line corresponds to numerical results equaling model results. The mean standard deviation $\sigma = 0.037$.

scale larger than $d_A/d_{pp} > 30$ but no validation is available yet.

3.3.3.2 Collision probability between an agglomerate and a spherical particle

For all simulations in this section, the primary particle size is $d_{pp} = 20$ nm. Four interception diameters of agglomerates were tested $\overline{d_A} = 311$ nm, 411 nm, 511 nm, 611 nm. For each interception diameter, 10 spherical particle sizes are tested. The value of the spherical particle diameter d_{p2} is presented in Table 11.

The comparison between numerical simulation results and model results is presented by Figure 36. The results show a very small discrepancy between the numerical simulation and the model with standard deviation of $\sigma = 0.0888$. It can be observed that in most of the cases, the model results underestimate the numerical results. This point can be explained by the approximation of the agglomerate mean cross section by the cross section of a spherical particle.

In practice, the only unknown parameter in Eq. (3.3.9) is the number of primary particles in an agglomerate N_{pp}. This parameter is often calculated by the fractal model

	$\overline{d_A} = 311$ nm	$\overline{d_A} = 411$ nm	$\overline{d_A} = 511$ nm	$\overline{d_A} = 611$ nm
$d_{p2}(nm)$	30	40	60	60
	60	60	100	1000
	120	80	1500	200
	180	100	200	300
	240	240	250	450
	300	400	5000	600
	450	600	750	900
	600	800	1000	1200
	750	1000	1250	1500
	900	1200	1500	1800

Table 11 – Value of the spherical particle diameter (nm) for collision with different agglomerate diameters.

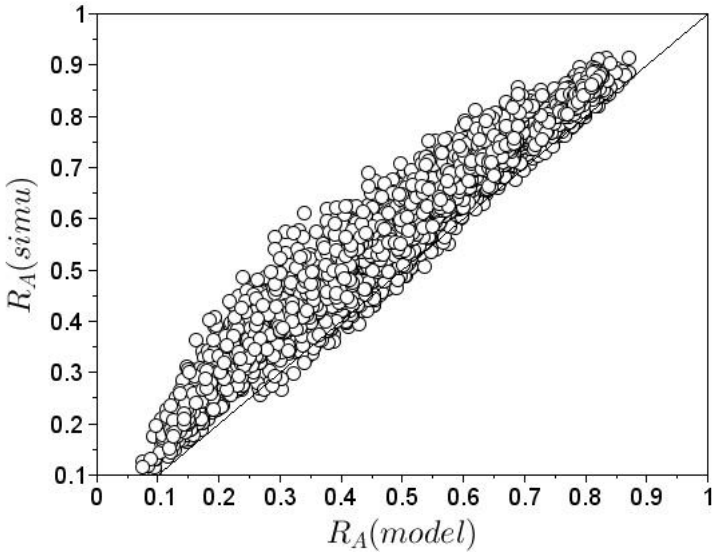

Figure 36 – Collision probability coefficient from the numerical simulation compared to the collision probability coefficient of the model. The model of R_A is Eq. (3.3.9). The correlations for ξ and α are respectively Eqs. (3.3.16) & (3.3.17). The number of primary particle N_{pp} is from the numerical simulation. The line corresponds to model results equal to numerical results. The standard deviation is $\sigma = 0.0888$.

following ([117])

$$N_{pp} = k_f \left(\frac{d_A}{d_{pp}} \right)^{D_f} \tag{3.3.18}$$

where $k_f = 0.414 D_f - 0.211$.

Figure 37 shows the results of R_A from Eq. (3.3.9) by calculating N_{pp} from the fractal model (Eq. (3.3.18)) and not from the numerical simulation. The results show the

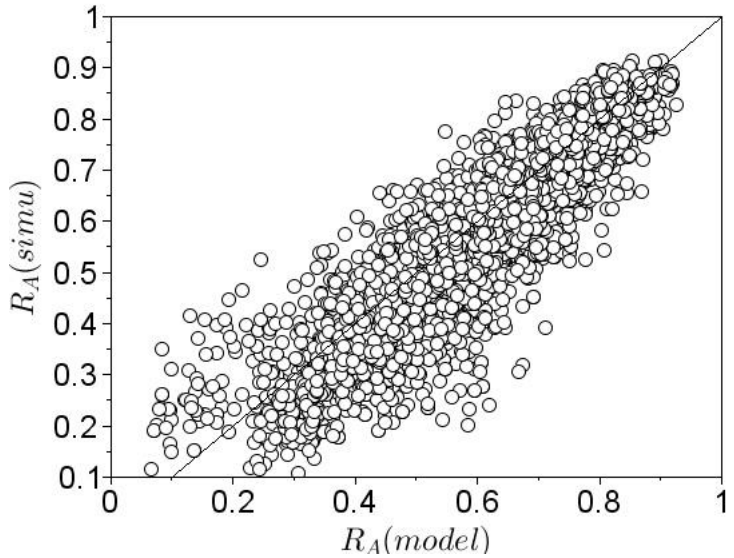

Figure 37 – Comparison between numerical simulation and model results for the case of the collision between an agglomerate and a spherical particle. In this results, the agglomerate primary particle number N_{pp} is calculated from Eq. (3.3.18) and not from the numerical simulation. The standard deviation $\sigma = 0.0818$.

consistency of using the fractal model for the determination of the collision probability coefficient R_A by our model.

In order to examine the trend and the limit of the collision probability coefficient R_A from Eq. (3.3.9), we calculated R_A in function of the spherical particle size d_{p2} for different agglomerate diameters and fractal dimensions. The results are shown by Figure 38 . When d_{p2} tends to infinity, R_A tends to 1 because the spherical particle cannot go through the agglomerate without collision, the fractal dimension becomes less important for the calculation of the collision probability coefficient. When the size of the agglomerate increases with a constant fractal dimension, the porosity of the agglomerate increases, R_A then decreases (see Figure 38).

3.3.3.3 Collision probability between two agglomerates

The parameters for two different agglomerates in collision are presented in Table 12. The comparison between the numerical simulations and the model is presented by Figure 39 .

The discrepancy between numerical results and model results is relative small with $\sigma = 0.0681$. The model results underestimate the simulation results because the agglom-

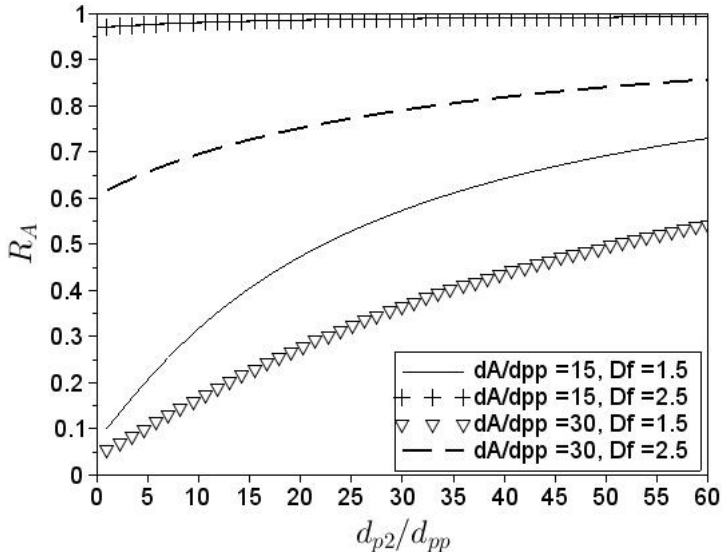

Figure 38 – Collision probability coefficient with respect to the spherical particle size normalized by the primary particle size with different agglomerate sizes and agglomerate fractal dimensions. Eq. (3.3.9) is used by calculating N_{pp} from Eq. (3.3.18).

$d_{pp1}(nm)$	$d_{A1}(nm)$	$d_{pp2}(nm)$	$d_{A2}(nm)$
20	300	20	60
20	300	20	90
20	300	20	120
20	300	20	150
20	300	20	210
20	300	20	240
20	300	20	300
20	400	20	60
20	400	20	80
20	400	20	120
20	400	20	160
20	400	20	240
20	400	20	320
20	400	20	400

Table 12 – Primary particle diameter and agglomerate diameter for different simulation cases.

eration cross section is approximated by the cross section of a spherical particle.

We compare the results of R_A from Eq. (3.3.10) by calculating $N_{pp,A1}$ and $N_{pp,A2}$

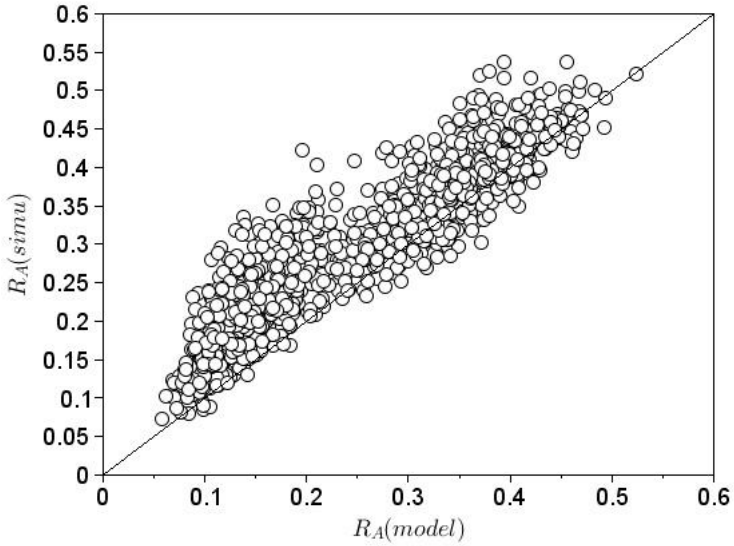

Figure 39 – Collision probability coefficient from the numerical results with respect to the collision probability coefficient from the model of Eq. (3.3.10). The line corresponds to model results equaling numerical results. The standard deviation is $\sigma = 0.0681$.

from the fractal model (Eq. (3.3.18)) and not from the numerical simulation. The results are showed by Figure 40. The results show the consistency of using the fractal model to estimate the collision probability coefficient R_A.

We analyze the trend and the limit of R_A from Eq. (3.3.10). The Eq. (3.3.10) is calculated for different sizes of d_{A2} and different fractal dimensions for both agglomerates. d_{A2} is considered as the larger agglomerate. The primary particle for both agglomerates are $d_{pp1} = d_{pp2} = 20$ nm. The size of the first agglomerate is fixed to $d_{A1} = 400$ nm. The result is presented by Figure 41 .

The results show that on one hand when the ratio of the agglomerate diameter d_{A2}/d_{A1} increases, the collision probability coefficient decreases because the porosity of the agglomerate 2 increases. On another hand when the fractal dimension of the agglomerate 1 increases, the collision probability coefficient increases because the agglomerate 1 is more dense. When the ratio of the agglomerate diameter d_{A2}/d_{A1} increases, the fractal dimension of the agglomerate 1 becomes less important for the calculation of R_A. Finally when the fractal dimension of the agglomerate 2 increases, the collision probability coefficient increases because the agglomerate 2 is denser. This point is related to the maximum value of R_A by Figure 41(a,b). The results show a good agreement for all variables with expected trends.

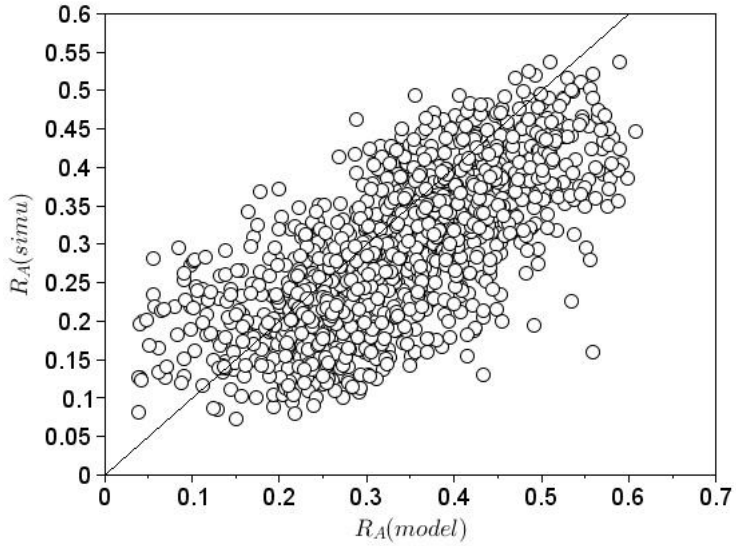

Figure 40 – Comparison between numerical simulation results and model results for the case of the collision between agglomerates. The primary particle number of the agglomerate 1 and 2 are calculated by Eq. (3.3.18) instead of the value from the numerical simulation. $\sigma = 0.0914$.

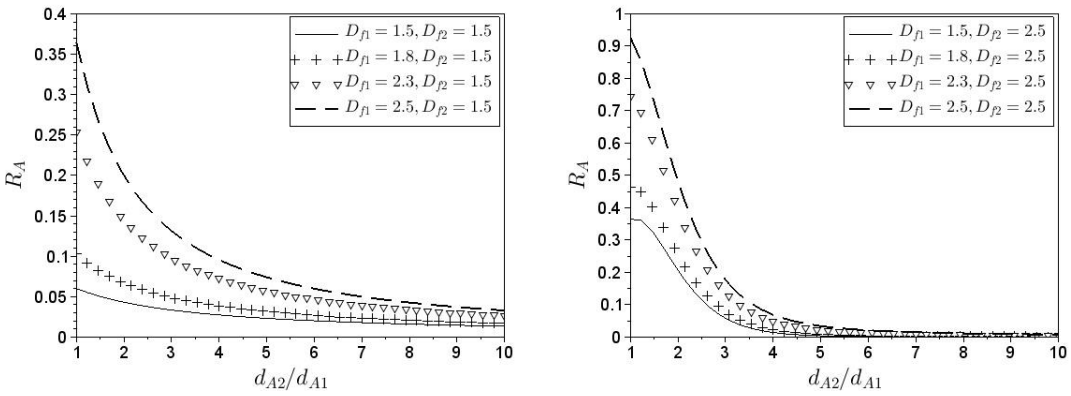

Figure 41 – Collision probability coefficient with respect to the ratio of the agglomerate diameter with different fractal dimensions of the agglomerates 1 and 2. Diameter of the agglomerate 1 is $d_{A1} = 400$ nm with $d_{pp1} = d_{pp2} = 20$ nm. The results are from Eq. (3.3.10). (Left) The fractal dimension of the second agglomerate is $D_f = 1.5$. (Right) The fractal dimension of the second agglomerate is $D_f = 2.5$.

3.4 Agglomerates collision in particle laden flow

In order to model the collision between spherical particles, a stochastic collision model with fictitious particles of Sommerfeld [104] by Monte-Carlo method is used in the present study. The dispersion model is first assessed and then the results with inter-particle collisions are compared to the results from the analytic model derived from the kinetic theory of rarefied gas.

The computational domain is a cube of the length of $L = 0.01\ m$ with 1000 cells and all boundaries are set as periodic boundary conditions. The particle are monodisperse spheres. The number of parcels has been set to 48,000 in order to have a good statistical convergence.

3.4.1 Turbulent dispersion model

Two dispersion models implemented in Code_Saturne are the one proposed by Minier [83] (hereafter named Model#1) and the second proposed by [102] (named Model#2). The main material properties of the fluid and the particles are given in Table 13 and Table 14.

Fluid viscosity, μ_f $(kg/m/s)$	1.72×10^{-5}
Fluid density, ρ_f (kg/m^3)	1.17
Fluid turbulence kinetic agitation, q_f^2 (m^2/s^2)	3.1×10^{-2}
Turbulence time scale, τ_f^t (s)	6.12×10^{-2}
Normal restitution coefficient, e_c	1
Time step simulation, Δt	0.001

Table 13 – Gas material properties.

Particulate diameter, d_p (μm)	600	600	600	600	600	600
Particulate density, ρ_p (kg/m^3)	18.75	37.50	75.00	150.00	300.00	450.00
Stokes number	0.22	0.43	0.85	1.70	3.22	4.58

Table 14 – Particle material properties.

At the beginning of the simulation, the particle and the fluid velocities are equal to zero. The dispersion model leads the mean fluid velocity to stay equal to zero however the fluid kinetic agitation develops and reaches a statistically steady state. The particles follows the same time-evolution. The time-average particle and fluid kinetic energy, computed at steady state, are shown by Figure 42. As well known, in homogeneous isotropic turbulent flows the particles reach an equilibrium well described by the Tchen-Hinze theory

$$2q_p^2 = q_{fp} = 2q_{f@p}^2 \frac{\eta_r}{1+\eta_r} \tag{3.4.1}$$

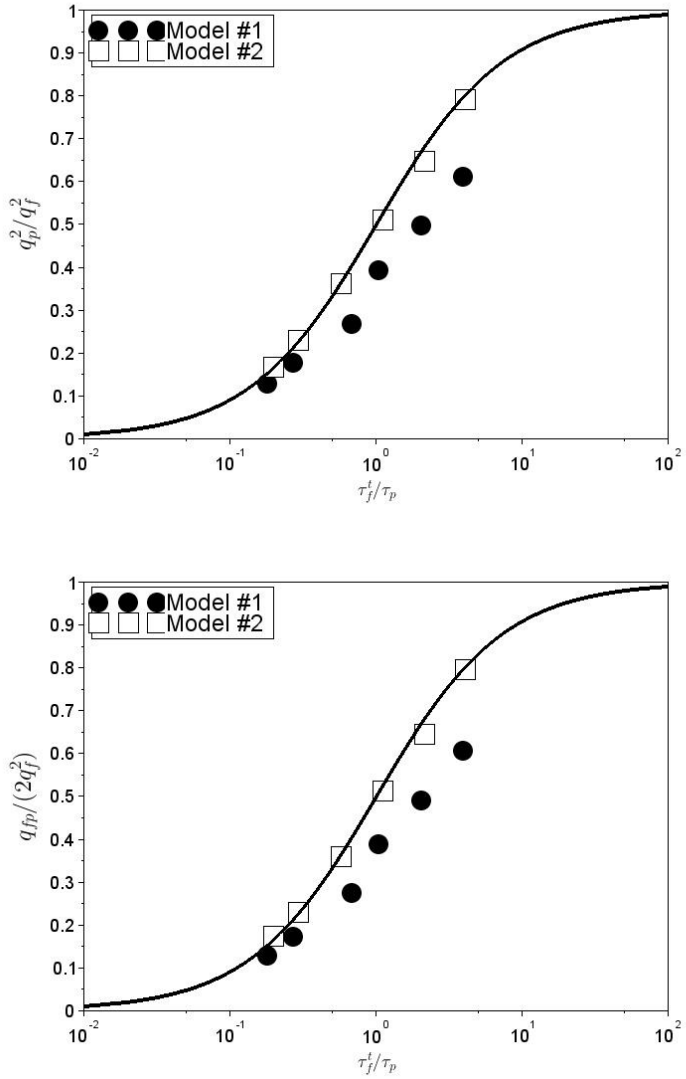

Figure 42 – Particle kinetic energy (top) and fluid-particle covariance normalized by the turbulent kinetic energy with respect to Stokes number. The black circles are the results from Model #1 and the black square are the results from Model #2. The solid line stands for Eq. (3.4.1).

where $\eta_r = \tau_f^t/\tau_p$ is the inverse of the Stokes number and q_{fp} is the fluid-particle covariance $q_{fp} = \left\langle u'_{f@p,i} u'_{p,i} \right\rangle$. The Tchen-Hinze theory is shown by Figure 42 (solid lines). It can be observed that surprisingly the Model#1 underestimate the particle agitation whereas the Model#2 is in accordance with the Tchen-Hinze theory.

3.4.2 Inter-particle stochastic collision model

The second step consists in the validation of the collision model by considering several particle volume fractions. In numerical simulation the number of parcels is unchanged and consequently the parcel statistical weight is adapted for each particle volume fraction. The inter-particle collision timescale is derived from the framework of the kinetic theory of dilute gases of rigid elastic sphere [17]:

$$\frac{1}{\tau_k^{pp}} = 4\pi n_p d_p^2 \sqrt{\frac{2}{3\pi} q_p^2} \tag{3.4.2}$$

where n_p in the particle number concentration, q_p^2 is the particle kinetic energy. In stochastic numerical simulation the collision frequency is computed with

$$f_{coll}(t) = \frac{N_{p,coll}(t)}{N_{p,tot}} \frac{1}{\Delta t} \tag{3.4.3}$$

where $N_{p,coll}(t)$ is the number of particles having the collision and $N_{p,tot}$ is the total number of particles.

Finally, the characteristic collision time scale of numerical simulation is calculated by definition:

$$\tau_{k,simu}^{pp} = \frac{1}{\langle f_{coll} \rangle_t} \tag{3.4.4}$$

where $\langle f_{coll} \rangle_t$ is the time-averaged collision frequency.

Figure 43 shows the comparison between the characteristic collision time scale from the numerical results and the model results with respect to the particulate volume fraction. As expected, when the volume fraction increases, the characteristic collision time scale decreases because the collision increases. The results from the numerical simulation are in good agreement with the results from the theoretical model (cf. Eq. (3.4.2)).

3.4.3 Inter-agglomerate and particle-agglomerate collision

The same test case as the collision between spherical particles test case is considered but for this test case, the parcels represent agglomerates.

3.4.3.1 Collision between an agglomerate and a spherical particle

In this case, the diameter of the fictitious particle is calculated depending on the agglomerate diameter by the ratio $(d_{fict}/d_A) = 0.5, 1, 2, 4$. The fractal dimension of the agglomerate ranges in $D_f = 1.8, 2.1, 2.5$. All other properties are given in Table 15 .

The inter-particle collision time scale reads [32]:

$$\frac{1}{\tau_{coll}^{pq}} = 4\pi d_{pq}^2 n_p \sqrt{\frac{1}{\pi} \frac{(q_p^2 + q_q^2)}{3}} \tag{3.4.5}$$

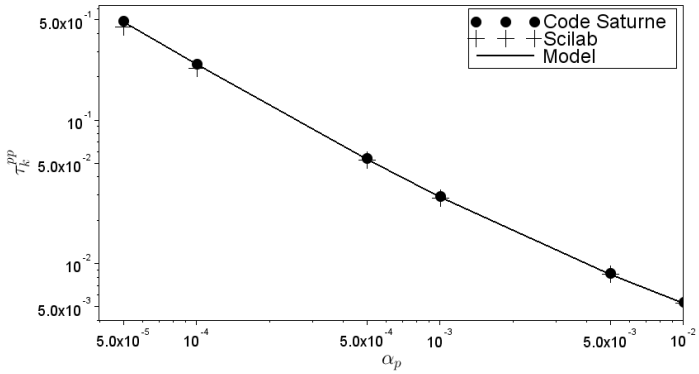

Figure 43 – Mean inter-particle collision timescale with respect to the particle volume fraction. The solid lines are from Eq. (3.4.2)

Viscosity, μ_f $(kg/m/s)$	1.72×10^{-5}
Density, ρ_f (kg/m^3)	1.17
Turbulence kinetic agitation, q_f^2 (m^2/s^2)	30.1×10^{-3}
Turbulence time scale, τ_f^t (s)	61.2×10^{-3}
Agglomerate diameter, d_A (μm)	400
Primary particle diameter, d_{pp} (μm)	20
Density, ρ_p (kg/m^3)	150.00
Agglomerate volume fraction, $\alpha_p(d_A)$	0.01
Stokes number $\tau_A/\tau_{f@A}^t$	1.70
Lagrangian time scale, $\tau_{f@A}^t/\tau_f^t$	1.06
Fluid kinetic energy, $q_{f@A}^2/q_f^2$	0.97
Elasticity coefficient, e_c	1

Table 15 – Fluid and agglomerate properties for all cases

where q_p^2 and q_q^2 correspond to the particle agitation of p- and q-particle, and $d_{pq} = (d_p + d_q)/2$ is the diameter.

In case of the collision between an agglomerate and a spherical particle, the agglomerate - particle collision time scale is estimated by

$$\frac{1}{\tau_{coll}^{AP}} = \left(d_{pp,A1}\sqrt{\xi_{A1}N_{pp,A1}^{\alpha_{A1}}} + d_{p2}\right)^2 \pi n_A \sqrt{\frac{1}{\pi}\frac{(q_A^2 + q_{p2}^2)}{3}} \tag{3.4.6}$$

where N_{pp} is the number of primary particles and d_{pp} is the primary particle diameter. The results of the simulation are shown by Figure 44 . The results show good agreement between the model results and the numerical simulation results. With dense agglomerates (high fractal dimension), the agglomerate collision frequency tends to the spherical particle collision frequency. The agglomerate collision frequency decreases when the

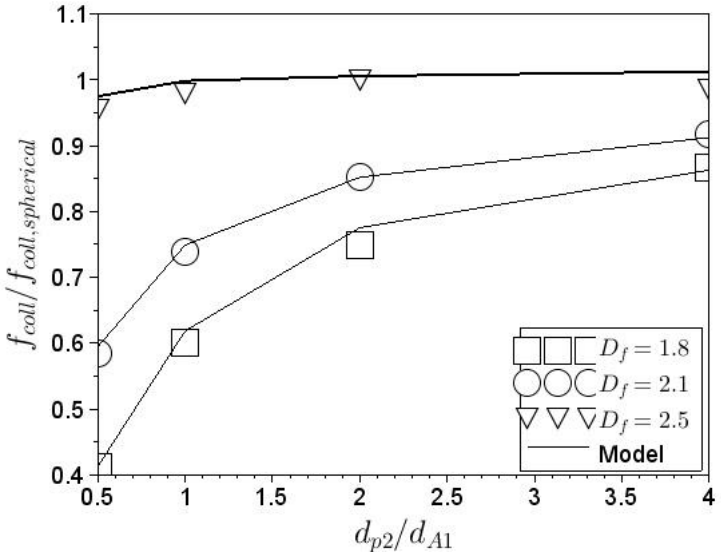

Figure 44 – Collision frequency between an agglomerate and a spherical particle normalized by the collision frequency between two spherical particles with respect to the ratio of the agglomerate size. The line stands for Eq. (3.4.6).

fractal dimension decreases. When the spherical particle size becomes very large compared to the agglomerate size, the collision frequency increases and agglomerate fractal dimension becomes less important. The trend of the results is as expected.

3.4.3.2 Collision between agglomerates

The inter-agglomerate collision time scale between agglomerates is:

$$\frac{1}{\tau_{coll}^{AA}} = \left(d_{pp,A1}\sqrt{\xi_{A1}N_{pp,A1}^{\alpha_{A1}}} + d_{pp,A2}\sqrt{\xi_{A2}N_{pp,A2}^{\alpha_{A2}}}\right)\pi n_A\sqrt{\frac{1}{\pi}\frac{(q_{A1}^2+q_{A2}^2)}{3}} \tag{3.4.7}$$

For this case, the fractal dimension of the agglomerates 1 and 2 changes and also the size of the agglomerate 2 . The fractal dimension of the agglomerate 1 has two values: $D_{f1} = 1.8, 2.5$ and the fractal dimension of the agglomerate 2 has two values: $D_{f2} = 1.8, 2.5$. The size ratio of the agglomerate 1 is $d_{A1}/d_{pp1} = 15$, the size ratio of the agglomerate 2 is $d_{A2}/d_{pp2} = 15, 30, 45, 60$. The primary particle of the agglomerate 1 is equal to the primary particle of the agglomerate 2 and is equal to $d_{pp1} = d_{pp2} = 20$ nm. The results of the test case are shown by Figure 45.

A good agreement between the model results and the numerical simulation results is obtained. The trend of the results is expected except for the configuration $d_{A2}/d_{A1} = 4$. In this case, the ratio size of the agglomerate 2 is $d_{A2}/d_{pp2} = 60$. As explained in the

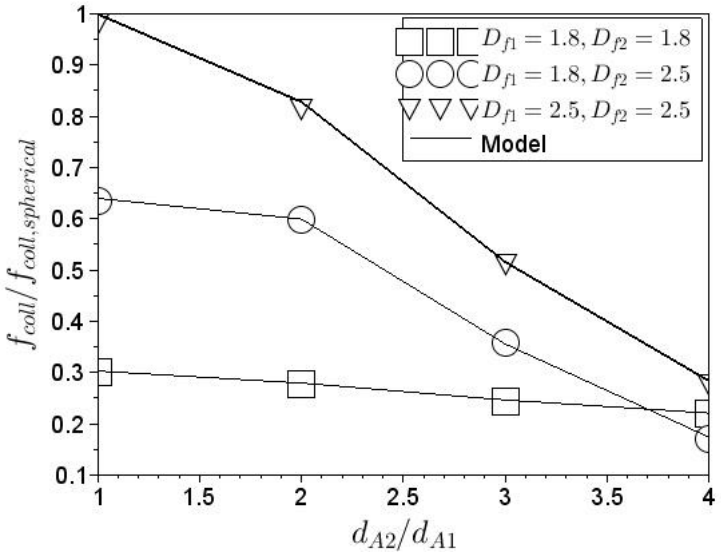

Figure 45 – Collision frequency between agglomerates normalized by the collision frequency between two spherical particles with respect to the ratio of the agglomerate size. The line stands for Eq. (3.4.7) .

model for ξ and α in section 3.3.3.1, the value of ξ and α are validated for the maximum ratio agglomerate size of $d_A/d_{pp} = 30$.

3.5 Agglomeration of agglomerates in the particle laden flow

In this section, the agglomeration modelling is presented. When a collision is detected, the agglomeration criterion, Eq. (2.3.5), is computed for detecting the agglomeration occurrence. In the present study, the agglomerates are presented by parcels with a statistical weight. When the agglomeration occurs between a real parcel and a fictitious parcel, the new properties of the parcel are calculated as follows to ensure the mass conservation:

$$N_{pp}^{+} = N_{pp}^{-} + N_{pp,fict} \tag{3.5.1}$$

$$w_p^{+} = w_p^{-} \left(1 - \frac{N_{pp,fict}}{N_{pp}^{-} + N_{pp,fict}} \right) \tag{3.5.2}$$

where the index $^-$ et $^+$ indicate the variable before and after the agglomeration respectively . N_{pp} and $N_{pp,fict}$ are the number of primary particles of the real parcel and the fictitious parcel respectively. w_A is the parcel statistical weight.

The configuration case of the agglomerate collision modelling is used for this case. The agglomerate and fluid properties are given in Table 16. The time step is equal

to $\Delta t = 0.001$ and is verified to be smaller than the collision time scale. The physical simulation time is 4 seconds. The volume fraction of the agglomerate phase is $\alpha_A = 10^{-3}$.

Gas properties	
Viscosity, μ_f $(kg/m/s)$	1.72×10^{-5}
Density, ρ_f (kg/m^3)	1.17
Turbulence kinetic agitation, q_f^2 (m^2/s^2)	3.01×10^{-2}
Turbulence time scale, τ_f^t (s)	6.12×10^{-2}
Agglomerates properties	
Diameter, d_A, (μm)	20
Fractal dimension, D_f	2.75
Diameter of primary particles, d_{pp} (nm)	20
Primary particle density, ρ_{pp} (kg/m^3)	450.00
Elasticity coefficient, e_c	0.9
Maximum deformation pressure, $\bar{p}$ (Pa)	5×10^9

Table 16 – Fluid and agglomerate properties in test case.

Figures 46 and 47 shows the evolution of the agglomerate total number and the agglomerate mean diameter respectively. Because of the agglomeration, the agglomerate mean diameter increases and the number of agglomerates decreases. This trend is well expected. The evolution of agglomerate number is stable after certain simulation time meanwhile the evolution of diameter is not stable.

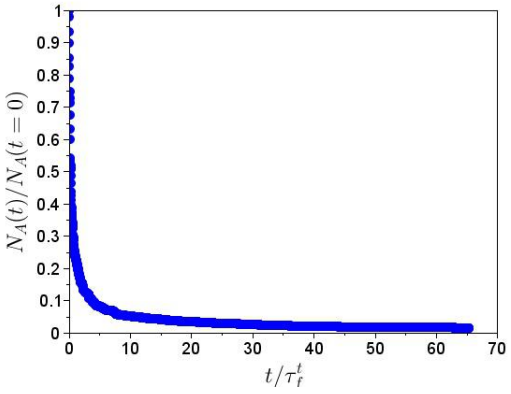

Figure 46 – Time-evolution of number of agglomerates.

One of the important parameter in the agglomeration modelling is the fluid turbulence kinetic energy. Some values of the turbulence kinetic k_f between 100×10^{-6} m^2/s^2 and 30.1×10^{-3} m^2/s^2 is tested in the present case. With a constant turbulence time scale $\tau_f^t = 61.2 \times 10^{-3}$ s^{-1}, the value of the fluid dissipation ε_f ranges between 7.87×10^{-4} m^2/s^3 and 0.237 m^2/s^3. Figures 48 and 49 show the agglomerate number and

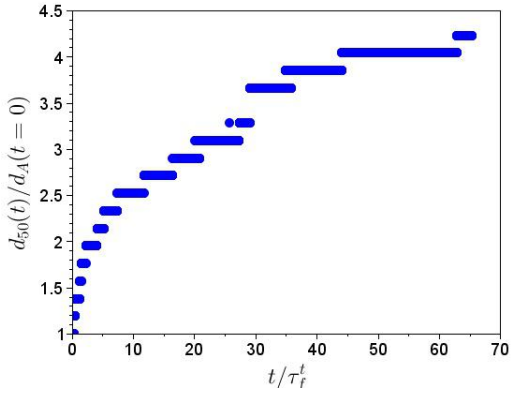

Figure 47 – Time -evolution of agglomerate median count diameter.

the agglomerate count median diameter respectively with respect to the fluid turbulence kinetic energy. The results show that a good agreement of the results from Code_Saturne and Scilab is obtained. When the fluid kinetic energy increases, the relative velocity between agglomerate increases, the collision increases. However, the interparticle force is not strong enough to adhere the agglomerates in collision, therefore the agglomeration decreases and the rebound becomes more predominant in the system.

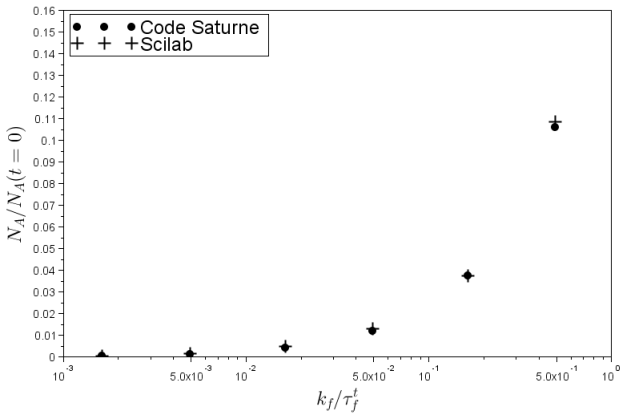

Figure 48 – Agglomerate number normalized by the initial agglomerate number with respect to the fluid kinetic energy normalized by the fluid turbulence time scale

3.6 Conclusion

In this chapter, physical phenomena related to nanoparticle agglomerates were modelled and developed in *Code_Saturne* and Scilab tool including the drag force on agglom-

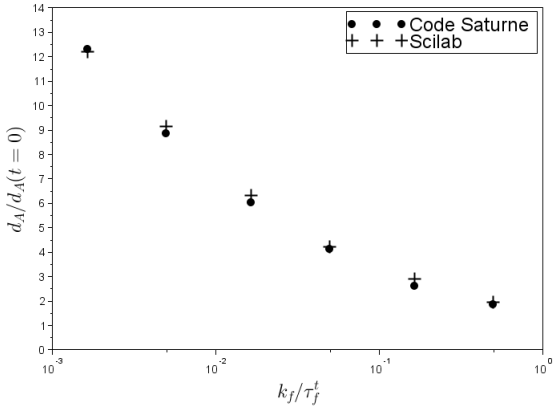

Figure 49 – Agglomerate median count diameter normalized by the initial agglomerate diameter with respect to the fluid kinetic energy normalized by the fluid turbulence time scale

erates, the agglomerates breakage by fluid turbulence, the collision between agglomerates and the agglomeration.

Regarding the drag force on agglomerates, a drag model taking into account the fractal dimension of the agglomerate has been developed in *Code_Saturne*. This is an issue for the dispersion modelling of agglomerates. The development was verified through the free fall simulation of different fractal dimensions of agglomerates.

The turbulence created by the jet is the main cause of agglomerate breakage. A probabilistic method for the agglomerate breakage modelling was developed in *Code_Saturne*. The development is validated by a good agreement obtained with Scilab tool. The simulation case with a homogeneous isotropic turbulence has shown that the agglomerate breakage occurs down a critical agglomerate diameter where the fluid agitation is not strong enough to break the agglomerates. A critical agglomerate diameter is found in function of the dissipation rate. The simulation of the agglomerate breakage in a jet configuration has shown that the agglomerate breakage is strong near the nozzle where the turbulent fluctuation are strong. When the agglomerates are far from the nozzle, the turbulent decreases and the agglomerate breakage decreases. In the future, a comparison between the numerical results and the experimental results need to be performed to fully validate the breakage modelling in *Code_Saturne*.

Because of the agglomerate shape, the collision probability for spherical particles cannot be applied for agglomerates. A new simple model to determine the collision probability for agglomerates is proposed in the present study. This new model allows to take into account the agglomerate geometry as the fractal dimension and the primary particle size in the modelling of the collision probability. The new model was validated with the numerical simulation of the collision between an agglomerate and spherical particles or between agglomerates. However, some additional physical phenomena need

to be considered in the probability collision modelling such as the Brownian motion and the flow around the agglomerate.

Regarding the agglomerate collision modelling, the probabilistic approach is used in the present study to model the collision between the agglomerates. The collision modelling is developed in *Code_Saturne* and is validated through the simulation of the particle collision in a homogeneous isotropic turbulence . A good agreement is obtained between the numerical results and the analytic model.

Concerning the agglomeration modelling, the deterministic approach is used in the present study. The development of this approach in *Code_Saturne* is validated by the simulation of the particles agglomeration in a homogeneous isotropic turbulence. A good agreement between the results from *Code_Saturne* and Scilab tool is obtained. The simulation case has shown that when the turbulence increases, the relative velocity between agglomerates increases, the rebound become dominant and the agglomeration decreases. In the future, the agglomeration modelling results could be compared with the experimental data if available.

In the next chapter, a numerical simulation case of a conveying pipe leakage in Blanzy, France in 2012 will be realized. All the physical phenomena presented in this chapter will be included. The results from *Code_Saturne* will be introduced as an inlet condition into an atmospheric dispersion modelling tool in order to simulate the nanoparticle dispersion in the large scale.

Chapter 4

Numerical simulation of an accidental pipe leakage

Contents

In the previous chapters, physical phenomena related to nanoparticles released in the air were modelled and implemented in *Code_Saturne*. In this chapter, a numerical simulation of the massive nanoparticle jet released is realized from the local leakage to the large scale simulation of atmospheric dispersion. *Code_Saturne* is used to simulate the nanoparticle jet in the vicinity of the leakage over time scale of seconds and length scale of several meters. The results from *Code_Saturne* will be an input data for the atmospheric dispersion simulation with ADMS (*Atmospheric Dispersion Modelling System*). ADMS is able to simulate particle dispersion on a large scale for time scale of hours and length scale of kilometers. The aim of this chapter is to show the application of *Code_Saturne* and to analyze the results of the atmospheric dispersion.

4.1 Configuration of the accidental case

The accidental pipe leakage occurred in Blanzy, France at 3:40 am during approximately 5 hours on November 18^{th} 2012 and led to an important exposure of the surroundings population to carbon black powder. Unfortunately, the available data of this

accidental case are very limited. The carbon black powder is stored in bulk in silos and is transported by the conveying pipe to another process equipment. Air is used to push the powder in package. This method of conveyance is characteristic of dense phase transport [81]. Because of the erosion of the pipe, the carbon black powder was released to the air. The mass released by the leakage was 5,000 kg of black carbon during approximately 5 hours corresponding to the mass flow rate of $Q_m \approx 0.278\ kg/s$. The length of the leakage was between 15 and 20 *cm* and its width was about several millimeters [1]. The characteristics of the powder (size distribution, morphology, and primary particle size) were not communicated by the industrial plant. The concentration and the deposition of the released black carbon were not measured after the leakage. In order to have a better view of the dispersion field of black carbon, we collected information, from the press article, on the locations where carbon black was found:

English translation [2]

It seems that the pollution is mainly concentrated on the sector of the Charbonnière district (the office of tobacco, the bar, the Republic street would have undergone the fouling), but deposits would have been seen until the Sablière district. At the moment we put on line, it is difficult to really know the amplitude of the damage and their geographical extents. However, we took pictures showing the gravity of the situation and gathered some testimonials from residents of the Charbonnière district who were, this morning, very angry in view of this polluting situation: Léon and Germaine Nowak, from René Cassin street, noticed a layer of black dust this morning when they woke up and fearing that their 2 white cats turn black, they keep them locked up. The soil, the terraces, everything is dirty. Their neighbor, Maurice Mennuni, who lives in the Jean Moulin street, 50 meters away noticed that the whole exterior of their house is blackened, the walls, the vehicles, the terraces, the balcony, the sills and window sills, everything is soiled.

English translation [3]

The diagnosis has not yet been realized by the environment manager but east area of the plant (Charbonniere street, Mépliers street...) is the most affected.

According to those information, we reconstitute the deposition distance of the black carbon with the IGN map [4] as shown in Figure 50.

Dimensions of the industrial plant is approximately 500 m wide and 700 m long. The exact location of the release in the industrial plant is not known. We assume that the release point is at the center of the industrial plant. One point on each street (Mepliers street, Charbonnière street and Jean Moulin street) were selected on the map to measure the distance compared to the industrial plant. The first point on the Mepliers street is approximately 500 m away from the industrial plant and the two other points on the Charbonniere street and the Jean Moulin street are approximately 1 km away from the

1. https://www.aria.developpement-durable.gouv.fr/accident/43049/
2. http://charolais-news.com/faits-divers/9450-incident-cette-nuit-de-samedi-a-dimanche-a-lusine-michelin-de-blanzy.html, consulted day: 12/12/2017
3. http://www.lejsl.com/actualite/2012/11/18/blanzy-fuite-de-noir-de-carbone-a-l-usine-michelin-udis, consulted day: 12/12/2017
4. https://www.geoportail.gouv.fr/donnees/carte-ign

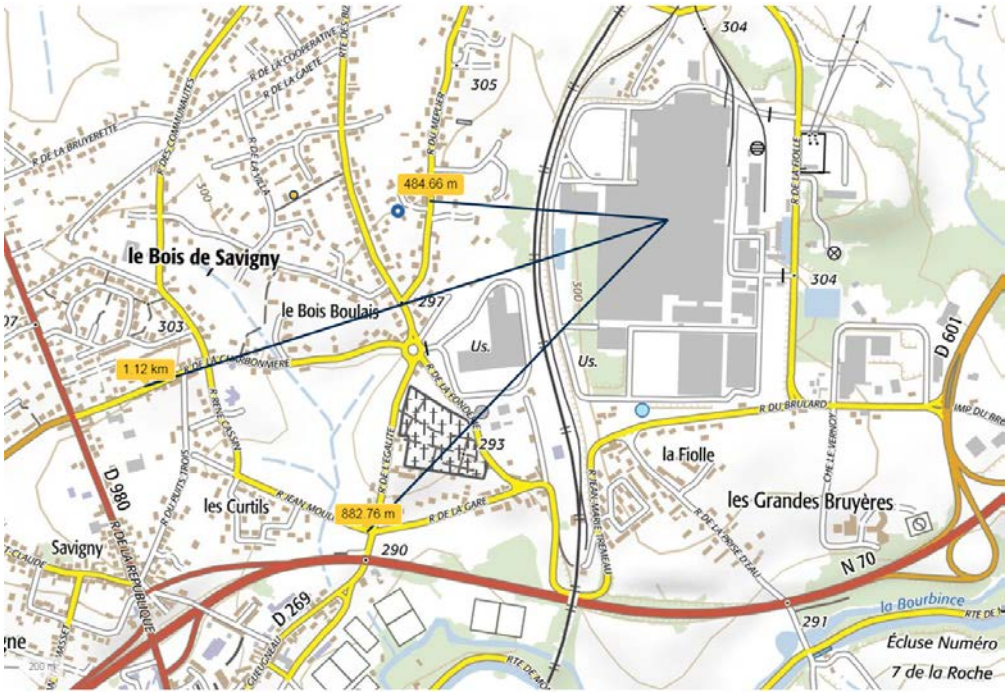

Figure 50 – Estimation of the deposition distance. The grey building is the industrial plant where the leakage occurred.

industrial plant. The dispersion of black carbon could have gone further away than those points.

Figure 51 shows the configuration for the numerical simulation of the accidental case in Blanzy. The leakage occurred on the roof of the building at 10 m height. The height of the leakage from the roof is considered negligible compared to the height of the building, therefore the height of the leakage is also 10 m. The release is supposed in upward vertical direction with a uniform velocity profile of the black carbon jet at the leakage of the pipe. It must be pointed out that, because of the release height, the wind profile is assumed to be constant, uniform and perpendicular to the jet direction. The field near the leakage is simulated by Code_Saturne in order to model the important physical phenomena related to nanoparticles as described in the previous chapters. The results from Code_Saturne will be an input for the numerical simulation tool, ADMS, for the large scale dispersion modelling .

4.2 Numerical simulation with *Code_Saturne*

4.2.1 Configuration and parameters

Figure 52 shows the boundary conditions of the numerical simulation. The jet enters the domain by the Inlet face and in the z-direction. The height of the domain is chosen

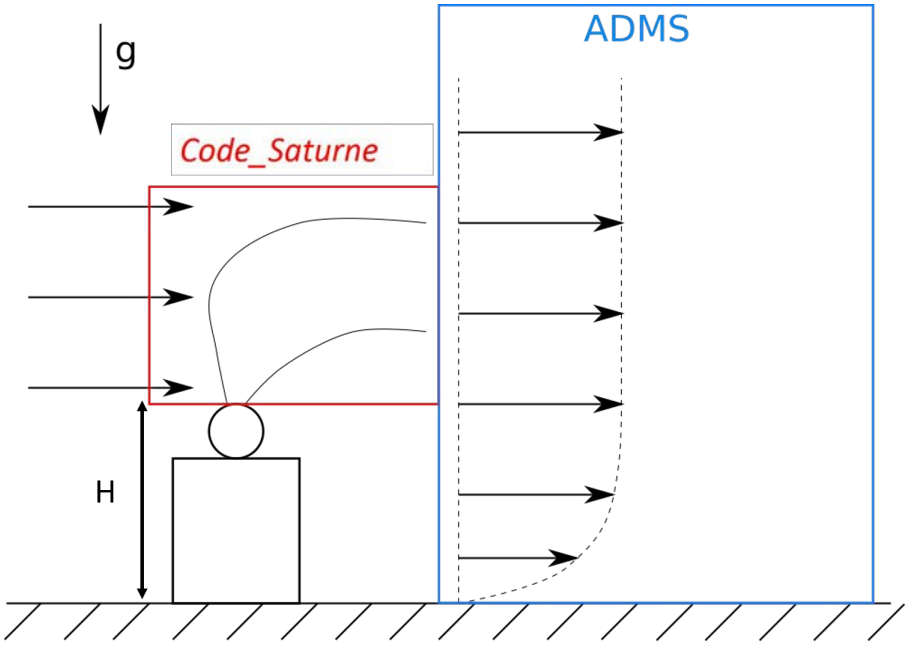

Figure 51 – Schematic representation of the configuration for the numerical simulation of the accidental case in Blanzy

as 7 m with 4 m above the release point and 3 m under the release point. The width of the domain is 4 m. The wind enters the domain by the left face and in the x-direction. The distance between the Inlet of the wind and the Inlet of the jet is 1 m. The distance between the inlet of the jet and the right face of the domain is 15 m. All other faces of the domain are set as free Outlet for the gas and the particulate phase. The gravity direction is the opposite of the z-direction.

Figure 53(top) shows the mesh used in the present simulation. The mesh is composed of 72450 cells. A refinement of the mesh is realized near the jet Inlet in order to model the dispersion of the jet. Figure 53(bottom) shows the mesh of the Inlet face. The jet Inlet is chosen as a square. Because the velocity spatial distribution of the jet is not considered, the Inlet face is meshed only by 9 cells. The size of the edge of the jet Inlet is $a = 17.1\ mm$ having the same surface of a circle orifice of diameter of 19.3 mm.

Table 17 summarizes the gas and agglomerates properties in the numerical simulation of *Code_Saturne*.

The parameters of the simulation are as follows:

— One-way coupling
— $k_f - \varepsilon_f$ standard turbulence model
— Drag model for agglomerates.
— Breakage and agglomeration of agglomerates modelling
— Coupling with ADMS

The initial condition of the wind field corresponds to a uniform wind field in the

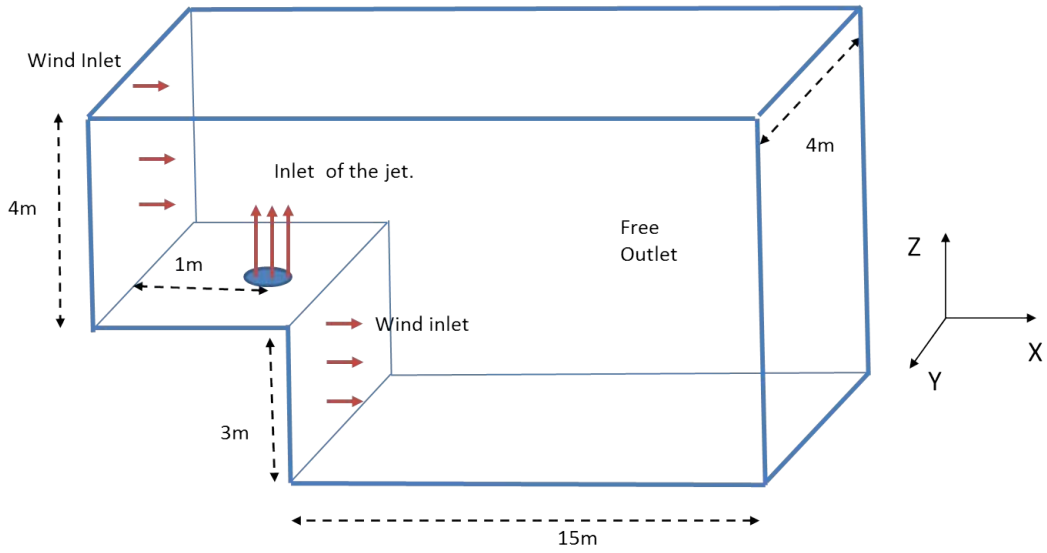

Figure 52 – Boundary conditions in the numerical simulation

Gas properties	
Uniform profile wind velocity	3 m/s
Uniform profile jet velocity at nozzle	10 m/s
Agglomerates properties	
Carbon black mass flow rate	0.278 kg/s
Primary particle size	20 nm
Fractal dimension	2.5
Primary particle density	2500 kg/m^3
Agglomerate diameter	100 nm
Hamaker constant	15.6×10^{-12} J
Minimal distance between primary particles	0.4 nm

Table 17 – Gas and agglomerate properties in the numerical simulation of *Code_Saturne*

whole domain. The numerical simulation proceeds in 2 steps:

1. Simulation of the release in order to obtain a stationary velocity field for the gas phase.
2. Simulation of the agglomerate phase with the steady air velocity field.

4.2.2 Numerical results and discussion

Figure 54 shows the gas velocity field. The domain is large enough to damp the influence of the jet velocity on the fluid velocity near the Outlet faces. Figure 54(bottom) shows the change of the gas velocity because of the wind field. This behavior is well

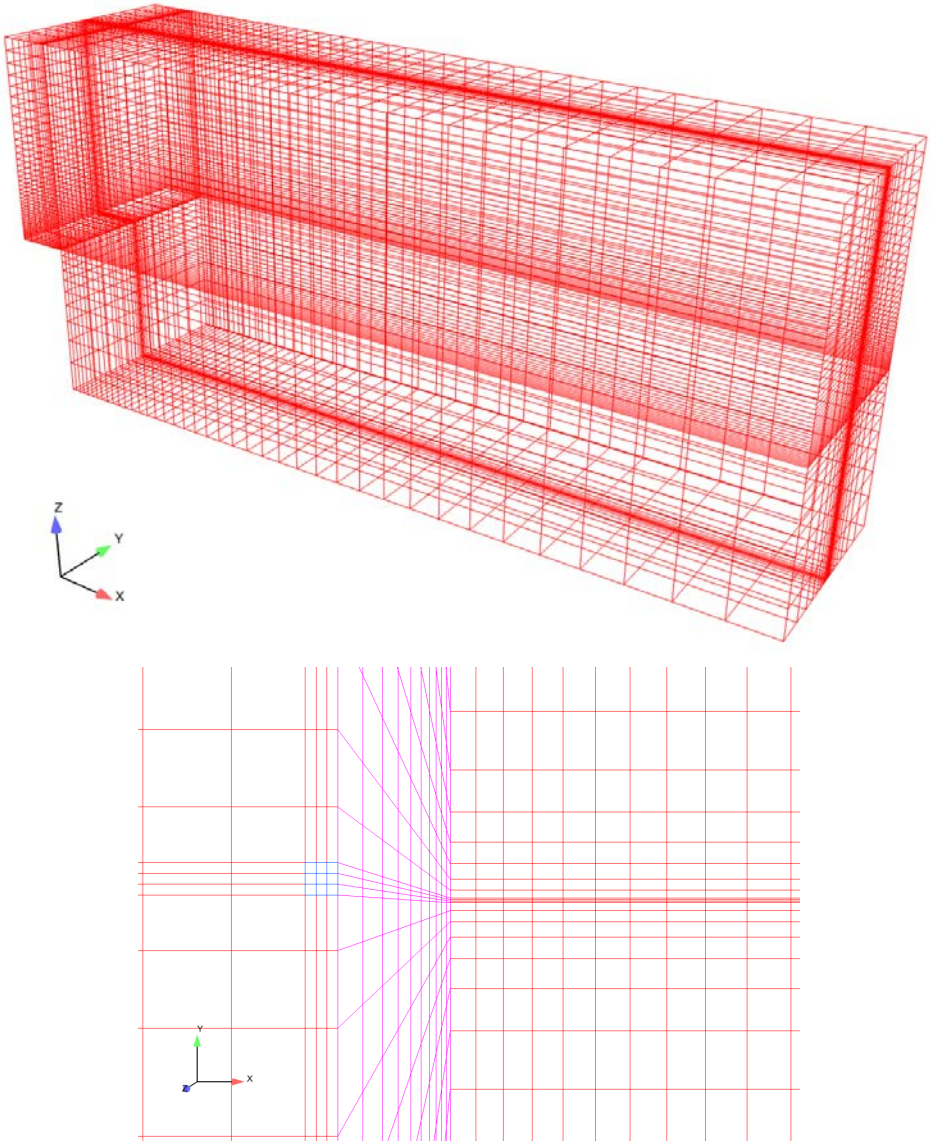

Figure 53 – Mesh used in the numerical simulation (top) and zoom in inlet face colored by the blue line (Bottom).

expected. When the air velocity field is obtained, the agglomerates are injected and the statistical post-processing of the Lagrangian results is performed.

We show here the statistical method used to determine several parameters of the Lagrangian results. The collision frequency is calculated as follows:

$$f_{coll}(t) = \frac{N_{A,coll}}{N_A} \frac{1}{\Delta t} \tag{4.2.1}$$

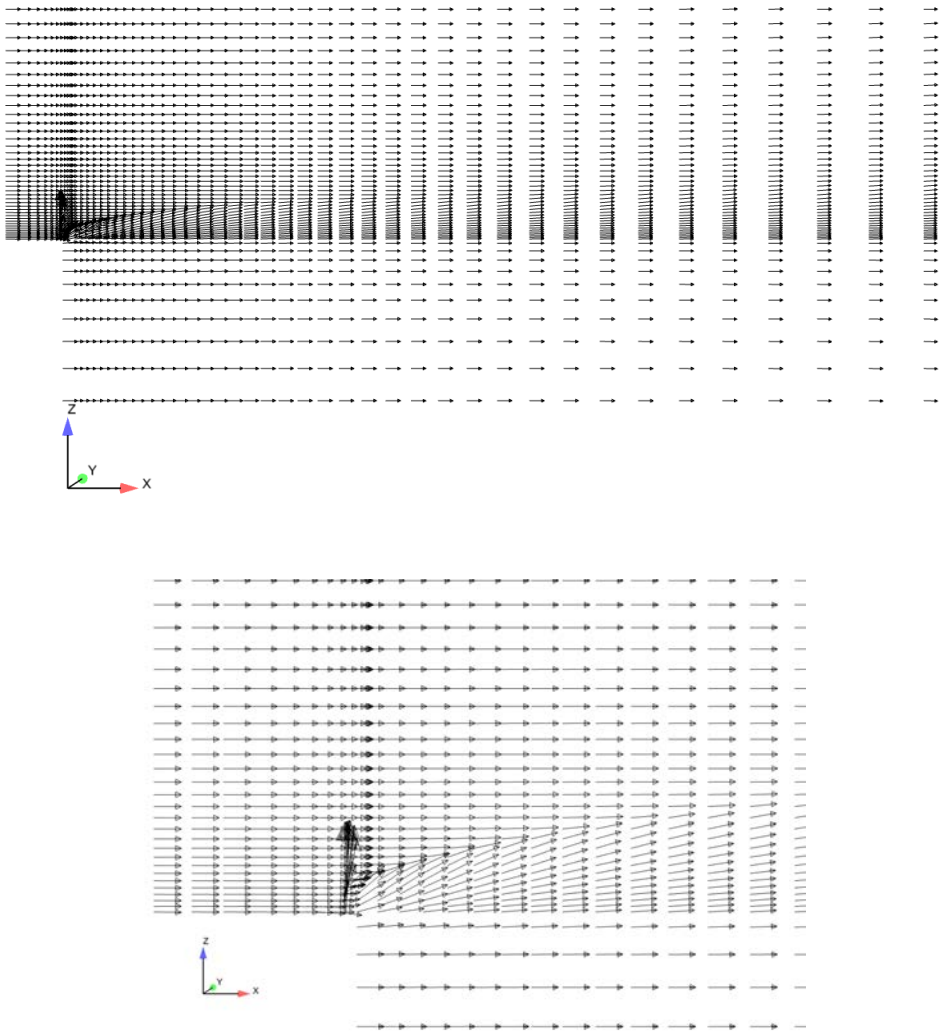

Figure 54 – Gas velocity field in the slice of the middle (top) and zoom on Inlet (bottom).

where $N_{A,coll}$ is the number of agglomerate having a collision during the simulation time step Δt. N_A is the total agglomerate number inside the domain.

The collision characteristic time scale is then deduced:

$$\tau_{coll}(t) = \frac{1}{f_{coll}(t)} \tag{4.2.2}$$

The agglomeration frequency $f_{agg}(t)$ is also calculated by replacing $N_{A,coll} \equiv N_{A,agg}$

in Eq (4.2.1) where $N_{A,agg}$ is the number of agglomerates having an agglomeration in the domain. The agglomeration characteristic time scale is deduced by replacing $f_{coll}(t) \equiv f_{agg}(t)$ in Eq (4.2.2).

The space-average diameter of agglomerate is calculated as follows:

$$\langle d_A \rangle(t) = \int_{parcels \in V_{stat}} d_A(\mathbf{x}, t)\Gamma(\mathbf{x})d\mathbf{x} \tag{4.2.3}$$

where V_{stat} is the volume for the statistical calculation. $\Gamma(\mathbf{x})$ is an indicator function. $\Gamma(\mathbf{x}) = 1$ if the parcel is inside the volume V_{stat}, otherwise $\Gamma(\mathbf{x}) = 0$.

The time-average of the agglomerate diameter is calculated as follows:

$$\overline{d_A} = \int_{t_0}^{t_0+\delta t_s} \langle d_A \rangle(t)dt \tag{4.2.4}$$

where t_0 is the starting time of the statistic and δt_s is the time during which the statistic is performed.

Figure 55 shows the dispersion of the agglomerate phase and the modification of the agglomerate diameter because of the agglomeration. Figure 55(top) shows the view of the agglomerates phase in z-direction. The width of the agglomerates flow in y-direction does not have a great change in the downstream direction. Figure 55(middle) shows the view of the agglomerate phase in y-direction. Near the jet Inlet, the agglomeration is not well observed. After this field, the agglomeration becomes stronger. The larger agglomerates are mostly seen in the bottom part of the release. Figure 55(bottom) shows the view of the agglomerate phase in x-direction. The larger agglomerates are seen as well inside the release where the agglomerate number concentration is high.

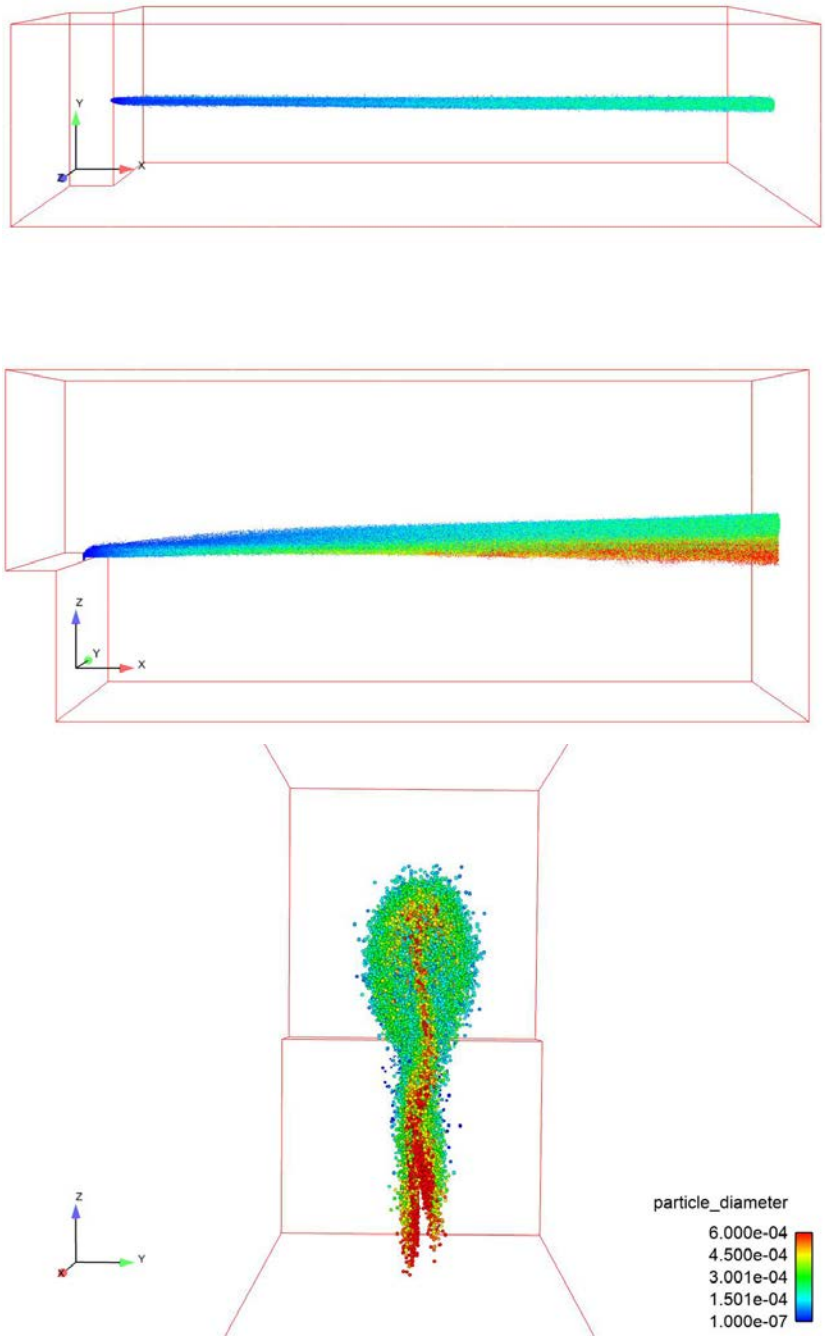

Figure 55 – Dispersion of the agglomerates view in z-direction (top), in y-direction(middle) and in x-direction (bottom) . The parcels are colored by their diameters.

Figure 56 shows the time-average agglomerate diameter and number at the oulet face. The results have an agreement with the Lagrangian results as shown by Figure 55 (bottom). The result shows that the particulate phase exiting the domain does not have a circular shape because of the sedimentation of the large agglomerates. Because of the agglomeration, the mean agglomerate number is small in the cell where the mean agglomerate diameter is high.

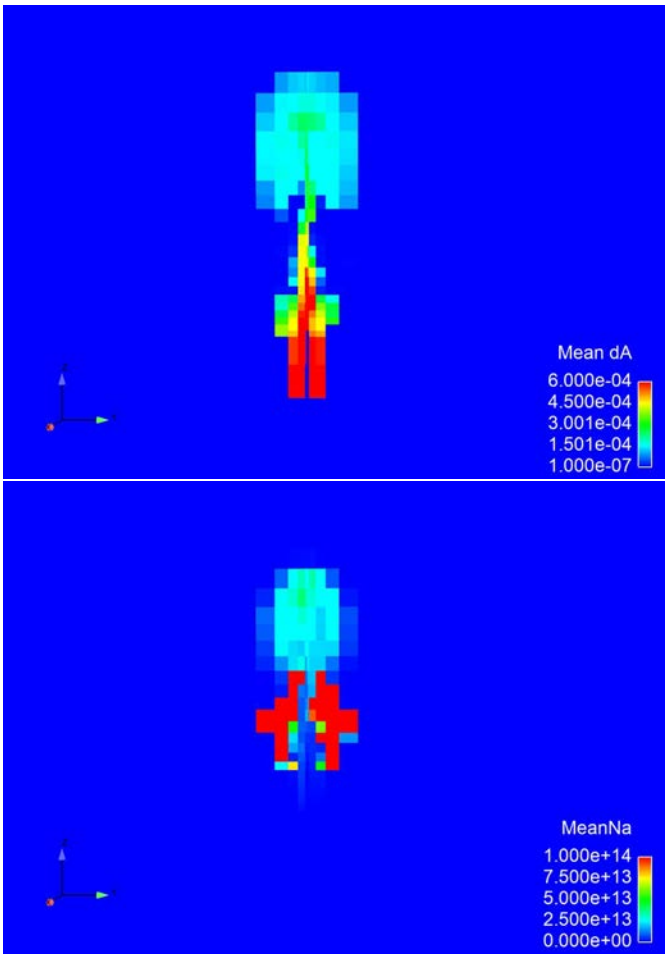

Figure 56 – Time-average agglomerate diameter (top) and time-average agglomerate number (bottom) at the outlet face.

Figure 57 (top) shows the time evolution of the total number of parcels in the domain. After 6 seconds of physical time, the total number of parcels in the domain is unchanged indicating that the number of parcels exiting the domain is equal to the number of parcels injected in the domain. Figure 57 (bottom) shows the time evolution of the total agglomerate number in the domain. At the very first numerical iterations, the total agglomerate number increases by the injection of parcels but very quickly, the total agglomerate number fluctuates because of the agglomeration. The agglomeration does

not change the total agglomerate mass, the time-average agglomerate mass flow rate exiting the domain is verified to be equal to the agglomerate mass flow rate entering the domain.

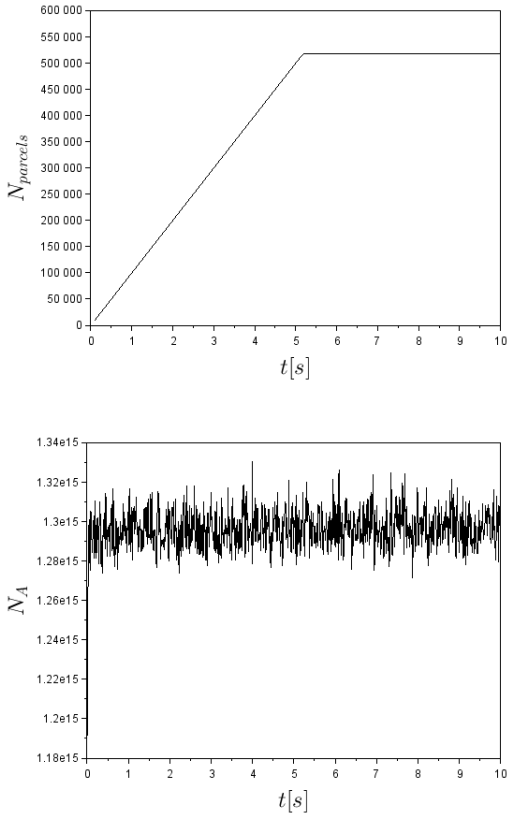

Figure 57 – Time evolution of total number of parcels (top) and total number of agglomerates (bottom) in the domain.

Figure 58 shows the time evolution of the collision characteristic time scale and the agglomeration characteristic time scale within the domain. The collision and agglomeration occurred already in the first seconds of the simulation. The collision time scale and the agglomeration time scale tend to the steady state after 4 - 5 s of physical time. Figure 58 also shows that the agglomeration characteristic time scale is larger than the collision characteristic time scale because of the rebound of the agglomerate.

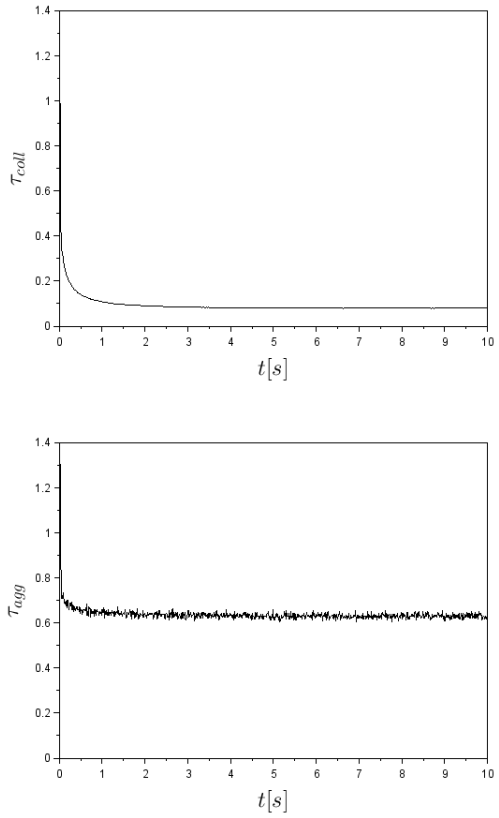

Figure 58 – Time evolution of the collision characteristic time scale (top) and the agglomeration characteristic time scale (bottom) within the domain

The Outlet of the domain is chosen 15 m away from the jet Inlet in the x-direction. The distance is chosen in order to ensure that near the Outlet, the agglomeration does not have a strong influence on the agglomerates properties. Figure 59 shows the comparison of the size and mass distribution function for all agglomerates positioned between $x =$ 14 m - 15 m and between $x =$ 13 m - 14 m. The results show that the agglomerate diameter distribution does not change, the Outlet distance is chosen far enough.

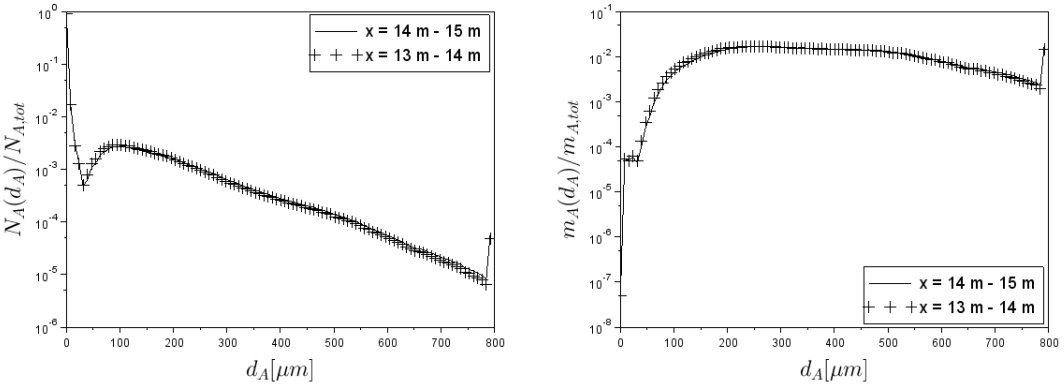

Figure 59 – Frequency of the PDF in number (left) and in mass (right) for $x = 14$ m - 15 m and $x = 13$ m - 14 m

We choose to represent the PDF by only 5 classes of agglomerate diameter in order to couple the results with ADMS. The agglomerate distribution function in number and in mass are calculated from the Lagrangian results for all the parcels whose position is between $x = 14$ m -15 m. The first class contains all agglomerates whose size is smaller than 10 μm. The second class contains all agglomerates whose size is between 10 μm and 50 μm. The third class contains all agglomerates whose size is between 50 μm and 100 μm. The fourth class contains all agglomerates whose size is larger than 400 μm. For each agglomerate class, an arithmetic average value of agglomerate diameter is calculated. The results show that for the smallest agglomerate class of 2 μm, the number ratio is very high but it corresponds to very low mass ratio. On the other hand, the 500 μm have a mass ratio very high compared to their respective low number ratio.

Limit agglomerate diameter	Average agglomerate diameters (μm)	Number ratio	Mass ratio
$d_A \leqslant 10\ \mu m$	2	0.918	2.66×10^{-4}
$10\ \mu m < d_A \leqslant 50\ \mu m$	20	0.0098	3.58×10^{-4}
$50\ \mu m < d_A \leqslant 100\ \mu m$	80	0.015	0.013
$100\ \mu m < d_A \leqslant 400\ \mu m$	200	0.052	0.524
$d_A > 400\ \mu m$	500	0.0052	0.463

Table 18 – Number ratio and mass ratio of 5 agglomerates classes.

The input data for ADMS is as follows:
— Agglomerate total mass flow rate: $Q_{m,A} = 0.278\ kg/s$
— The gas mass flow rate is equal to the sum of mass flow rate of the wind and the mass flow rate of the jet : $Q_{m,g} = 99\ kg/s$.
— In ADMS, the release is considered to have a circular shape. Therefore, the

diameter of the circle having the same surface of the Outlet face of Code_Saturne is calculated. The diameter of the release is therefore $d_{release} = 5.97$ m

— The jet is positioned at 10 m height. The center of the release is equal to the center of the Outlet face of Code_Saturne. The height of the source is therefore $H_{release} = 10.5\ m$

— Agglomerate diameter distribution function as shown in Table 18

4.3 Large scale simulation of the release using ADMS

In this section, the simulation of the agglomerate dispersion on large scales using ADMS (*Atmospheric Dispersion Modelling System*) is presented. The ADMS tool is not dedicated to simulate the nanoparticle dispersion. Therefore, the complex physical phenomena related to nanoparticles in large time and space scale as: nucleation, condensation - vaporization (cf. Chapter 2) are not modelled in ADMS.

4.3.1 Introduction to ADMS

ADMS v5.0, developed by CERC, allows to model the atmospheric dispersion over short scale (typically in kilometers) from one or several source terms. In order to simulate the dispersion of a plume, ADMS use a Gaussian plume model 'second generation'. Figure 60 shows the principal method used by ADMS. ADMS calculates the concentration of pollutant (gas or particles) in the center of the plume in function of the space and time. After that, ADMS deduces the concentration for all other points in the plumes by a Gaussian distribution..

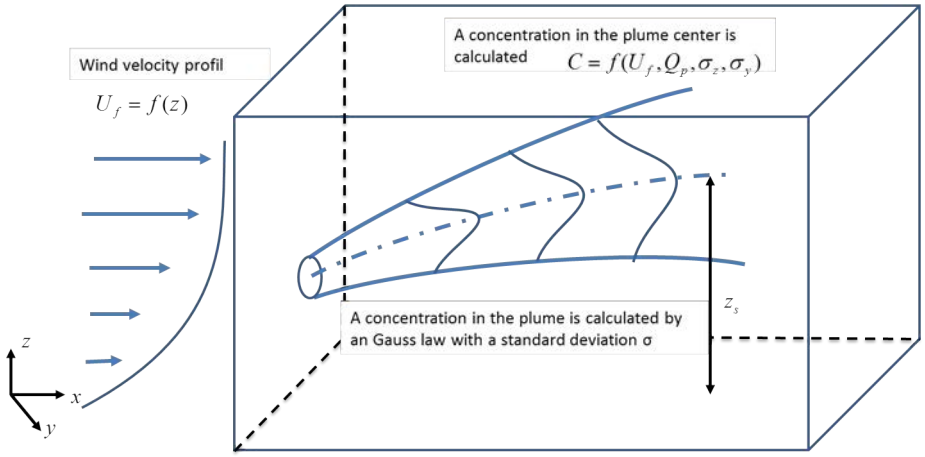

Figure 60 – Schematic representation of the atmospheric dispersion modelling method in ADMS. Where C is the concentration of the particle, U_f is the velocity of the fluid flow, Q_p is the particle mass flow rate, σ_z and σ_y are respectively the standard deviation of the mass concentration in z and y direction.

The mass concentration distribution in the plume is calculated as follows [44]:

$$C(x,y,z) = \frac{Q_S}{2\sqrt{2\pi}\sigma_y\sigma_z U_w} e^{-\frac{y^2}{2\sigma_y^2}} \left(e^{-\frac{(z-z_s)^2}{2\sigma_z^2}} + e^{-\frac{(z+z_s)^2}{2\sigma_z^2}} + e^{-\frac{(z+2h-z_s)^2}{2\sigma_z^2}} + e^{-\frac{(z-2h+z_s)^2}{2\sigma_z^2}} + e^{-\frac{(z-2h-z_s)^2}{2\sigma_z^2}} \right) \tag{4.3.1}$$

where:

— x, y, z are the spatial position
— C is the mass concentration of the disperse phase.
— Q_S is the intensity of the source whose unity is $kg/m^2/s$. $Q_S = Q_m/S_{src}$ where $Q_m[kg/s]$ is the mass flow rate of the pollutant and S_{src} is the surface of the source.
— U_w is the wind speed. In case of calm winds where $U_w \to 0$, Eq (4.3.1) diverges. Therefore, the wind speed in this case is set to the minimal value of $U_w = 0.5$ m/s by convention [44].
— z_s is the height of the source as shown in Figure 60.
— σ_z and σ_y are respectively the standard deviation of the concentration in the z and y direction.

Important input parameters in ADMS are the weather conditions. The weather conditions define the atmospheric stability and is an index to estimate the standard deviation σ_z and σ_y in Eq. (4.3.1). The most widely used method was developed by Pasquill [90] and slightly modified by Turner [113]. Pasquill proposed six atmospheric stability classes based on five classes of the wind speed, three classes of day time insolation and two classes of night time cloudiness. Table 19 shows the Pasquill atmospheric stability classes.

Wind speed, m/s	Day time insolation			Night time conditions	
	Strong	Moderate	Slight	Thin overcast or > 4/8 low cloud	< 3/8 cloudiness
<2	A	A-B	B		
2	A-B	B	C	E	F
4	B	B-C	C	D	E
6	C	C-D	D	D	D
>6	C	D	D	D	D

Table 19 – Meteorological conditions defining Pasquill turbulence types. A: Extremely unstable conditions. B: Moderately unstable conditions. C: Slightly unstable conditions. D: Neutral conditions. E: Slightly stable conditions. F: Moderately stable conditions. [90].

In function of the turbulent state of the atmosphere, the standard deviation σ_z and σ_y are defined. The detail of the model of the standard deviation is not published.

ADMS considers the particulate phase as a passive tracer transported by the fluid phase where inertial effect is negligible. However, ADMS considers the deposition physical phenomena that depends on the particle diameter and density. In addition, ADMS allows to take into account several physical phenomena in the atmospheric dispersion of gas or particles as follows:

— Roughness of the surface
— Presence of the building
— Dry and wet deposition of gas and particles
— Chemical aspect of NO_x
— Radioactivity of several components, etc...

In the present study, the only additional physical modelling considered is the dry deposition of particles. The dry deposition of particles in the air depends on the particle properties, the meteorological condition and the deposition surface. This subject has been investigated widely in the literature. For more information about the dry deposition modelling, the reader can refer to the review of Sehmel [98]. The simplest model to calculate the dry deposition rate is as follows [44] :

$$F_{depo,dry} = u_d C(x, y, 0) \tag{4.3.2}$$

where $F_{depo,dry}$ is the dry deposition rate (unity of $\mu g/m^2/s$). $C(x, y, 0)$ is the mass concentration of the disperse phase at ground level $z \to 0$ m. u_d is the deposition velocity. The deposition velocity is the sum of two velocities which are the terminal velocity u_{ts} and the diffusive velocity. The terminal settling velocity for agglomerate is presented in Chapter 2.2.3. The diffusive velocity is caused by the Brownian motion which is important for particles size less than 100 nm (cf. Chapter 2.2.4) . The diffusion velocity by the Brownian motion is not well modelled yet in the literature [44] and is not modelled in the present study.

4.3.2 Configuration and parameters

Table 20 synthesizes the parameters considered in the ADMS simulation. In *Code_Saturne*, the outlet face have the dimension of 4 m of width and 7 m of height. The source has the same surface as the outlet face in *Code_Saturne* which gives the diameter of source equal to 5.97 m. The gas mass flow rate which enters the domain of ADMS is equal to the sum of the mass flow rate of the wind and the jet exiting the domain in *Code_Saturne*. The height of the center of the release is estimated at 10.4 m from *Code_Saturne*. The total agglomerate mass flow rate input in ADMS is also from *Code_Saturne*.

Unfortunately, there were no weather stations at Blanzy, where the accidental leakage occurred, but we used the meteorological data of the nearest weather station, in the Lyon city approximately 100 km away from Blanzy. The data of the weather station gives the value of the wind speed and the cloud recovery during the night of November 18^{th} 2012 when the accidental leakage occurs. The wind velocity varies between $2.1 < U_w < 4.6$ m/s and the cloud recovery is 70% within 5 hours at night. The wind direction is 130° which means that the wind heads to South-East direction but Figure 50 seems to shows

Height of the source	10.4 m
Diameter of the source	5.97
Mass flow rate of the source	99.0 kg/s
Total agglomerate mass flow rate	0.278 kg/s
Wind velocity at 10 m height	3 m/s
Cloud recovery	70 %

Table 20 – Parameters chosen in ADMS.

that the wind heads to South - West direction. Because of the lack of the weather data at Blanzy, we assume the wind velocity to 3 m/s in the South-West direction. The atmospheric stability is *E: Slightly stable conditions* or *D:Neutral conditions*. As shown in Figure 50, the dispersion terrain is urban.

In ADMS, the agglomerate properties as the primary particle size, the primary particle density and the agglomerate fractal dimension are the same as in *Code_Saturne*. 5 classes of diameter of agglomerates are considered. The agglomerate density and the agglomerate mass flow rate are calculated for each agglomerate class as shown by Table 21. The agglomerate density decreases greatly when the agglomerate size increases because the agglomerate porosity increases. The mass flow rate of each agglomerate class is calculated in function of the mass ratio of each class as shown by Table 18.

Agglomerate diameters (μm)	Agglomerate density (kg/m^3)	Mass flow rate (g/s)
2	182.8	0.07
20	64.34	0.1
80	32.67	3.614
200	20.67	145.67
500	12.92	128.7

Table 21 – Density and mass flow rate of each agglomerate class.

The physical time simulated is 5 hours corresponding to the duration of the release in the accidental case. Numerical simulations of a duration of the release of 3 hours have shown no differences of the results.

4.3.3 Preliminary test

In Eq. (4.3.1), the particle size is not taken into account as a parameter. The particle size parameter may be taken into account in the deposition rate model. Additionally, as shown by Table 21, the small agglomerates of $d_A = 2$ μm have density of $\rho_A = 182$ kg/m^3 and the large agglomerates of $d_A = 500$ μm have density of $\rho_A = 12.92$ kg/m^3. When the agglomerate diameter decreases or the agglomerate density decreases, the terminal settling velocity decreases. But in the present case, the agglomerate density of small agglomerates is higher than the large agglomerates. The prediction of the terminal settling velocity or the deposition rate becomes more complicated. The aim of this test

case is to verify if there are differences of the dispersion behavior between two different particles size. Two monodisperse cases corresponding to two values of the agglomerate diameter $d_A = 2\ \mu m$ and $d_A = 500\ \mu m$ are tested.

Figure 61 shows the deposition rate on the ground and the mass concentration at center of the jet as a function of the distance from the release source. The results show that the $d_A = 500\ \mu m$ case still has a higher deposition rate with a smaller density. Because of the deposition, the mass concentration of the case of $d_A = 500\ \mu m$ decreases faster with respect to the distance from the source.

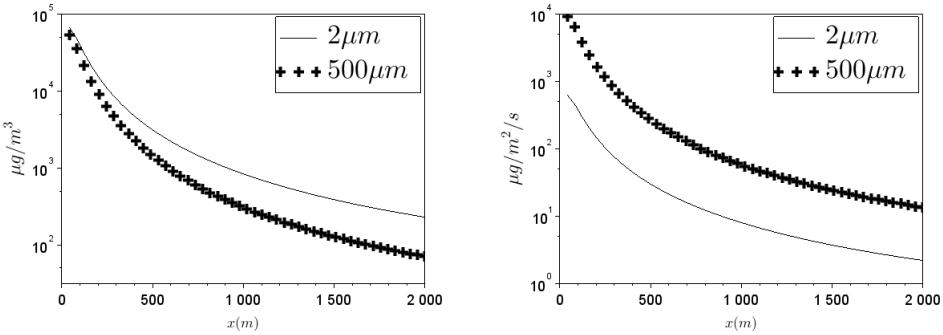

Figure 61 – Agglomerate mass concentration (left) and agglomerate deposition rate (right) for the agglomerate of $d_A = 2\ \mu m$ and $d_A = 500\ \mu m$ as a function of the distance from the release source at the center of the release.

4.3.4 Numerical results and discussion

Figure 62 shows the total number concentration of the agglomerate phase in the height of $z = 1.5$ m for 5 hours of physical time. Near the source, the particle number concentration is very high and decreases with distance from the source.

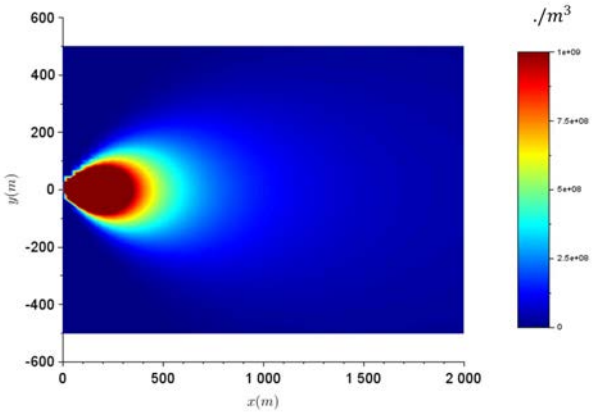

Figure 62 – Number concentration of agglomerates at the height of $z = 1.5$ m. The physical time is 5 hours.

Figure 63 shows the profile of the number concentration and the mass concentration of each agglomerate class at the center of the release with respect to the distance from the source. The number concentration decreases very slowly with the distance (4.48×10^8 m^{-3} at 500 m from the source to 6.8×10^7 m^{-3} at 1400 m from the source). ADMS shows that the dispersion of the carbon black can reach 1 km from the release source which is in agreement with the observations.

For small agglomerates, the number concentration is much higher than the number concentration of the largest agglomerates (up to 10^3 times between the case of 2 μm and 500 μm) but the mass concentration is much lower than the largest agglomerate (up to 10^4 times between the case of 2 μm and 500 μm). Figure 63 (left) shows that the number concentration of $d_A = 2$ μm is approximately equal to the total number concentration of the mixture. Figure 63 (right) shows that the mass concentration of large agglomerates of 200 μm and 500 μm is very high compared to other agglomerates class.

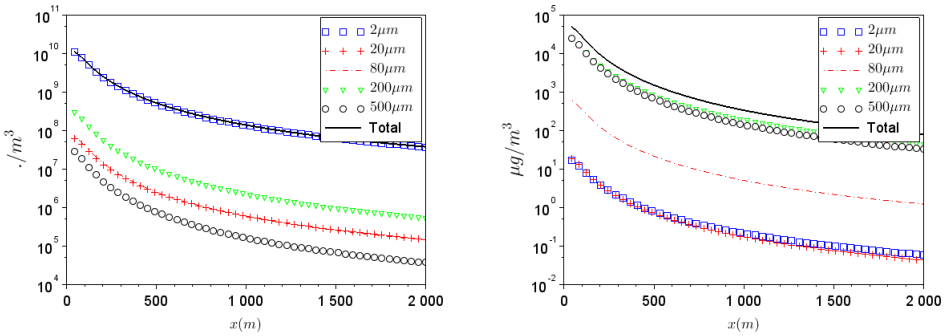

Figure 63 – Agglomerate number concentration (left) and agglomerate mass concentration (right) of all agglomerate size class in x direction at y = 0.

Figure 64 shows the deposition rate of total agglomerates. The deposition rate field is very close to the number concentration field showed by Figure 62. Indeed, the deposition rate is proportional to the number concentration by Eq. (4.3.2).

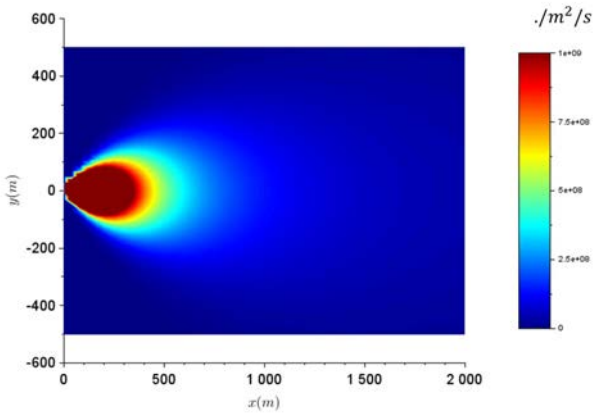

Figure 64 – Deposition rate of agglomerates at ground level.

Figure 65 shows the profile of the number deposition rate (left) and the mass deposition rate (right) of each agglomerate class in x direction at y = 0 and z = 0. The deposition rate has the same trend as the number concentration. Figure 65 (left) shows that for the largest agglomerate class, the deposition rate decreases faster because of a greater terminal velocity. However, the mass concentration of the large agglomerates are still higher than the mass concentration of the small agglomerates at 2 km from the source.

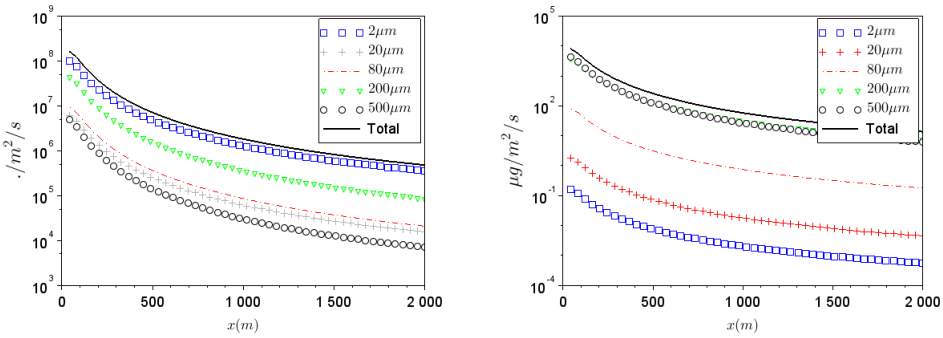

Figure 65 – Number deposition rate (left) and mass deposition rate (right) of all agglomerate size classes in x direction at y = 0.

Figure 66 shows the number concentration of the release (total number concentration of all agglomerates class) onto the map of Blanzy. The results show that the dispersion

field given by ADMS cover the places where the carbon black was found which is in agreement with the observations. The quantitative results of the concentration number and the deposition rate of agglomerates can be determined for each position in the map.

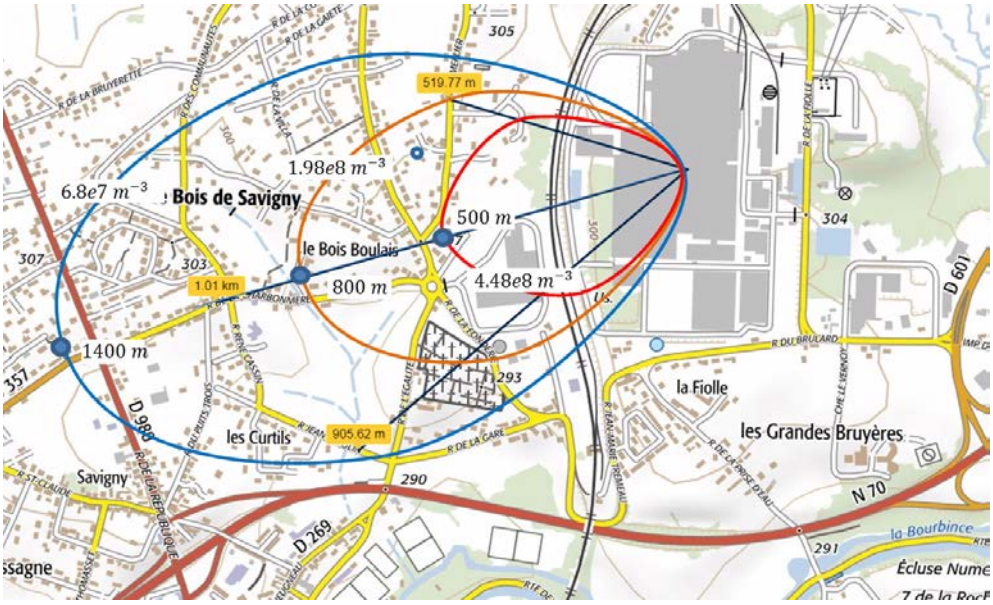

Figure 66 – Isoline of the agglomerate number concentration in the accidental case in Blanzy from simulation.

Quoting the French Ministry of Environment, article N° R221-1 to R221-3, the alert threshold for pollution due to fine particles of diameter below 10 μm is a daily average concentration of 80 $\mu g/m^3$. In the case of the accidental release in Blanzy, the exposure may have been short but the mass concentration of particles was much higher than this limit: 320 $\mu g/m^3$ at approximately 1 km away from the source and 1000 $\mu g/m^3$ at 500 m from the source.

This modelling study demonstrated the capability of our model to assess not only the mass concentration but also the number concentration. Results presented in this study show that the number of particles increases with decreasing particle size. It raises questions about the relevance of using mass concentration or number concentration as criteria for toxicity. This issues was discussed by Beaudrie et al. [10]. Although mass concentration has traditionally been used as the metric for exposure assessment to airborne particles and the basis for regulation, several studies suggested that at similar concentrations, nanometric sized particles are more harmful than micron-sized particles [14]. According to Beaudrie et al. [10] , it is worth pointing out that since the number of particles and particle surface per unit mass increase and pulmonary deposition increases with decreasing particle size, dose by particle number or surface area will increase as size decreases for a same mass concentration. Exposure assessments that rely on mass concentration could underestimate ultrafine particle toxicity, since these particles do not contribute significantly to total mass concentration despite their high number. There-

fore, particle numbers and surface area concentrations have been proposed as alternative metrics for experimental observation studies. Results have shown that in some cases, better, i.e. more reliable, dose-response relationships were obtained when dose was expressed with reference to surface area or number concentrations whereas in other cases using mass concentration seemed more appropriate. These contrasted results could be attributed to the variable weight of different mechanisms and parameters involved in the interaction between the particles and the target organs: chemical activity of the substance, size, shape, specific surface area and surface coating. Since investigations [28, 79, 24] on these parameters are still in the early stages, there is no official recommendation yet to take into account the number concentration as criterion for toxicity.

4.4 Conclusion

With the available information about the accidental pipe leakage in Blanzy, France in 2012, the leakage of conveying pipe was modelled in this chapter. We used two numerical simulation tools in order to simulate the dispersion of nanoparticle agglomerates in air. *Code_Saturne* was used to simulate the nanoparticle jet near the leakage over time scale of seconds and length scale of meters. In this part, the physical phenomena related to nanoparticle agglomerates was taken into account as: specific drag on agglomerate, breakage and agglomeration of agglomerates. The results of *Code_Saturne* were used as input data for ADMS, the second numerical tool, in order to simulate the dispersion of nanoparticles for large scales in both time and space. The results show that the nanoparticles could be deposited more than 1 km away from the source which is in agreement with the deposition map. The results also shows that at 1 km from the source, the total mass concentration of the particles is 10 times higher than the alert limit imposed by the Ministry of Environment. In addition, the alert limit based on the mass concentration may be not relevant for the case of nanoparticle agglomerates because the number concentration of agglomerate smaller than 10 μm is very high whereas its mass concentration is very weak compared to all other agglomerates class.

This accidental case study has shown the application of the physical phenomena modelling developed in *Code_Saturne*. *Code_Saturne* is able to predict the nanoparticle dispersion behavior in the near field and to determine quantitatively the number and size distribution of nanoparticles, the velocity, the mass flow rate, the height and the equivalent diameter of the release. This information is required by most of numerical tools of atmospheric dispersion to be able to model the dispersion of particles over large time and space scales.

Chapter 5

Conclusions and future work

A massive release of nanoparticles in air occurred in Blanzy, France in 2012 leading to the significant exposure of surroundings population and environment to nanoparticles whose potential negative effect is still not well known. In order to evaluate the effective distance of such a massive release of nanoparticles in air, the aim of the present study was to understand and model the physical phenomena related to nanoparticles in air and to propose a numerical tool for the prediction of nanoparticle dispersion, in term of the number concentration and the size distribution.

In the literature, each study investigated only specific physical phenomena related to the dispersion of nanoparticles in air but a global view of different physical phenomena was not realized yet. The first part of the work consisted in the synthesis of the physical phenomena related to nanoparticles in the configuration of a nanoparticle jet into the air. This synthesis provided a better understanding of the nanoparicle behaviors when they are released in the air. By a simple approach or from the literature data, the relevance of those physical phenomena was estimated. In the configuration of the jet, the predominant physical phenomena considered for the modelling step are: drag on agglomerates, agglomerates breakage by fluid and agglomeration of agglomerates.

Due to many physical phenomena involved in nanoparticle jets, the existing numerical tool available were not suitable to model the nanoparticle jet. Therefore, the second part of the work consisted in the development of a numerical tool able to predict the nanoparticle behavior in air by modelling each physical phenomenon chosen in the first part of work. The numerical tool was developed in a CFD framework with *Code_Saturne* which had a good accuracy for the microparticle jet modelling. The drag on agglomerates modelling was validated with a configuration of free fall agglomerates. In the homogeneous isotropic turbulence configuration, a critical agglomerate diameter is obtained where the fluid turbulence is not strong enough to break the agglomerates. The critical agglomerate diameter was found in relation with the fluid turbulence by a power law proposed in the present study. In a configuration of a jet, the simulation results have shown that the agglomerate breakage is strong near the nozzle where the turbulent fluctuations are strong. When the agglomerates are far from the nozzle, the turbulent decreases and the agglomerate breakage decreases.

Due to the agglomerate porosity, the collision probability for spherical particles in the literature cannot be applied for the agglomerates case. Most of studies in the literature used a very expensive computation method in order to model the agglomerate collision. Unfortunately, those numerical methods cannot be used in the industrial application. In the present study, a simple model to calculate the collision probability for agglomerates was proposed. The agglomerate collision probability model takes into account the agglomerate properties as the fractal dimension, the primary particles size in the computation of the collision probability. In order to reduce the computational time, other studies can use the new agglomerate collision probability model in the agglomerates collision modelling without simulating the structure of the agglomerates.

The agglomeration modelling is developed in *Code_Saturne*. The numerical results show that in a homogeneous isotropic turbulence configuration, when the turbulence increases, the relative velocity between agglomerate increases and the collision increases. However, the interparticle force is not strong enough to adhere the agglomerates in collision, therefore the agglomeration decreases.

An accident leakage of a conveying pipe occurred in Blanzy, France in 2012 but there were no studies realized in order to estimate the distance effect of this accident case. Therefore, the third part of the work investigated the simulation of this accident case. *Code_Saturne* is used to simulate the field near the release. The results showed that that breakage was not observed and the agglomeration has a great influence on the agglomerate size and number concentration. *Code_Saturne* results are used as the input data for an atmospheric modelling tool, ADMS. The accidental study case showed the application of the numerical tool developed and its capability to be coupled with another numerical tool.

Future work

A wide variety of subjects is analyzed in the present study. We synthesize here the possible tracks in order to improve the modelling of the physical phenomena related to nanoparticle dispersion in the air.

Concerning the numerical simulation of the accident pipe leakage in Blanzy by *Code_Saturne*, a more detailed CFD study could be performed. It would be interesting to run the simulation with black carbon properties in order to see the influence of nanoparticle properties on main physical mechanisms: agglomeration, agglomerate breakage, sedimentation. The wall of the building where the leakage occurs can be taken into account in the boundary conditions of the numerical simulation. The presence of the wall may influence the wind field and therefore the particle dispersion. A fine post-processing of the results should show the region of the release where the highest agglomeration rate occurs. The new agglomerate collision probability model presented in Chap. 3.3 is not used in the numerical simulation of the accident pipe leakage. A further study should investigate on the influence of the agglomerate collision probability on the particle distribution function exiting the domain in *Code_Saturne*. At INERIS, prelimary experiments of microparticle jet are realized and presented in the Annex C.

A comparison between the experimental data and the numerical simulation should be realized for this configuration.

In the modelling of the agglomerate strength, the capillary force could be added in the future if the model is available in the literature. The capillary force would increase the agglomerate strength and therefore decreases the agglomerate breakage. Regarding the modelling of the fragmentation distribution function, a more appropriate function should be used than an uniform distribution function. This function should depend on the agglomerate fractal dimension as shown by the experiment in the literature. Concerning the collision probability for agglomerates, additional physical phenomena need to be considered in the collision modelling such as the Brownian motion and the flow around the agglomerate. The experiment data for the physical phenomena of breakage and agglomeration of agglomerate in a turbulent jet is not sufficient to well understood for those physical phenomena. Once the experimental analysis of microparticle jet, presented in the Annex C, have a good agreement with the numerical simulation, an experiment study of each physical phenomena as the breakage or the agglomeration in a jet can be performed. On the other hand, the experiment of nanoparticle jet can also be realized by changing the powder type, the instrument measurement appropriated for nanoparticles. The experiment of nanoparticle jet should be realized in the laboratory scale for the control of the dispersed nanoparticles.

In the future, the present study could be used to predict the consequences of an accidental release. This requires that toxicity data are available for short term exposure. In the meantime, it can be used to better understand and interpret experimental results. The model was developed to simulate accidental massive releases but it could be adapted for other scenario and purposes: possible adaptation of the model to assess the behavior of nanoparticles at a workplace, simulating continuous release from stack, prediction of the fate of nanoparticles in the air following a fire, assessment of dispersibility of a powder containing nano-objects, simulating agglomeration mechanisms in experimental set-ups (such as the 20 L sphere, Hartman tube, etc), simulating the behavior of particles in measurement devices (agglomeration inside the pipe leading to a particle counter).

Bibliography

[1] ISO/TS 80004-1. Nanotechnologies - vocabulaire. 2015.

[2] Hamed Abbasfard, Geoffrey Evans, and Roberto Moreno-Atanasio. Effect of van der Waals force cut-off distance on adhesive collision parameters in DEM simulation. *Powder Technology*, 299:9–18, October 2016.

[3] M. Alletto and M. Breuer. One-way, two-way and four-way coupled LES predictions of a particle-laden turbulent flow at high mass loading downstream of a confined bluff body. *International Journal of Multiphase Flow*, 45:70–90, October 2012.

[4] Laure Alloul-Marmor. *Réentrainement par ecoulement d'air d'une contamination particulaire deposée sur une surface.* PhD thesis, Université Paris XII, 2002.

[5] N. Almohammed and M. Breuer. Modeling and simulation of agglomeration in turbulent particle-laden flows: A comparison between energy-based and momentum-based agglomeration models. *Powder Technology*, January 2016.

[6] Yasmine Ammar, Abdel Dehbi, and Michael W. Reeks. Break-Up of Aerosol Agglomerates in Highly Turbulent Gas Flow. *Flow, Turbulence and Combustion*, 89(3):465–489, September 2012.

[7] Renaud Ansart, Alain De Ryck, and John A Dodds. Dust emission in powder handling: free falling particle plume characterisation. *Chemical Engineering Journal*, 152(2-3):415–420, 2009.

[8] Sergiy Antonyuk, Manoj Khanal, Jürgen Tomas, Stefan Heinrich, and Lothar Mörl. Impact breakage of spherical granules: Experimental study and DEM simulation. *Chemical Engineering and Processing: Process Intensification*, 45(10):838–856, October 2006.

[9] Boris V. Balakin, Guzel Shamsutdinova, and Pawel Kosinski. Agglomeration of solid particles by liquid bridge flocculants: Pragmatic modelling. *Chemical Engineering Science*, 122:173–181, January 2015.

[10] Christian E.H. Beaudrie, Milind Kandlikar, and Gurumurthy Ramachandran. Chapter 5 - using expert judgment for risk assessment. In Gurumurthy Ramachandran, editor, *Assessing Nanoparticle Risks to Human Health (Second Edition)*, pages 91 – 119. William Andrew Publishing, Oxford, second edition, 2016.

[11] L. Boguslawski and Cz. O. Popiel. Flow structure of the free round turbulent jet in the initial region. *Journal of Fluid Mechanics*, 90(03):531, February 1979.

[12] M. Breuer and N. Almohammed. Modeling and simulation of particle agglomeration in turbulent flows using a hard-sphere model with deterministic collision detection and enhanced structure models. *International Journal of Multiphase Flow*, 73:171–206, July 2015.

[13] H. C. Brinkman. On the permeability of media consisting of closely packed porous particles. *Applied Scientific Research*, 1(1):81–86, December 1949.

[14] James S. Brown, Kirby L. Zeman, and William D. Bennett. Ultrafine Particle Deposition and Clearance in the Healthy and Obstructed Lung. *American Journal of Respiratory and Critical Care Medicine*, 166(9):1240–1247, November 2002.

[15] G. Calvert, M. Ghadiri, and R. Tweedie. Aerodynamic dispersion of cohesive powders: A review of understanding and technology. *Advanced Powder Technology*, 20(1):4–16, January 2009.

[16] Chloé Caumont-Prim, Jérôme Yon, Alexis Coppalle, François-Xavier Ouf, and Kuan Fang Ren. Measurement of aggregates' size distribution by angular light scattering. *Journal of Quantitative Spectroscopy and Radiative Transfer*, 126:140–149, September 2013.

[17] Sydney Chapman and T. G. Cowling. *The mathematical theory of non-uniform gases: an account of the kinetic theory of viscosity, thermal conduction and diffusion in gases*. Cambridge mathematical library. Cambridge Univ. Press, Cambridge, 3. ed., transferred to digital printing edition, 1998. OCLC: 246384286.

[18] A. L. Chernyakov. Hydrodynamic drag of a fractal cluster. *Journal of Experimental and Theoretical Physics*, 93(4):771–776, October 2001.

[19] R Clift and WH Gauvin. Motion of particles in turbulent gas streams. *British Chemical Engineering*, 16(2-3):229, 1971.

[20] C. Coufort, D. Bouyer, and A. Liné. Flocculation related to local hydrodynamics in a Taylor–Couette reactor and in a jar. *Chemical Engineering Science*, 60(8-9):2179–2192, April 2005.

[21] C.A. Coulaloglou and L.L. Tavlarides. Description of interaction processes in agitated liquid-liquid dispersions. *Chemical Engineering Science*, 32(11):1289–1297, January 1977.

[22] Michael A. Delichatsios and Ronald F. Probstein. The Effect of Coalescence on the Average Drop Size in Liquid-Liquid Dispersions. *Industrial & Engineering Chemistry Fundamentals*, 15(2):134–138, May 1976.

[23] M. Devilliers. *Modélisation et simulation numérique de la dynamique des nanoparticules appliquée aux atmosphères libres et confinés*. PhD thesis, Université Paris-Est, 2012.

[24] Colin A. J. Dick, David M. Brown, Ken Donaldson, and Vicki Stone. The role of free radicals in the toxic and inflammatory effects of four different ultrafine particle types. *Inhalation Toxicology*, 15(1):39–52, 2003. PMID: 12476359.

[25] M. Dietzel, M. Ernst, and M. Sommerfeld. Application of the Lattice-Boltzmann Method for Particle-laden Flows: Point-particles and Fully Resolved Particles. *Flow, Turbulence and Combustion*, January 2016.

[26] Mathias Dietzel and Martin Sommerfeld. Numerical calculation of flow resistance for agglomerates with different morphology by the Lattice–Boltzmann Method. *Powder Technology*, 250:122–137, December 2013.

[27] Yaobo Ding, Burkhard Stahlmecke, Araceli Sánchez Jiménez, Ilse L. Tuinman, Heinz Kaminski, Thomas A. J. Kuhlbusch, Martie van Tongeren, and Michael Riediker. Dustiness and Deagglomeration Testing: Interlaboratory Comparison of Systems for Nanoparticle Powders. *Aerosol Science and Technology*, pages 17–28, November 2015.

[28] Kevin E Driscoll. Role of inflammation in the development of rat lung tumors in response to chronic particle exposure. *Inhalation toxicology*, 8:139–153, 1996.

[29] Maximilian L. Eggersdorfer and Sotiris E. Pratsinis. Agglomerates and aggregates of nanoparticles made in the gas phase. *Advanced Powder Technology*, 25(1):71–90, January 2014.

[30] S. Elghobashi, T. Abou-Arab, M. Rizk, and A. Mostafa. Prediction of the particle-laden jet with a two-equation turbulence model. *International Journal of Multiphase Flow*, 10(6):697–710, December 1984.

[31] Mark E. Erupe, David R. Benson, Jingmin Li, Li-Hao Young, Bart Verheggen, Mohammed Al-Refai, Omar Tahboub, Victoria Cunningham, Flavia Frimpong, Albert A. Viggiano, and Shan-Hu Lee. Correlation of aerosol nucleation rate with sulfuric acid and ammonia in Kent, Ohio: An atmospheric observation. *Journal of Geophysical Research*, 115(D23), December 2010.

[32] Pascal Fede, Olivier Simonin, and Philippe Villedieu. Monte-Carlo simulation of colliding particles or coalescing droplets transported by a turbulent flow in the framework of a joint fluid–particle pdf approach. *International Journal of Multiphase Flow*, 74:165–183, September 2015.

[33] S R Forrest and T A Witten Jr. Long-range correlations in smoke-particle aggregates. *Journal of Physics A: Mathematical and General*, 12(5):L109, 1979.

[34] Sheldon Kay Friedlander. Smoke, dust and haze: Fundamentals of aerosol behavior. *New York, Wiley-Interscience, 1977. 333 p.*, 1977.

[35] Sonja Froeschke, Stefanie Kohler, Alfred P. Weber, and Gerhard Kasper. Impact fragmentation of nanoparticle agglomerates. *Journal of Aerosol Science*, 34(3):275–287, March 2003.

[36] Jonghwu Jung et Dimitri Gidaspow. Fluidization of nano-siez paticles. *Journal of nanoparticle Research 4: 483-497*, 2002.

[37] R. A. Gore and C. T. Crowe. Effect of particle size on modulating turbulent intensity. *International Journal of Multiphase Flow*, 15(2):279 – 285, 1989.

[38] AD Gosman and E Ioannides. Aspects of computer simulation of liquid-fuelled combustors. aiaa 19th aerospace sciences meeting. *Saint-Louis, Missouri (January 12–15, 1981)*, 1981.

[39] Eirini Goudeli, Maximilian L. Eggersdorfer, and Sotiris E. Pratsinis. Coagulation–Agglomeration of Fractal-like Particles: Structure and Self-Preserving Size Distribution. *Langmuir*, 31(4):1320–1327, February 2015.

[40] Romain Guichard. *Dynamique d'un aérosol de Nanoparticules - Modélisation de la coagulation et du transport d'agrégats*. PhD thesis, Université de Lorraine, 2013.

[41] E. Gutmark and I. Wygnanski. The planar turbulent jet. *Journal of Fluid Mechanics*, 73(03):465, February 1976.

[42] K. Hadinoto, E. N. Jones, C. Yurteri, and J. S. Curtis. Reynolds number dependence of gas-phase turbulence in gas–particle flows. *International Journal of Multiphase Flow*, 31(4):416 – 434, 2005.

[43] Frank Hamelmann and Eberhard Schmidt. Methods of estimating the dustiness of industrial powders–a review. *KONA Powder and Particle Journal*, 21:7–18, 2003.

[44] Steven R Hanna, Gary A Briggs, and Rayford P Hosker Jr. Handbook on atmospheric diffusion. Technical report, National Oceanic and Atmospheric Administration, Oak Ridge, TN (USA). Atmospheric Turbulence and Diffusion Lab., 1982.

[45] John Happel. Viscous flow in multiparticle systems: slow motion of fluids relative to beds of spherical particles. *AIChE Journal*, 4(2):197–201, 1958.

[46] W Keith Hastings. Monte Carlo sampling methods using Markov chains and their applications. *Biometrika*, 57(1):97–109, 1970.

[47] Hans J. Herrmann, Falk K. Wittel, and Ferenc Kun. Fragmentation. *Physica A: Statistical Mechanics and its Applications*, 371(1):59–66, November 2006.

[48] Rainer Hiller and Friedrich Löffler. Der Einfluß von Partikelstoß und Partikel-Haftung auf die Abscheidung von Partikeln in Faserfiltern: Der Einfluß von Partikelstoß und Partikel-Haftung auf die Abscheidung von Partikeln in Faserfiltern. *Chemie Ingenieur Technik*, 52(4):352–353, 1980.

[49] William C. Hinds. *Aerosol technology - Properties, behavior, and measuremet of aiborne particles*. 2nd edition, 1999.

[50] J. Huang, S. Xu, H. Yi, and S. Hu. Size effect on the compression breakage strengths of glass particles. *Powder Technology*, 268:86–94, December 2014.

[51] Nelson Ibaseta and Béatrice Biscans. Fractal dimension of fumed silica: Comparison of light scattering and electron microscope methods. *Powder Technology*, 203(2):206–210, November 2010.

[52] Nelson Ibaseta, Eric Climent, and Béatrice Biscans. SFGP 2007 - Ultrafine Aerosol Generation from Free Falling Nanopowders: Experiments and Numerical Modelling. *International Journal of Chemical Reactor Engineering*, 6(1), January 2008.

[53] Klaus Iglberger, Nils Thürey, and Ulrich Rüde. Simulation of moving particles in 3d with the Lattice Boltzmann method. *Computers & Mathematics with Applications*, 55(7):1461–1468, April 2008.

[54] M. Ihalainen, T. Lind, J. Ruusunen, P. Tiitta, A. Lähde, T. Torvela, and J. Jokiniemi. Experimental study on bounce of submicron agglomerates upon inertial impaction. *Powder Technology*, 268:203–209, December 2014.

[55] T Kapias and R Griffiths. Accidental releases of titanium tetrachloride (TiCl) in the context of major hazards spill behaviour using REACTPOOL. *Journal of Hazardous Materials*, 119(1-3):41–52, March 2005.

[56] Catharine A. Kastner, Andreas Braumann, Peter L.W. Man, Sebastian Mosbach, George P.E. Brownbridge, Jethro Akroyd, Markus Kraft, and Chrismono Himawan. Bayesian parameter estimation for a jet-milling model using Metropolis–Hastings and Wang–Landau sampling. *Chemical Engineering Science*, 89:244–257, February 2013.

[57] Albert S. Kim and Keith D. Stolzenbach. The Permeability of Synthetic Fractal Aggregates with Realistic Three-Dimensional Structure. *Journal of Colloid and Interface Science*, 253(2):315–328, September 2002.

[58] Albert S. Kim and Rong Yuan. Hydrodynamics of an ideal aggregate with quadratically increasing permeability. *Journal of Colloid and Interface Science*, 285(2):627–633, May 2005.

[59] P. Kosinski, A. Kosinska, and A.C. Hoffmann. Simulation of solid particles behaviour in a driven cavity flow. *Powder Technology*, 191(3):327–339, April 2009.

[60] Pawel Kosinski and Alex C. Hoffmann. An extension of the hard-sphere particle–particle collision model to study agglomeration. *Chemical Engineering Science*, 65(10):3231–3239, May 2010.

[61] C. Kuang, P. H. McMurry, A. V. McCormick, and F. L. Eisele. Dependence of nucleation rates on sulfuric acid vapor concentration in diverse atmospheric locations. *Journal of Geophysical Research*, 113(D10), May 2008.

[62] Pramod Kulkarni, Paul A Baron, and Klaus Willeke. *Aerosol measurement: principles, techniques, and applications*. John Wiley & Sons, 2011.

[63] Markku Kulmala and Veli-Matti Kerminen. On the formation and growth of atmospheric nanoparticles. *Atmospheric Research*, 90(2-4):132–150, November 2008.

[64] Prashant Kumar, Alan Robins, Sotiris Vardoulakis, and Rex Britter. A review of the characteristics of nanoparticles in the urban atmosphere and the prospects for developing regulatory controls. *Atmospheric Environment*, 44(39):5035–5052, December 2010.

[65] KA Kusters. On aggregation of small particles in agitated vessels. *PhD in Chemical Engineering, Technische Universiteit Eindhoven*, 1991.

[66] Karl A. Kusters, Johan G. Wijers, and Dirk Thoenes. Aggregation kinetics of small particles in agitated vessels. *Chemical Engineering Science*, 52(1):107–121, January 1997.

[67] Daniele L. Marchisio, R. Dennis Vigil, and Rodney O. Fox. Implementation of the quadrature method of moments in CFD codes for aggregation–breakage problems. *Chemical Engineering Science*, 58(15):3337–3351, August 2003.

[68] Cédric Laborde-Boutet, Faiçal Larachi, Nicolas Dromard, Olivier Delsart, and Daniel Schweich. CFD simulation of bubble column flows: Investigations on turbulence models in RANS approach. *Chemical Engineering Science*, 64(21):4399–4413, November 2009.

[69] B.E. Launder and D.B. Spalding. The numerical computation of turbulent flows. *Computer Methods in Applied Mechanics and Engineering*, 3(2):269–289, March 1974.

[70] Xiaoyan Li and Bruce E. Logan. Collision Frequencies of Fractal Aggregates with Small Particles by Differential Sedimentation. *Environmental Science & Technology*, 31(4):1229–1236, April 1997.

[71] Yixiang Liao and Dirk Lucas. A literature review on mechanisms and models for the coalescence process of fluid particles. *Chemical Engineering Science*, 65(10):2851–2864, May 2010.

[72] Maryanne G. Boundy Fierdrich Löffler Marc A.E. Plinky, david Leith. Dust generation from handling powders in industry. *Am. Ind. Hyg. Assog. J. 55251-257*, 1995.

[73] Clara Martineau. *Modélisation stochastique du dépôt de particule colloïdales transportées par des écoulements isothermes et non isothermes*. PhD thesis, Université de Lorraine, 2013.

[74] F. Martínez-López, M.A. Cabrerizo-Vıílchez, and R. Hidalgo-Álvarez. An improved method to estimate the fractal dimension of physical fractals based on the Hausdorff definition. *Physica A: Statistical Mechanics and its Applications*, 298(3-4):387–399, September 2001.

[75] Jacob H. Masliyah, Graham Neale, K. Malysa, and Theodorus G.M. Van De Ven. Creeping flow over a composite sphere: Solid core with porous shell. *Chemical Engineering Science*, 42(2):245–253, 1987.

[76] K. Matsumoto and A. Suganuma. Settling velocity of a permeable model floc. *Chemical Engineering Science*, 32(4):445–447, 1977.

[77] S. Matsusaka, H. Maruyama, T. Matsuyama, and M. Ghadiri. Triboelectric charging of powders: A review. *Chemical Engineering Science*, 65(22):5781–5807, November 2010.

[78] Andrew D Maynard. Nanotechnology: assessing the risks. *Nano Today*, 1(2):22–33, 2006.

[79] Michael A McCawley, Michael S Kent, and Michael T Berakis. Ultrafine beryllium number concentration as a possible metric for chronic beryllium disease risk. *Applied Occupational and Environmental Hygiene*, 16(5):631–638, 2001.

[80] Robert McGraw. Description of Aerosol Dynamics by the Quadrature Method of Moments. *Aerosol Science and Technology*, 27(2):255–265, January 1997.

[81] David Mills. *Pneumatic conveying design guide*. Butterworth-Heinemann, 2003.

[82] Jean-Pierre Minier. On Lagrangian stochastic methods for turbulent polydisperse two-phase reactive flows. *Progress in Energy and Combustion Science*, 50:1–62, October 2015.

[83] Jean-Pierre Minier and Eric Peirano. The pdf approach to turbulent polydispersed two-phase flows. *Physics Reports*, 352(1-3):1–214, October 2001.

[84] B.K Mishra and C Thornton. Impact breakage of particle agglomerates. *International Journal of Mineral Processing*, 61(4):225–239, April 2001.

[85] R. Moreno-Atanasio and M. Ghadiri. Mechanistic analysis and computer simulation of impact breakage of agglomerates: Effect of surface energy. *Chemical Engineering Science*, 61(8):2476–2481, April 2006.

[86] Philippe Nerisson. *Modélisation du transfert des aérosols dans un local ventilé*. PhD thesis, Institut National Polytechnique de Toulouse, 2009.

[87] Kiyoshi Nogi, Makio Naito, and Toyokazu Yokoyama. *Nanoparticle technology handbook*. Elsevier, 2012.

[88] B. Oesterle and A. Petitjean. Simulation of particle-to-particle interactions in gas solid flows. *International Journal of Multiphase Flow*, 19(1):199 – 211, 1993.

[89] C. Oh and C.M. Sorensen. The Effect of Overlap between Monomers on the Determination of Fractal Cluster Morphology. *Journal of Colloid and Interface Science*, 193(1):17–25, September 1997.

[90] Frank Pasquill. The estimation of the dispersion of windborne material. *Meteorol. Magazine*, 90:33–49, 1961.

[91] Lus M. Portela and Ren V. A. Oliemans. Eulerian-Lagrangian DNS/LES of particle-turbulence interactions in wall-bounded flows. *International Journal for Numerical Methods in Fluids*, 43(9):1045–1065, November 2003.

[92] Walter Roedel. Measurement of sulfuric acid saturation vapor pressure; Implications for aerosol formation by heteromolecular nucleation. *Journal of Aerosol Science*, 10(4):375–386, January 1979.

[93] Debashish Saha, Matthaus U. Babler, Markus Holzner, Miroslav Soos, Beat Lüthi, Alex Liberzon, and Wolfgang Kinzelbach. Breakup of Finite-Size Colloidal Aggregates in Turbulent Flow Investigated by Three-Dimensional (3d) Particle Tracking Velocimetry. *Langmuir*, 32(1):55–65, January 2016.

[94] A.D Salman, G.K Reynolds, J.S Fu, Y.S Cheong, C.A Biggs, M.J Adams, D.A Gorham, J Lukenics, and M.J Hounslow. Descriptive classification of the impact failure modes of spherical particles. *Powder Technology*, 143-144:19–30, June 2004.

[95] N. Sator and H. Hietala. Damage in impact fragmentation. *International Journal of Fracture*, 163(1-2):101–108, May 2010.

[96] N. Sator, S. Mechkov, and F. Sausset. Generic behaviours in impact fragmentation. *EPL (Europhysics Letters)*, 81(4):44002, February 2008.

[97] L. Schiller and Z. Naumann. A drag coefficient correlation. *Verein Deutscher Ingenieure*, 77,318, 1935.

[98] George A Sehmel. Particle and gas dry deposition: a review. *Atmospheric Environment (1967)*, 14(9):983–1011, 1980.

[99] John H Seinfeld and Spyros N Pandis. *Atmospheric chemistry and physics: from air pollution to climate change*. John Wiley & Sons, 2006.

[100] Martin Seipenbusch, Petya Toneva, Wolfgang Peukert, and Alfred P. Weber. Impact Fragmentation of Metal Nanoparticle Agglomerates. *Particle & Particle Systems Characterization*, 24(3):193–200, September 2007.

[101] J.P.K. Seville, C.D. Willett, and P.C. Knight. Interparticle forces in fluidisation: a review. *Powder Technology*, 113(3):261–268, December 2000.

[102] O. Simonin, E. Deutsch, and J. P. Minier. Eulerian Prediction of the Fluid/-Particle Correlated Motion in Turbulent Two-Phase Flows. In R. Moreau and F. T. M. Nieuwstadt, editors, *Advances in Turbulence IV*, volume 18, pages 275–283. Springer Netherlands, Dordrecht, 1993.

[103] S.J.R. Simons. Modelling of agglomerating systems: from spheres to fractals. *Powder Technology*, 87(1):29–41, April 1996.

[104] Martin Sommerfeld. Validation of a stochastic Lagrangian modelling approach for inter-particle collisions in homogeneous isotropic turbulence. *International Journal of Multiphase Flow*, 27(10):1829–1858, October 2001.

[105] Richard C. Sonntag and William B. Russel. Structure and breakup of flocs subjected to fluid stresses. *Journal of Colloid and Interface Science*, 113(2):399–413, October 1986.

[106] Miroslav Soos, Lyonel Ehrl, Matthäus U. Bäbler, and Massimo Morbidelli. Aggregate Breakup in a Contracting Nozzle. *Langmuir*, 26(1):10–18, January 2010.

[107] C. M. Sorensen. The Mobility of Fractal Aggregates: A Review. *Aerosol Science and Technology*, 45(7):765–779, July 2011.

[108] Christopher M. Sorensen and Gregory C. Roberts. The Prefactor of Fractal Aggregates. *Journal of Colloid and Interface Science*, 186(2):447–452, February 1997.

[109] Burkhard Stahlmecke, Sandra Wagener, Christof Asbach, Heinz Kaminski, Heinz Fissan, and Thomas A. J. Kuhlbusch. Investigation of airborne nanopowder agglomerate stability in an orifice under various differential pressure conditions. *Journal of Nanoparticle Research*, 11(7):1625–1635, October 2009.

[110] S. L. Sutter. Aerosols Generated By Releases of Pressurized Powders ad Solutios in Static Air. Technical report, Office of Nuclear Regulatory Research, 1983.

[111] C. Thornton, K. K. Yin, and M. J. Adams. Numerical simulation of the impact fracture and fragmentation of agglomerates. *Journal of Physics D: Applied Physics*, 29(2):424, 1996.

[112] Zhenbo Tong, Wenqi Zhong, Aibing Yu, Hak-Kim Chan, and Runyu Yang. CFD–DEM investigation of the effect of agglomerate–agglomerate collision on dry powder aerosolisation. *Journal of Aerosol Science*, 92:109–121, February 2016.

[113] D Bruce Turner. Atmospheric dispersion modeling. a critical review. *J. Air Pollut. Control Assoc.*, 29(5), 1979.

[114] P. Vainshtein and M. Shapiro. Porous agglomerates in the general linear flow field. *Journal of Colloid and Interface Science*, 298(1):183–191, June 2006.

[115] P. Vainshtein, M. Shapiro, and C. Gutfinger. Mobility of permeable aggregates: effects of shape and porosity. *Journal of Aerosol Science*, 35(3):383–404, March 2004.

[116] Marina E Vance, Todd Kuiken, Eric P Vejerano, Sean P McGinnis, Michael F Hochella, David Rejeski, and Matthew S Hull. Nanotechnology in the real world: Redeveloping the nanomaterial consumer products inventory. *Beilstein Journal of Nanotechnology*, 6:1769–1780, August 2015.

[117] Marco Vanni. Creeping flow over spherical permeable aggregates. *Chemical Engineering Science*, 55(3):685–698, February 2000.

[118] Marco Vanni. Accurate modelling of flow induced stresses in rigid colloidal aggregates. *Computer Physics Communications*, 192:70–90, July 2015.

[119] Philippe Villedieu and Jouke Hylkema. Une méthode particulaire aléatoire reposant sur une équation cinétique pour la simulation numérique des sprays denses de gouttelettes liquides. *Comptes Rendus de l'Académie des Sciences - Series I - Mathematics*, 325(3):323–328, August 1997.

[120] Bert Vreman, Bernard J. Geurts, N. G. Deen, J. A. M. Kuipers, and J. G. M. Kuerten. Two- and Four-Way Coupled Euler–Lagrangian Large-Eddy Simulation of Turbulent Particle-Laden Channel Flow. *Flow, Turbulence and Combustion*, 82(1):47–71, January 2009.

[121] Claudius Weiler, Markus Wolkenhauer, Michael Trunk, and Peter Langguth. New model describing the total dispersion of dry powder agglomerates. *Powder Technology*, 203(2):248–253, November 2010.

[122] Robert Wengeler, Alexandra Teleki, Markus Vetter, Sotiris E. Pratsinis, and Hermann Nirschl. High-Pressure Liquid Dispersion and Fragmentation of Flame-Made Silica Agglomerates. *Langmuir*, 22(11):4928–4935, May 2006.

[123] R. Wernet, A.G. Schunck, W. Baumann, H.-R. Paur, and M. Seipenbusch. Quantification of interparticle forces by energy controlled fragmentation analysis. *Journal of Aerosol Science*, 84:14–20, June 2015.

[124] Melissa L. Whitfield Åslund, Heather McShane, Myrna J. Simpson, André J. Simpson, Joann K. Whalen, William H. Hendershot, and Geoffrey I. Sunahara. Earthworm Sublethal Responses to Titanium Dioxide Nanomaterial in Soil Detected by ^{1}H NMR Metabolomics. *Environmental Science & Technology*, 46(2):1111–1118, January 2012.

[125] Peter Wypych, Dave Cook, and Paul Cooper. Controlling dust emissions and explosion hazards in powder handling plants. *Chemical Engineering and Processing: Process Intensification*, 44(2):323–326, 2005.

[126] Feng Xiao, Hui Xu, Xiao-yan Li, and Dongsheng Wang. Modeling particle-size distribution dynamics in a shear-induced breakage process with an improved breakage kernel: Importance of the internal bonds. *Colloids and Surfaces A: Physicochemical and Engineering Aspects*, 468:87–94, March 2015.

[127] C. Xiong and S. K. Friedlander. Morphological properties of atmospheric aerosol aggregates. *Proceedings of the National Academy of Sciences*, 98(21):11851–11856, October 2001.

[128] Anthony K.C. Yeung and Robert Pelton. Micromechanics: A New Approach to Studying the Strength and Breakup of Flocs. *Journal of Colloid and Interface Science*, 184(2):579–585, December 1996.

[129] Robert A Yokel and Robert C MacPhail. Engineered nanomaterials: exposures, hazards, and risk prevention. *Journal of Occupational Medicine and Toxicology*, 6(1):7, 2011.

[130] Mingzhou Yu and Jianzhong Lin. Taylor-expansion moment method for agglomerate coagulation due to Brownian motion in the entire size regime. *Journal of Aerosol Science*, 40(6):549–562, June 2009.

[131] Z. Zhang, C. Kleinstreuer, J.F. Donohue, and C.S. Kim. Comparison of micro- and nano-size particle depositions in a human upper airway model. *Journal of Aerosol Science*, 36(2):211–233, February 2005.

[132] Chao Zhu, Qun Yu, Rajesh N. Dave, and Robert Pfeffer. Gas fluidization characteristics of nanoparticle agglomerates. *AIChE Journal*, 51(2):426–439, February 2005.

Appendices

Appendix A

A.1 Calculation of the standard deviation

The standard deviation between numerical results and model prediction for the collision probability coefficient is calculated as follows

$$\sigma = \sqrt{\frac{\sum_i^{N_{case}} \left(R_{A,i}(simu) - R_{A,i}(model)\right)^2}{N_{case}}} \tag{A.1.1}$$

where $R_{A,i}(simu)$ is the collision probability coefficient from the simulation for case i. $R_{A,i}(model)$ is the collision probability coefficient from the model for the same case i. Each case i corresponds to a collision between an agglomerate and a tracer or a spherical particle or a second agglomerate. N_{case} is the total number of configurations.

A.2 Calculation of the agglomerate velocity after a rebound

The elasticity coefficient is defined in function of the relative velocity between two particles in collision as follows:

$$e_c = \frac{u_{fict}^+ - u_A^+}{u_A^- - u_{fict}^-} \tag{A.2.1}$$

where u_A^+ and u_A^- are the velocity component after and before the collision respectively of the agglomerate. u_{fict}^+ and u_{fict}^- are the velocity component after and before the collision respectively of the fictitious particle. The fictitious particle is considered as stationnary at the collision moment, $u_{fict}^- = 0$. The relation following is deduced:

$$u_{fict}^+ = u_A^- e_c + u_A^+ \tag{A.2.2}$$

The momentum conservation between before and after the collision gives:

$$m_A u_A^+ + m_{fict} u_{fict}^+ = m_A u_A^- + m_{fict} u_{fict}^- \tag{A.2.3}$$

where m_A and m_{fict} are respectively the agglomerate mass and the fictitious particle mass.

Replacing Eq. (A.2.2) in Eq. (A.2.3) and $u_{fict}^{-} = 0$, we obtain:

$$m_A u_A^+ = m_A u_A^- - m_{fict}(u_A^- e_c + u_A^+) \tag{A.2.4}$$

By arranging the terms, the agglomerate velocity after the rebound is calculated as follows:

$$\mathbf{u}_A^+ = \mathbf{u}_A^- \left(\frac{m_A - m_{fict} e_c}{m_{A1} + m_{fict}} \right) \tag{A.2.5}$$

Appendix B

Evaluation of Code_Saturne v4.0 in a configuration of micro particles jet

B.1 Experimental configuration

The experimental data is from Hadinoto et al., [42]. The particle laden gas is injected from the orifice of diameter of 14.2 mm into a test chamber. The test chamber dimension cross section is 470 mm x 470 mm. The length of the chamber is more than 1000 mm but in this evaluation case, the length is considered as 1000 mm. Spherical glass bead particles are considered. The particles velocity is measured by a LPA/PDA (Anemometry laser Doppler). In order to measure the gas velocity, very small particles diameter lower than 10 μm are injected and their velocities are assumed to be equal to the gas velocity. Figure 67 shows the experimental configuration.

Four configuration cases were considered in the study:

1. Only the gas phase (single-phase flow)
2. Two-phase flow with monodisperse particles of diameter of 25 μm
3. Two-phase flow with monodisperse particles of diameter of 70 μm
4. Two-phase flow with bidisperse particles of diameter of 25 μm and 70 μm

Figure 68 shows the mearement profile of the velocity of gas and particulate phases for four configuration cases.

B.2 Description of the numerical simulations

Figure 69 shows the mesh used in the present simulation. The mesh has a dimension of 470 mm $\times$ 470 mm $\times$ 1000 mm with 57780 cells.

The models used in Code_Saturne are as follows

— k-ε standard model

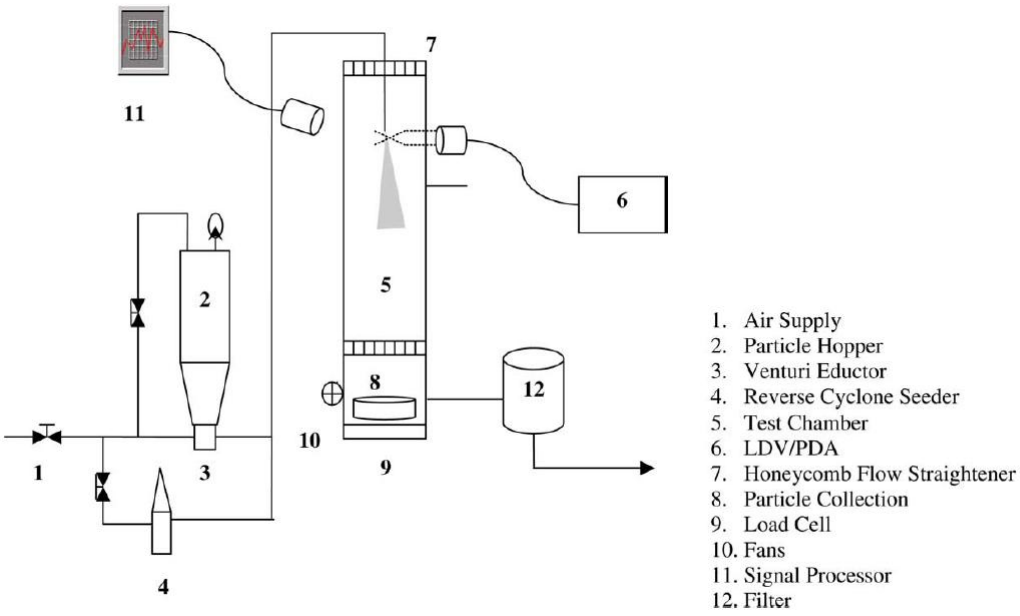

Figure 67 – Schematic representation of the experiment. [42].

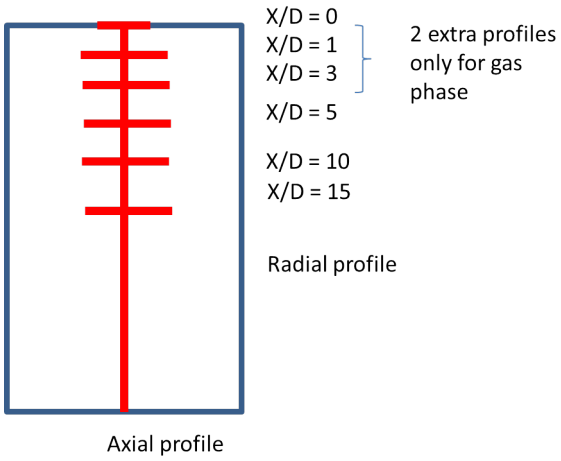

Figure 68 – Measurement profile of the velocity of gas and particule phases for four configuration cases.

— Schiller & Newmann drag model
— 2-way coupling
— Dispersion model of Minier et al., [83].

The volume fraction of the particulate phase is based on the ratio of the particle mass flow rate to the gas mass flow rate measured in experiments. In Code_Saturne, the number of parcels and the statistical weight of each parcel are determined from the

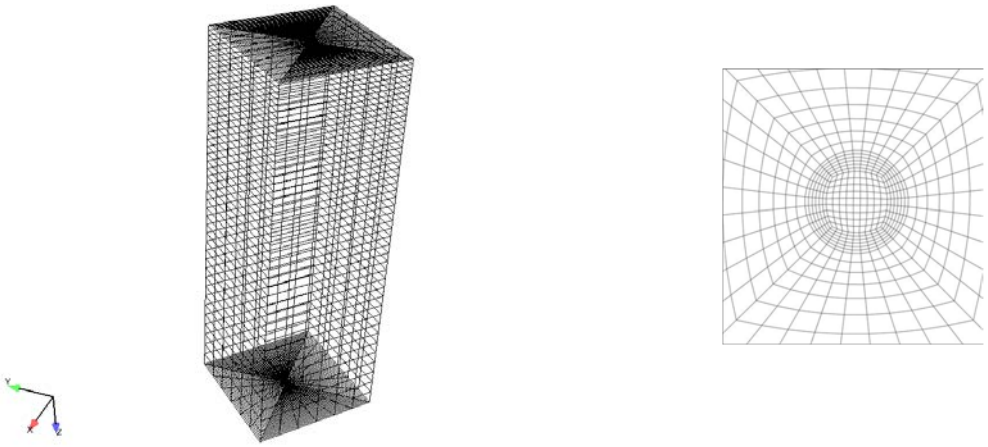

Figure 69 – Mesh used in numerical simulation.

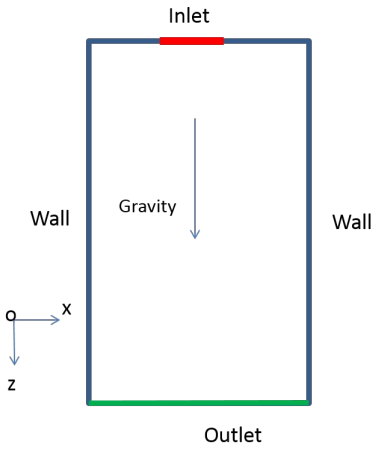

Figure 70 – Boundary conditions in the numerical simulation

volume fraction of experimental data. The time step is $\delta t = 0.001$ s.

- For monodisperse particle of $d_p = 25\ \mu m$: 600 parcels injected/iteration with the statistical weight of $w_p = 225$
- For monodisperse particle of $d_p = 70\ \mu m$: 300 parcels injected/iteration with the statistical weight of $w_p = 20$
- For the case of bidisperse particle with $d_p = 25\ \mu m$ and $70\ \mu m$: 300 parcels injected of $d_p = 25\ \mu m$/iteration with the statistical weight of $w_p = 20$ and 300 parcels injected of $d_p = 70\ \mu m$/iteration with the statistical weight of $w_p = 10$

B.3 Numerical results

B.3.1 Single-phase flow

Figure 71 shows the steady field of the pressure and the velocity component in z-direction of the gas phase.

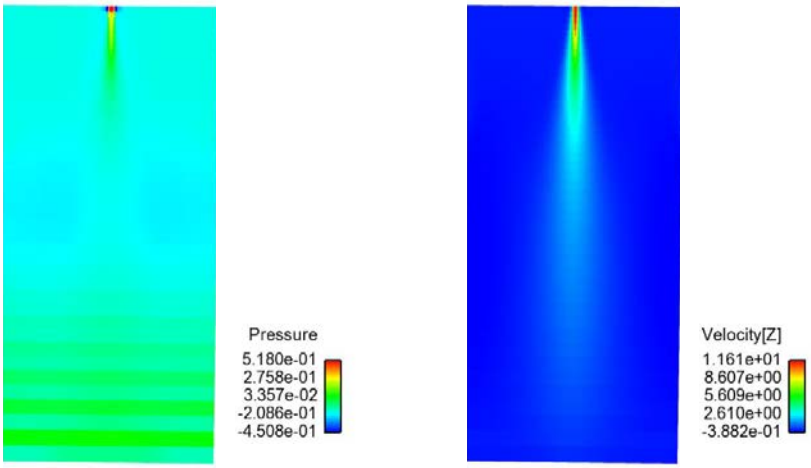

(a) (b)

Figure 71 – Steady field of the pressure (left) and the velocity component in the z-direction of the gas phase

Figure 72 shows the comparison between the results from the numerical simulation and the experimental data. There are no major difference between the experimenation and the numerical results. Far from the orifice, the difference becomes more significant.

B.3.2 Monodisperse case with 25 μm particles

Figure 73 shows the particle dispersion at different times of the simulation.

Figure 74 shows the comparison between the experiment and the numerical simulation of the gas phase of the case of $d_p = 25\ \mu m$. The gas velocity is underestimated by Code_Saturne compared to the experimental data.

Figure 75 shows the comparison between the results from the experiment and the simulation for the particulate velocity phase. The good evaluation is obtained for the particulate velocity in the jet axis. However, far from the orifice, a difference is observed.

B.3.3 Monodisperse case with 70 μm particles

Figure 76 shows the particle dispersion at different times of the simulation.

Figure 77 shows the comparison between the experiment and the numerical simulation of the gas phase of the case of $d_p = 70\ \mu m$. The gas velocity is underestimated by Code_Saturne compared to the experimental data.

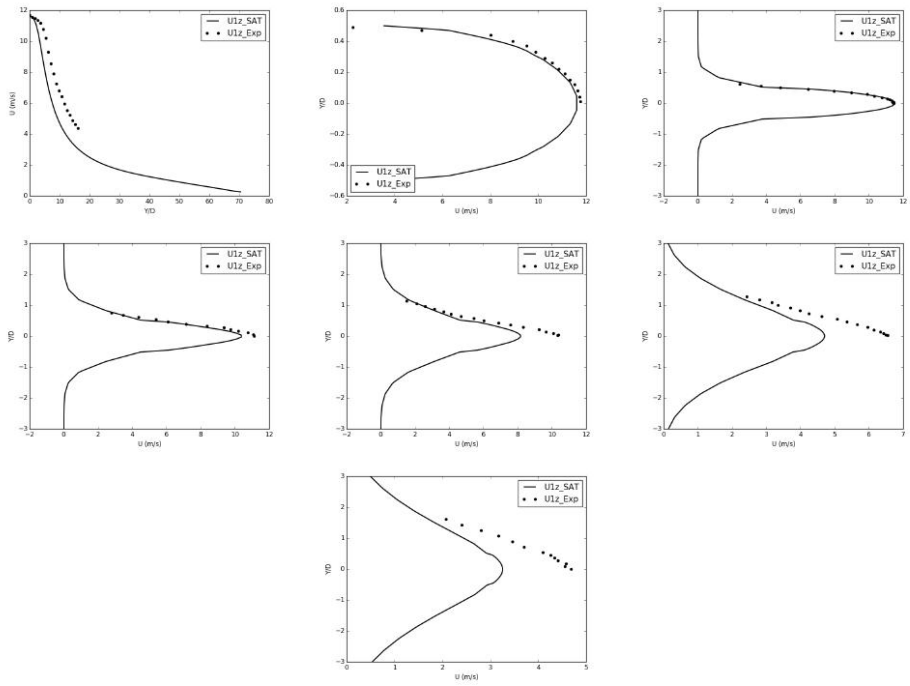

Figure 72 – Comparison of the gas velocity profiles between the experimental data and the results from Code_Saturne

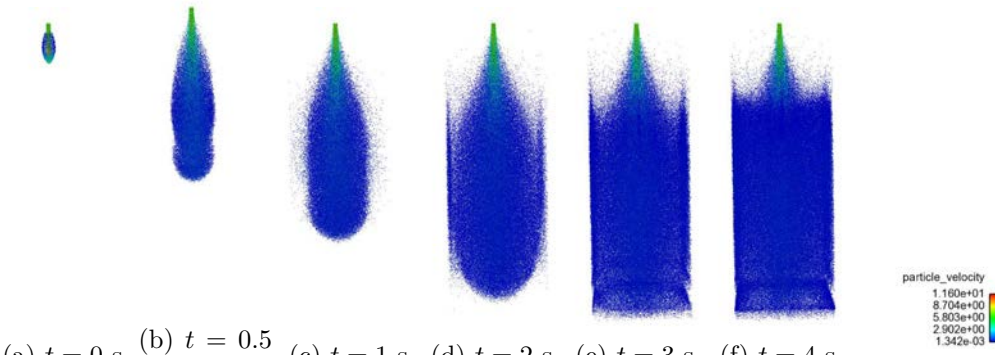

(a) $t = 0$ s (b) $t = 0.5$ s (c) $t = 1$ s (d) $t = 2$ s (e) $t = 3$ s (f) $t = 4$ s

Figure 73 – Results of the particle dispersion of the 25 μm case.

Figure 78 shows the comparison between the results from the experiment and the simulation for the particulate velocity phase. Good agreement is obtained for the particulate velocity in the jet axis. However, far from the orifice, a difference is observed.

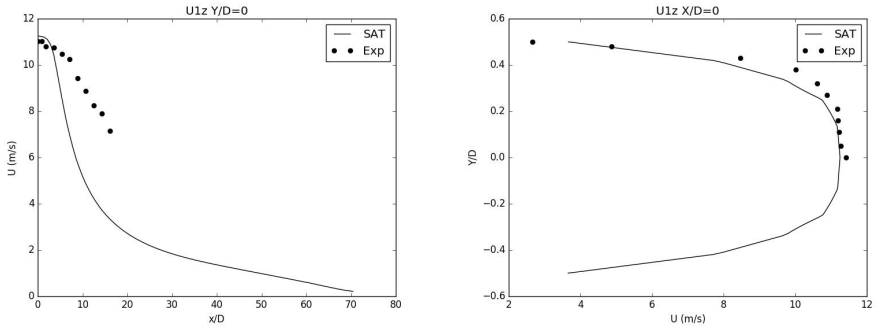

Figure 74 – Comparison between the results from the experiment and the simulation for the gas phase for the case of $d_p = 25\ \mu m$.

B.3.4 Bidisperse case with 25 μm and 70 μm particles

Figure 79 shows the particle dispersion at different times of the simulation. The dispersion behavior of each class is not different from the monodisperse case because the collision between particles is not modelled yet in Code_Saturne.

Figure 80 shows the comparison between the experiment and the numerical simulation of the gas phase for the bidisperse case. The gas velocity is underestimated by Code_Saturne compared to the experimental data.

Figures 81 and 82 show the comparison between the results of particulate velocity phase from the experiment and the simulation for respectively $d_p = 25\ \mu m$ and $d_p = 70\ \mu m$.

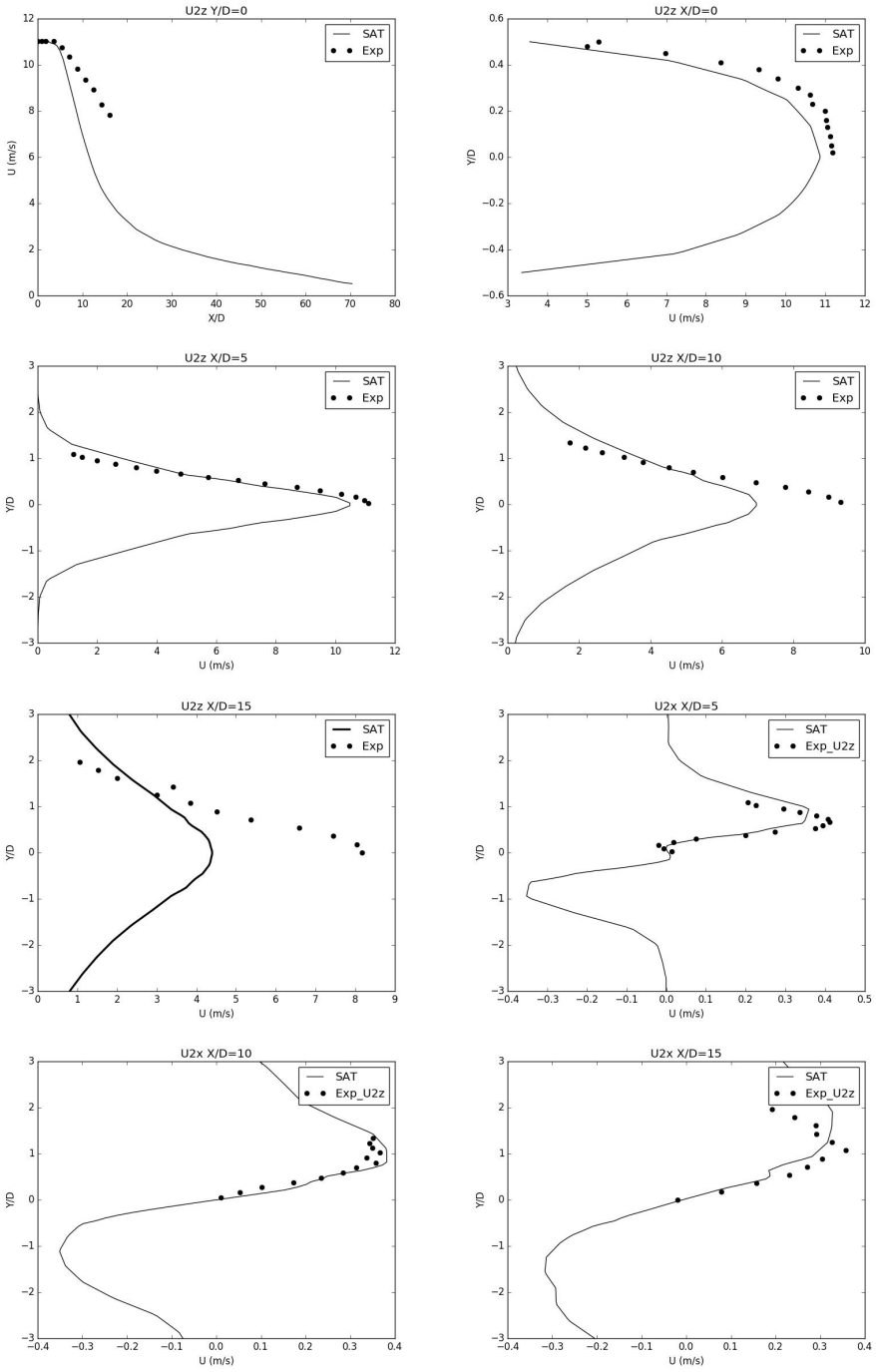

Figure 75 – Comparison between the results of the experiment and the simulation for the particulate velocity for the case of $d_p = 25\ \mu m$.

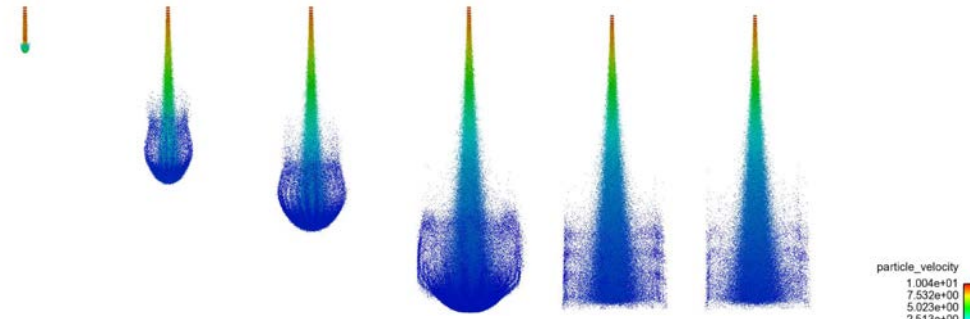

(a) 0s (b) 0.5s (c) 1s (d) 2s (e) 3s (f) 4s

Figure 76 – Results of the particle dispersion of the 70 μm case.

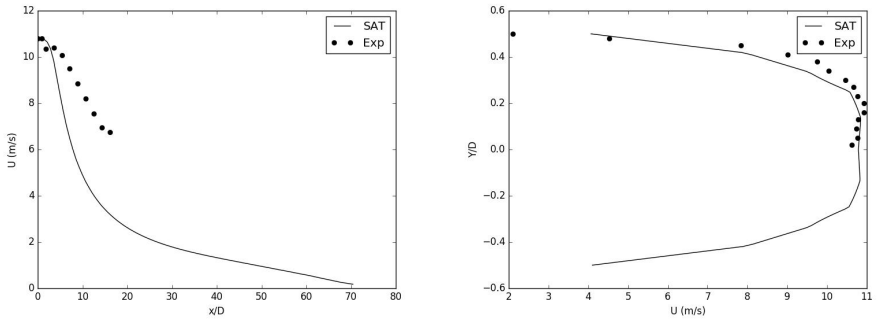

Figure 77 – Comparison between the results from the experiment and the simulation for the gas phase for the case of $d_p = 70$ μm

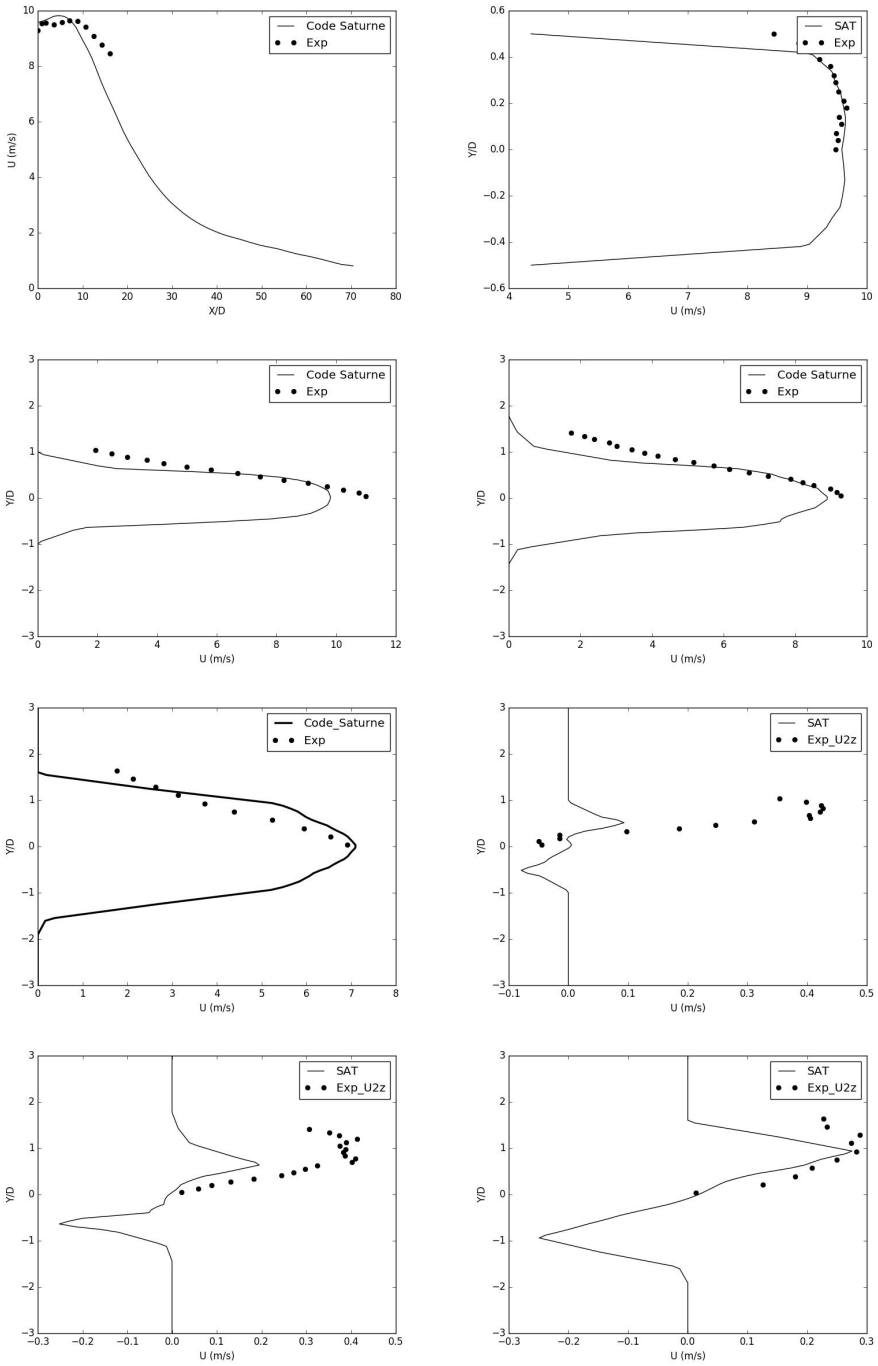

Figure 78 – Comparison between the results of the experiment and the simulation for the particulate velocity for the case of $d_p = 70\ \mu m$.

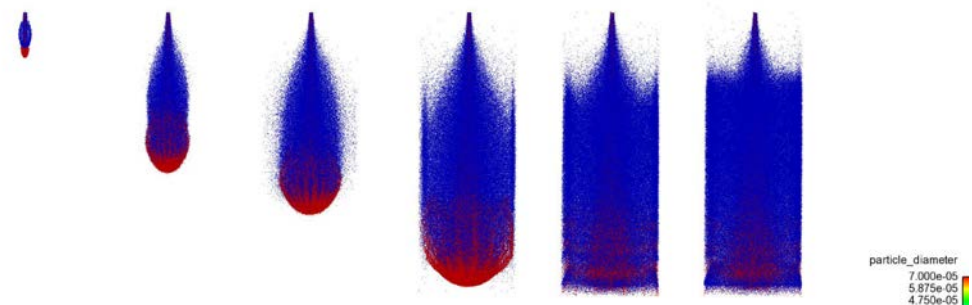

(a) 0s (b) 0.5s (c) 1s (d) 2s (e) 3s (f) 4s

Figure 79 – Results of the particle dispersion of the bidisperse case of $d_p = 25\ \mu m$ and $d_p = 70\ \mu m$.

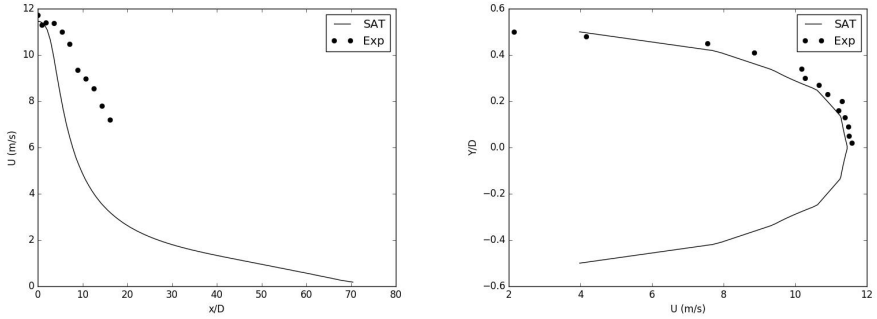

Figure 80 – Comparison between the results from the experiment and the simulation for the gas phase for the bidisperse case.

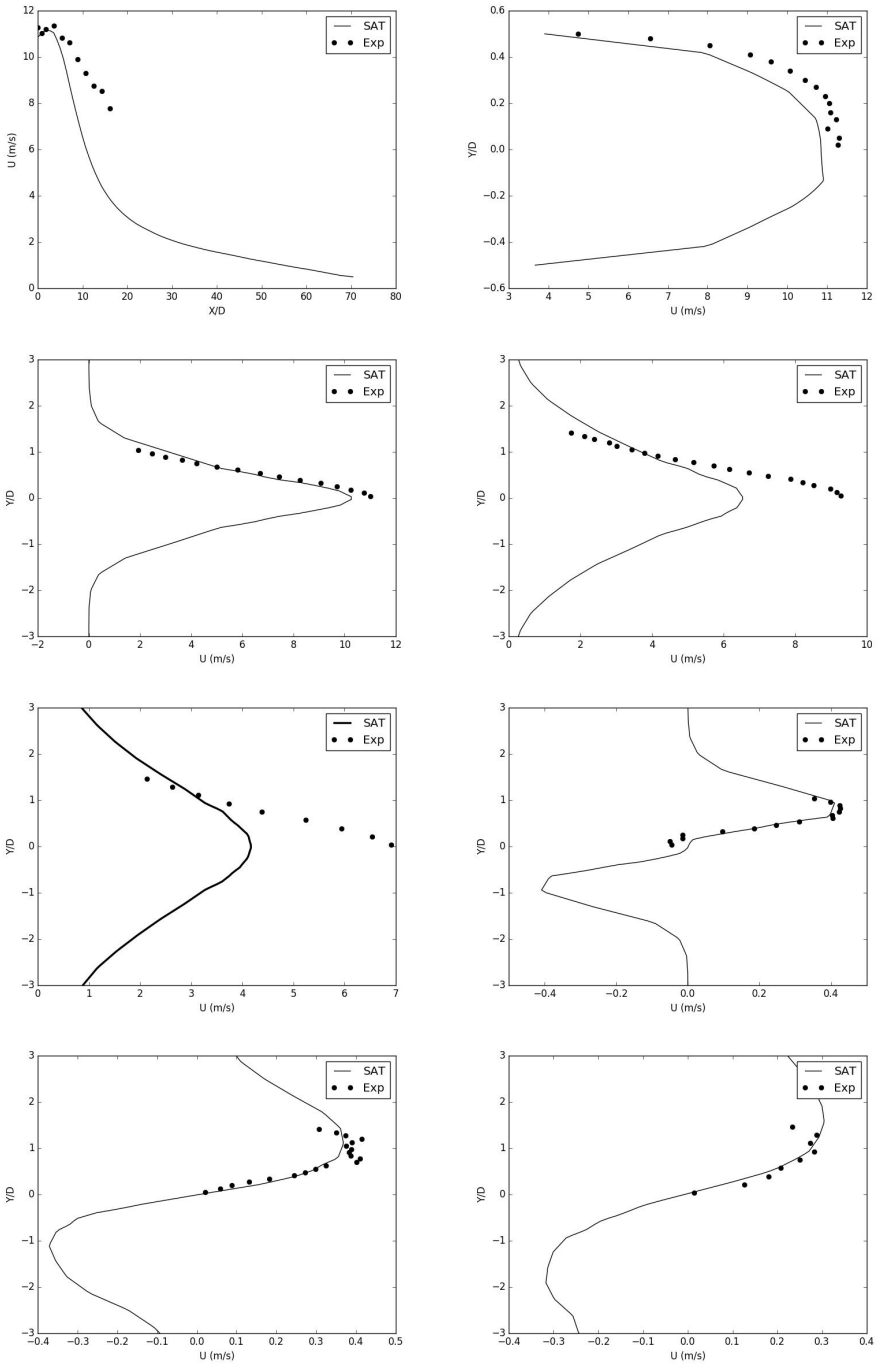

Figure 81 – Comparison between the results of the experiment and the simulation for the particulate velocity of $d_p = 25\ \mu m$ for the bidisperse case.

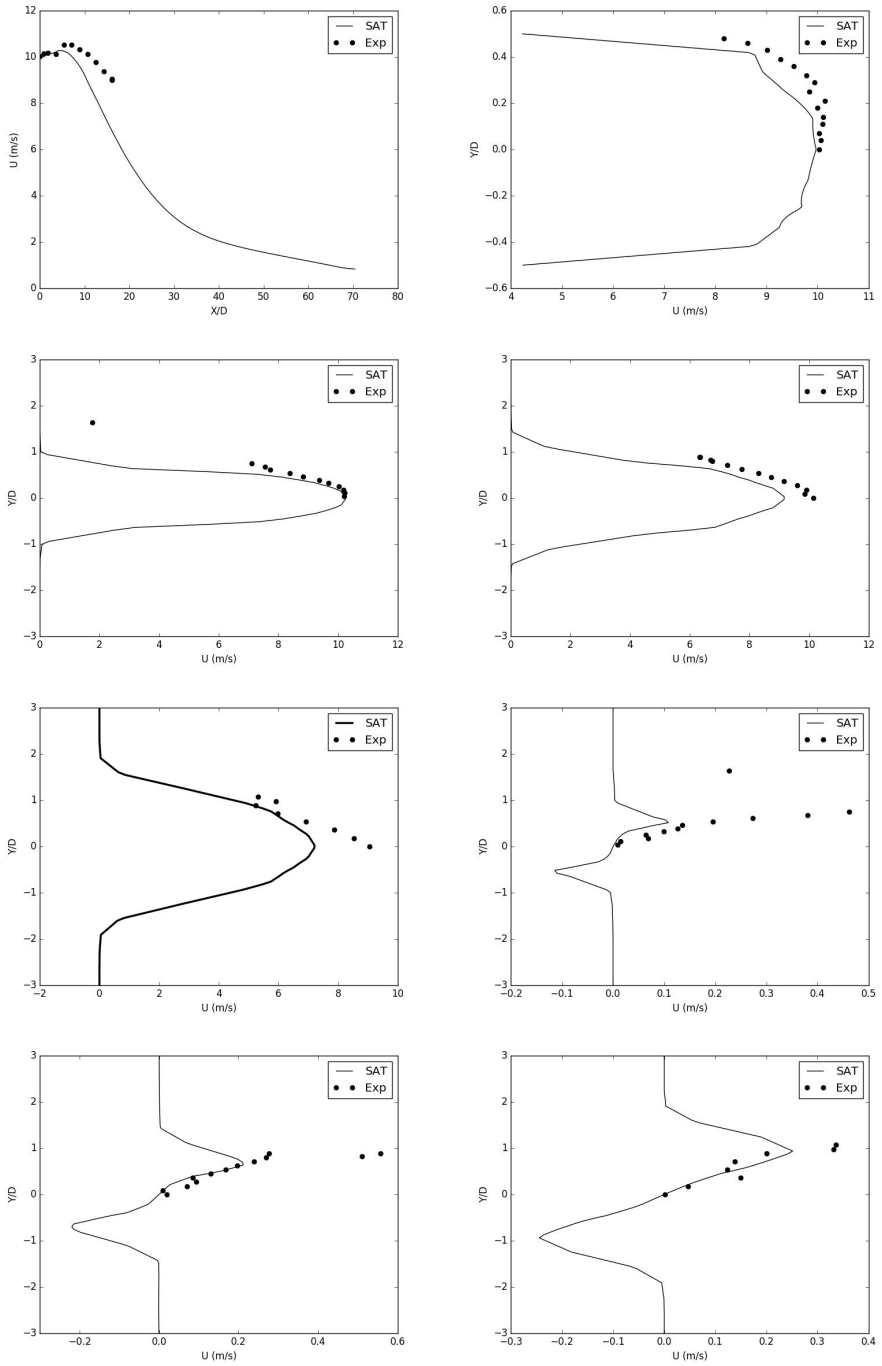

Figure 82 – Comparison between the results of the experiment and the simulation for the particulate velocity of $d_p = 70\ \mu m$ for the bidisperse case.

Appendix C

Experiment on particle jet

We can distinguish two types of experiments based on the particles size: experiments on microparticles dispersion and experiments on nanoparticles dispersion. The experiments on microparticles dispersion use the particles size above 1 μm. The experiments on nanoparticles dispersion use agglomerates composed by primary particles whose sizes are in nanoscale. However, the agglomerate size can be in nano or micro scale. The aim of those experiments is to measure the particles parameters as the particles velocity function distribution, the particles mass and size distribution function and eventually, for nanoparticles, the agglomerate fractal dimension and the agglomerate strength. The reader can refer to the work of Hamelmann et al. [43] and Alloul-Marmor [4] for the review of different experimental methods of the powder dispersion. Here, some experiments on microparticles dispersion are presented in Table 22. Some experiments on nanoparticles dispersion are presented in Table 23.

The main difficulty in the experiments on nanoparticle dispersion compared to the experiments on microparticles dispersion is the measurement apparatus capacity and cost. In addition, the nanoparticles experiment have to be performed in the confined environment because of the undetermined toxicity of those nanoparticles. At INERIS and in the context of the thesis, it is interesting to build an experiment on nanoparticles dispersion. The results of the experiment can help to have a better understand of the nanoparticles behavior in the air. In addition, the a comparison between the experiment data and the numerical simulation results can be performed. In the first step, the experiment of the microparticles dispersion is realized. After that, the experimental setup will be adapted for the nanoparticle dispersion case.

Experimental type	Author	Experimental object	Powder type	Measurement System	Parameters measured
Jet under pressure	SUTTER [110]	Characterization of powder in suspension	Microparticle TiO_2. (d_p = 5-19 μm)	PARE (Pressurized Airborne Release Equipment)	Particle size distribution, mean particle, mass in suspension
Free fall of powder and resuspen-sion	PLINKE et al. [72]	Characterization powder in free fall	Micro particle TiO_2 (d_p above 5 μm)	Six stage Sierra Model 236 impactor	Quantity and size distribution of particle, powder cohesion.
Free fall of powder	WYPYCH et al. [125]	Air entrainment, particle size distribution	Microparticle Alumina, Sable, Corvic vinyl.	Malvern Laser Diffraction Particle Size, High Speed camera	Air entrainment, air volume fraction and velocity, particle size distribution and velocity.
Free fall of powder	ANSART et al. [7]	Dust emission when free fall of powder.	Silice ($d_p = 34 - 97\mu m$)	Spraytec laser granulometer	Size, velocity distribution and concentration of particles, quantity of air entrainment.
Particle jet	Hadinoto et al. [42]	Particle dispersion and particle collision	Glass beads ($d_p = 25\mu m$ and $d_p = 70\mu m$)	LDA/PDA	Velocity distribution of gas and particulate phase.

Table 22 – Review of some experiments on microparticles dispersion in the literature.

Experimental type	Authors	Object	Powder used	Measurement system
Fluidized bed	Zhu et al., [132]	Effect of gas phase on the agglomeration of nanoparticles.	TiO_2 ($d_{pp} = 21nm$), SiO_2 ($d_{pp} = 7 - 40nm$)	Optical method : Laser Physics Reliant 1000m, CCD camera
Free fall of nanopowder	Ibaseta et al. [52]	Nanoparticle properties in free fall	TiO_2 ($d_{pp} = 5 - 12nm$), SiO_2($d_{pp} = 12nm$)	ELPI, Filters HEPA
Nanoparticles jet	Stahlecke et al, [109] , Ding et al., [27]	Breakage of agglomerates	TiO_2 ($d_{pp} = 27$ nm and $d_{pp} = 42$ nm), CeO_2 ($d_{pp} = 14$ nm and $d_{pp} = 70$ nm), $SrCO_3$ ($d_{pp} = 14$ nm)	SMPS, SEM
Agglomerate impaction	Ihailainen [54]	Breakage of agglomerates by impact with a surface	TiO_2 ($d_{pp} = 27$ nm and $d_{A,m} = 250, 300, 400$ nm)	DMA, MOUDI
Agglomerate impaction	Froeschke et al., [35]	Breakage of agglomerates by impact with surface	TiO_2 ($d_{pp} = 95$ nm), Ag ($d_{pp} = 8nm$), Ni ($d_{pp} = 4nm$)	TEM, SSLPI
Agglomerate breakage	Wengeler & Nirschl [122]	Breakage of agglomerates by high pressure dispersion	Nanoscale silica powder $d_A \approx 200 - 400nm$	Small Angle x-ray Scattering (SAxS), Dynamic light scattering.
Agglomerate breakage	Ammar et al., [6]	Breakage of agglomerates by high pressure dispersion	TiO_2 $d_A \approx 100 - 1000nm$	OPC, ELPI, SEM, LDA.

Table 23 – Review of experiments on nanoparticle dispersion in the literature. ELPI: Electrical Low Pressure Impactor, HEPA: High Efficiency Particulate Air, SMPS: Scanning Mobility Particle Sizer, SEM: Scanning electron microscopy, DMA: Differential Mobility Analyze, MOUDI: Micro-Orifice uniform deposit impactor. TEM: Transmission Electron Microscopy, SSLPI: Single -stage low pressure subsonic impactor, OPC: Optical particle Counter, LDA: Laser Doppler Anemometer

C.1 Experimental set-up

Figure 83 shows schematically the experimental set-up in the present study. The experiment is realized inside a tunnel in order to avoid the wind field influence. In the tunnel, a ventilation flow with very low velocity ($\approx 0.3\ m/s$) compared to jet velocity is set in order to evacuate the particles out the test tunnel. A box contained the powder is considered. In the low part of one box's face, an air flow is injected into the powder bed in order to create the particle air flow. To have a better particle - air mixture, a propeller in the center of the box is implemented. The propeller is a few centimeter above the powder bed surface. A nozzle is implemented in another box's face. A particle jet is created when the nozzle is opened. The diameter of the nozzle can be change from 10 mm up to 20 mm. For the experimental case considered, the nozzle have the interior diameter of 10 mm and the exterior diameter of 12 mm. The top face of the box can be opened to fill the powder. Under the box, a balance measures the weight of the box at different instance of the particle jet in order to estimate the mean particle mass flow rate. A measurement device PDA is used to measure the particle velocity and the particle diameter at different positions within the jet. The PDA is chosen because the measurement does not influence the particle jet. The choice is also based on the minimal particle size measured of 10 μm and its availability at INERIS. In addition, a high speed camera of type FASTCAM SA3 model 120K-M2 is used in order to observe the particles jet.

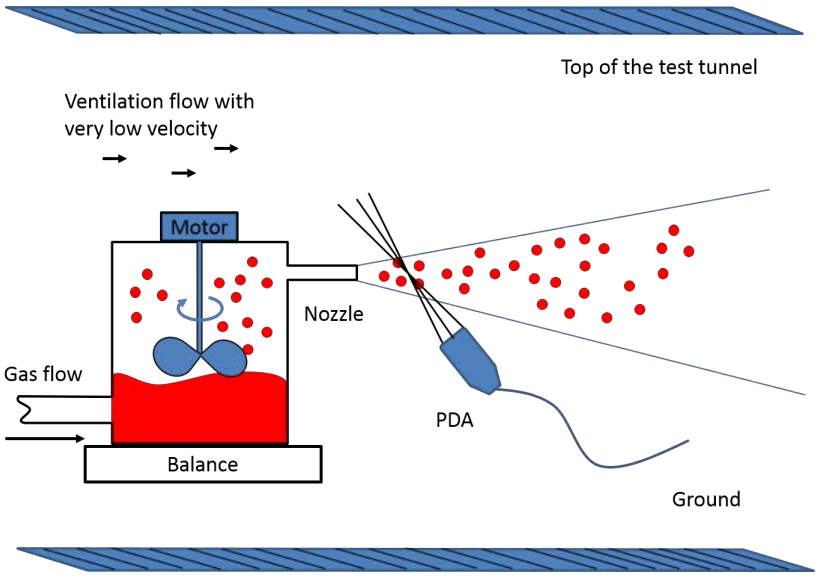

Figure 83 – Schematic presentation of the experimental configuration

Figure 84 shows the photo of the experiment.

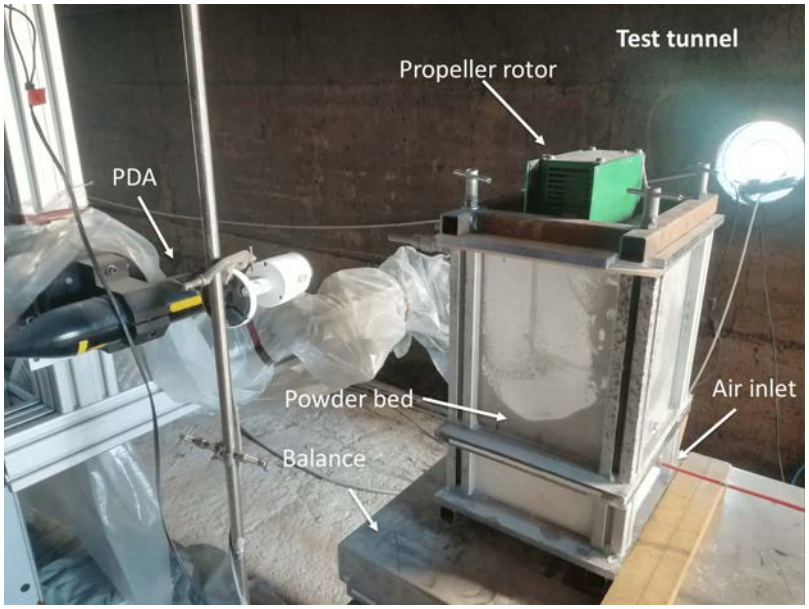

Figure 84 – Photo of the experiment

C.2 Experimental results

C.2.1 Visualization of the jet by high speed camera

The record rate of the high speed camera is 10000 fps with a shutter speed of 1/15000 s. Figure 85 shows the dispersion of particles jet at a steady regime. The core region of the jet can be observed near the nozzle. After this field, the particle dispersion is less stable.

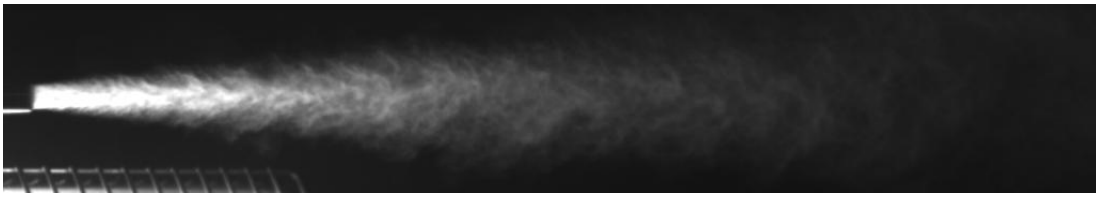

Figure 85 – Dispersion of particles jet captured by the high speed camera

C.2.2 Velocity and particle size by PDA measurement

The principal method of the Phase Doppler Anemometry can be founded in detail elsewhere [62].

Figure 86 shows the measurement profile realized with PDA.

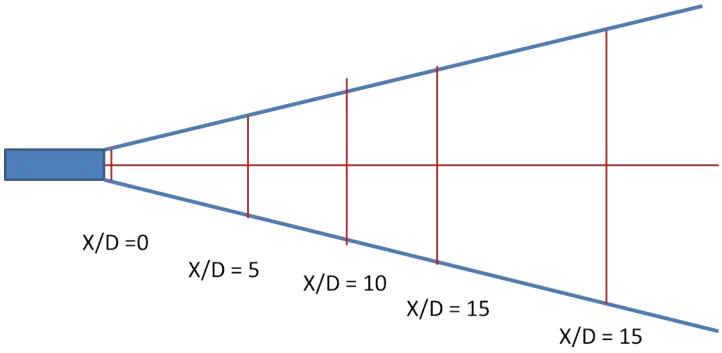

Figure 86 – Measurement profiles realized with PDA

The particles size distribution measured is the same between different positions measured. In this reference set-up, there are no breakage neither agglomeration well observed. Figure 87 shows the mean size distribution of particles measured.

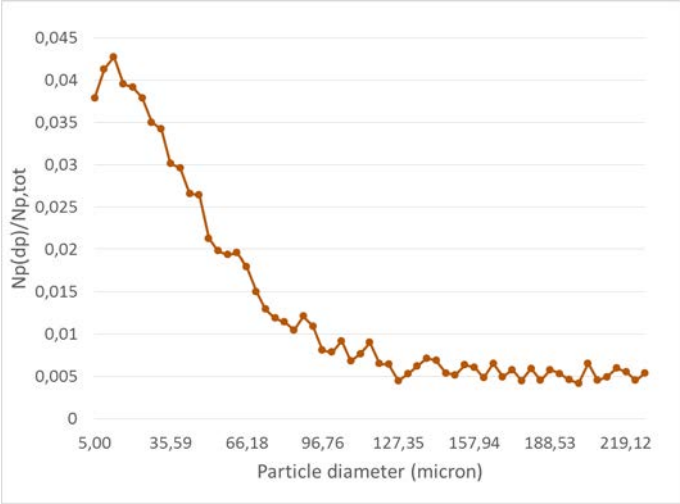

Figure 87 – Mean frequency of the particle distribution in the jet

Figure 88 shows the axial distribution of the particle velocity.

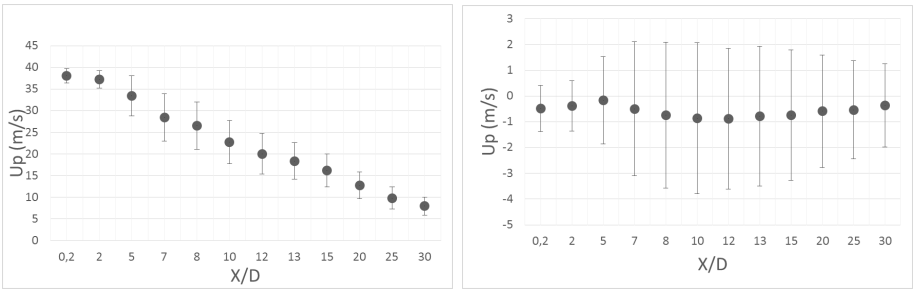

Figure 88 – Component velocity in the jet axis (left) and component velocity perpendicular to the jet axis(right).

Figure 89 shows the radial distribution of the velocity at different distances from the nozzle.

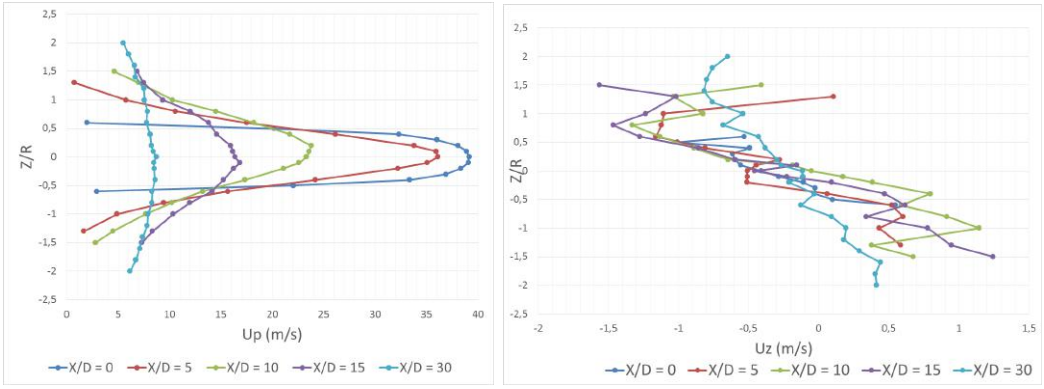

Figure 89 – Radial distribution of the particles velocity at different distances from the nozzle